

# Lithium-Ion Batteries and Materials

Cynthia A. Lundgren, Kang Xu, T. Richard Jow, Jan Allen, Sheng S. Zhang

Lithium-ion (Li-ion) batteries are now widely implemented as the power or energy source for everything from portable electronics to electric vehicles. The electrochemical charge storage in the batteries is intimately related to their material properties. This chapter gives an overview of the methods for characterizing battery materials, both ex situ and in situ in practical cells. An important consideration is the interphase between the active charge storage materials and the electrolyte, often called the secondary electrolyte interphase (SEI) layer. Different methodologies unlock different aspects of the battery materials and interphases. Standard test methods are summarized as well as emerging methodologies. Next generation Li-ion batteries, such as Li-sulfur and Li-air are also described.

<b>15.1 Overview – Electrochemical Evaluation of Li-Ion Batteries</b> .....	449
<b>15.2 Evaluation of Materials and Components in Li-Ion Batteries</b> .....	451
15.2.1 Electrode Evaluation .....	451
15.2.2 Electrolytes and Interphases .....	454
15.2.3 Separators .....	470
15.2.4 Advanced/In Situ Spectroscopy .....	471
<b>15.3 Evaluation at the Cell–Battery Level</b> .....	481
15.3.1 Cell Configurations .....	481
15.3.2 Performance Characteristics .....	481
15.3.3 Energy Density .....	483
15.3.4 Power Capability .....	483
15.3.5 Cycle Life and Storage Life (or Calendar Life) .....	485
15.3.6 Safety .....	486
<b>15.4 Beyond Li-Ion</b> .....	487
15.4.1 Li–S Battery .....	487
15.4.2 Li–Air Battery .....	489
<b>15.5 Conclusions</b> .....	490
<b>References</b> .....	491

Batteries are inherently electrochemical systems undergoing oxidation/reduction reactions. A primary battery is a galvanic cell that converts chemical energy into work. A rechargeable battery combines the galvanic cell with an electrolytic cell, where electrical work is converted into chemical energy upon charging. For a galvanic battery, a positive electrode (cathode) is paired with a negative electrode (anode), which allows a spontaneous oxidation reaction at its surface while sending electrons to the positive electrode through an external circuit, causing a reduction reaction there. Meanwhile

within the cell an electrolyte allows the motion of ions in response to an electric field to maintain local and global electroneutrality.

Some figures of merit (FOM) include:

- Storage capacity or charge density (Ah/kg or Ah/l)
- Specific energy (J/kg or Wh/kg)
- Energy density (J/l or Wh/l)
- Specific power (W/kg)
- Power density (W/l)
- Voltage efficiency; ratio of output voltage to  $E^0$ .

## 15.1 Overview – Electrochemical Evaluation of Li-Ion Batteries

Many of these FOM are controlled by the same characteristics that control all electrochemical reactions, including mass loading, surface area, voltage difference between anode and cathode, mobility of ions, resistance of the electrolyte, kinetics and reversibility of the reac-

tions. All modern advances in battery chemistries and components have resorted to various electrochemical methods to evaluate performance and stability. For instance the intrinsic voltage of many battery systems at equilibrium is controlled by the Nernst equation, which

is derived from the Gibb's free energy relationship

$$\Delta G = -nFE. \quad (15.1)$$

For any reaction

$$aA + bB = cC + dD. \quad (15.2)$$

The voltage of the system can be expressed by

$$E = E^0 - \frac{RT}{nF} \ln \frac{[C]^c [D]^d}{[A]^a [B]^b}, \quad (15.3)$$

where  $E^0$  is the standard electrode potential,  $R$  is the gas constant,  $T$  is the temperature in K,  $F$  is the Faraday constant,  $n$  the number of electrons involved in the oxidation/reduction reaction, and  $[A]$ – $[D]$  are the concentrations of each species.

The actual voltage produced will always be lower than the theoretical voltage due to voltage loss from parasitic processes and chemistries, and the profile upon discharge is a function of the chemistry, temperature, internal impedance, state of charge (SOC), age of the cell and the kinetics (rate of discharge, often expressed in C-rates). All of these parameters can be studied electrochemically. Some batteries such as lead acid can have the state of charge estimated by voltage at equilibrium; however, some Li-ion cells have a relatively flat voltage profile, indicative of a two-phase system [15.1] (Sect. 15.2.1) during the topotactic intercalation of  $\text{Li}^+$ . This makes the estimate of state of charge more complicated than just measuring the voltage of the cell at equilibrium. Coulomb counting is a common method to determine the state of charge of these batteries.

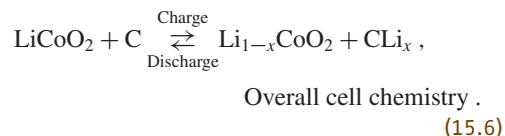
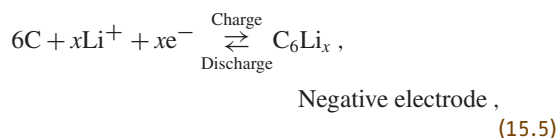
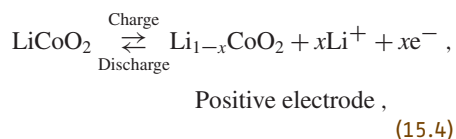
Battery components undergo the same electrochemical characterization as other redox systems to determine kinetics, reaction reversibilities, current–voltage behavior, reaction mechanisms and stabilities. These methods include cyclic voltammetry, impedance spectroscopy, coulometry, and so on, and will be discussed in more detail in the subsequent sections. Many of these electrochemical techniques have been augmented by in situ analytical methods, such as in situ extended x-ray absorption fine structure (EXAFS), atomic force microscopy (AFM), IR and nuclear magnetic resonance (NMR) so that chemical and/or structural changes can be observed as a function of real use conditions under an electric field (Sect. 15.2.4).

The development of Li-ion batteries has been spurred by the proliferation of portable electronic devices and the need for higher driving range electric vehicles needing higher energy density batteries that are safe and long lasting. Rechargeable Li-ion batteries have dominated the portable electronics market since their introduction. Due to their relatively high energy

density and capacity and good cycle life and storage characteristics, they rapidly replaced Ni–Cd and Ni–metal hydrides, which had been the most widely used in portable electronics prior to Li ion.

The history and advances in Li-ion technology start with the idea of Li metal being used as the source of energy in a battery because of its low weight, high electrochemical potential and stability in nonaqueous electrolytes. Li primary batteries were commercialized in the late 1960s and early 1970s using Li/SO<sub>2</sub>, which is still commercially available today. Significant efforts in developing rechargeable Li metal batteries ensued with initial promise shown by Exxon's Li/TiS<sub>2</sub> system [15.2] and then by Ballard Research Inc. and Moli Energy Ltd. However, the problems of Li dendrite formation upon cycling resulted in fires and a NTT recall of Moli batteries in 1989. To date, research is still being actively pursued to develop a rechargeable Li metal or metal–air battery to meet the growing needs of the industry (Sect. 15.4).

The inherent safety issues of using Li metal as the anode led to the development of graphite intercalation materials in the late 1970s by *Basu* and coworkers, *Yazami* and coworkers and patented by Bell Labs [15.3–5]. At the same time, *Goodenough* and *Muzichima* published a report using LiCoO<sub>2</sub> as a stable intercalation cathode that can reversibly accommodate Li ions [15.6]. These inventions laid the basis for the modern Li-ion battery, leading to its commercialization by Sony in 1991 [15.7]. The electrochemistry of this new battery is shown in the below equations



Research into optimizing and developing new chemistries and electrolytes has since grown dramatically. Increasing needs for more energy, higher power, and longer cycle life have led to the development of new materials. The increased interest in hybrid electric vehicles (HEVs) and electric vehicles (EVs) has led to an increased emphasis on safety, especially for

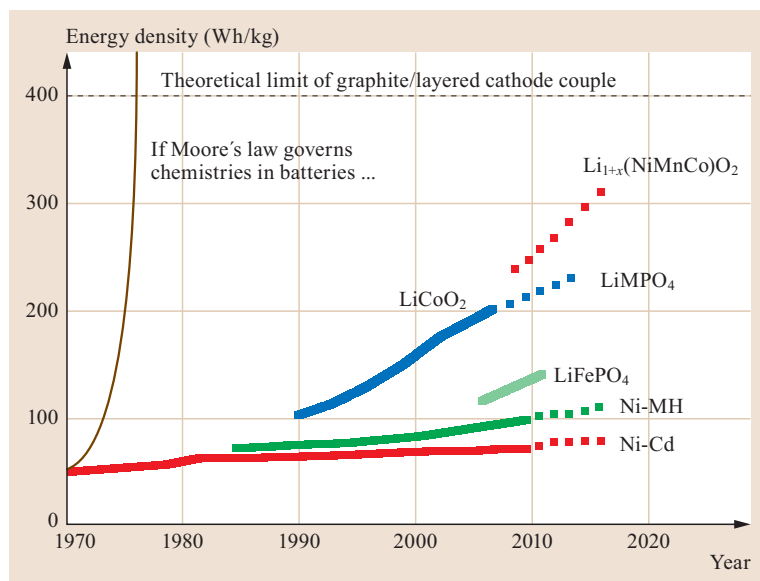


**Fig. 15.1** Advancement in advanced battery energy density as a function of time

larger format cells. Figure 15.1 shows the advancement of these Li-ion battery metrics with time. Progress has been steady but incremental, especially compared to the progress in advances of electronics during the same era, which has followed Moore's law (Fig. 15.1).

The rest of this chapter will elaborate the details on the recent advances made in Li-ion batteries and their components and the electrochemical methods that have made them possible, with a foray at the end into what is next, beyond Li ion (Sect. 15.4).

## 15.2 Evaluation of Materials and Components in Li-Ion Batteries

### 15.2.1 Electrode Evaluation

Electrode materials can be evaluated by a number of physical methods to predict their performance in a Li-ion cell. Diffraction is a bulk method which gives the average structure over a large number of unit cells.

This has been an important technique for the development of new electrode materials as the typical Li-ion insertion reaction is either a solid solution formation (same phase) or a topotactic transition (meaning there is little change in structure between the charged and discharged state). However, in some cases new phases can be formed. These Li-insertion mechanisms have been more troublesome owing to large changes in the volume between the charged and discharged states. Bulk transitions can be studied by electrochemical methods as well. Beyond this bulk method, local environments have been probed through spectroscopic and electrochemical methods. Thermal methods have shed light on safety considerations. Finally, the potential electrode materials need to be screened in a full electrode pair in order to understand the interactions between the two electrodes and also to determine the behavior when a large

surplus of Li reservoir is no longer available, as is the case for a *half* cell. Specific illustrative examples follow.

#### Diffraction

Diffraction experiments are useful to understand the structural transformations of the electrodes at the bulk level. Diffraction can give information on the crystal structure of the electrodes and changes in lattice constants. The formation of new phases and changes in atomic order can be quantified with high accuracy. For example, *Courtney and Dahn* [15.9] used in situ x-ray diffraction to understand the conversion reactions of various Sn oxides including SnO, SnO<sub>3</sub>, LiSnO<sub>3</sub> and SnSiO<sub>3</sub>. The diffraction experiments shed light on the mechanism of the conversion. Initially, Li<sub>2</sub>O and Sn are formed followed by an alloy formation. *Andersson and Thomas* [15.10] used neutron powder diffraction to study the two-phase reaction characteristic of LiFePO<sub>4</sub> to FePO<sub>4</sub>. By using Rietveld refinement the ratio of triphylite (LiFePO<sub>4</sub>) to heterosite (FePO<sub>4</sub>) could be quantified and information was gained on the mechanisms for Li insertion and extraction. *Dela-*

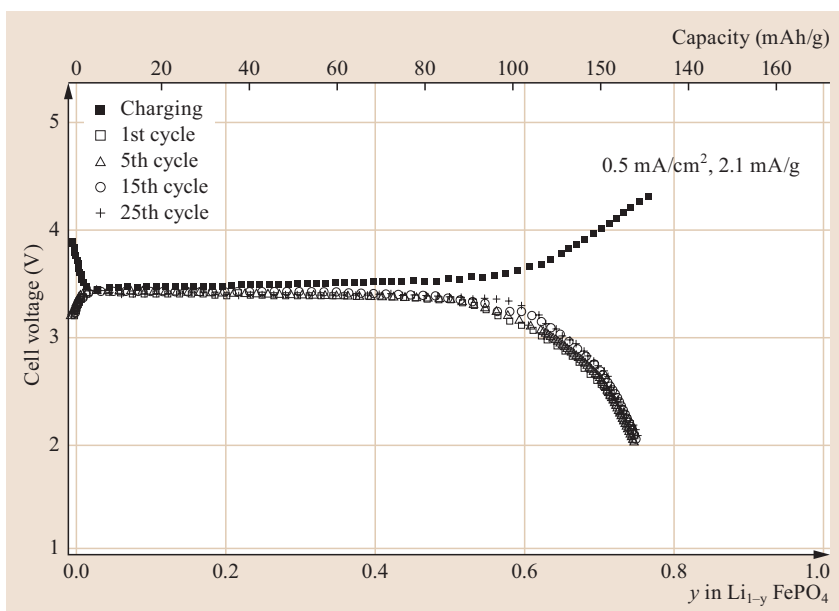


**Fig. 15.2** Constant current (2.0 mA/g) discharge and charge curves of  $\text{LiFePO}_4$  (after [15.8], courtesy of Electrochem. Soc., 1997)

court et al. [15.11] used diffraction to show that the two-phase mechanism changes at temperature above  $450^\circ\text{C}$  to a mechanism where a  $\text{Li}_x\text{FePO}_4$  ( $0 \leq x \leq 1$ ) solid solution is observed. Aurbach et al. [15.12] used diffraction to understand the capacity fading of  $\text{LiMn}_2\text{O}_4$  spinel. The authors observed formation of more disordered phases upon cycling in addition to Mn dissolution, which occurred at voltage  $> 4.4$  V. Understanding of the staging phenomenon in graphite has been heightened by diffraction studies of the intercalation of Li into graphite. Dahn [15.13] used in situ x-ray diffraction to determine the phase diagram of  $\text{Li}_x\text{C}_6$ . Another study by Ohzuku et al. [15.14] used x-ray diffraction to observe various stages of Li intercalation into graphite such as  $\text{LiC}_6$  (stage 1),  $\text{LiC}_{12}$  (stage 2) and so on up to  $\text{LiC}_{72}$  (stage 8). Additionally, differences in Li ordering could be discerned.

### Spectroscopic

Spectroscopic studies of electrodes are particularly useful for understanding changes in the valence of the active transition metal that occurs during the redox process of a functioning Li-ion battery and to observe the local environment. For example, Shaju et al. [15.15] studied the  $\text{LiNi}_{0.5}\text{Mn}_{0.5}\text{O}_2$  cathode using x-ray photoelectron spectroscopy (XPS) and observed a  $\text{Ni}^{2+}/^{4+}$  redox couple and a  $\text{Mn}^{3+}/^{4+}$  couple. Johannes et al. [15.17] used XPS to understand the electronic structures of  $\text{LiMPO}_4$  olivines by combining the spectroscopy with ab initio computations. Li-6 and Li-7 NMR has been used to study the local environment of Li with cathode materials. For example, Lee et al. [15.18]

studied  $\text{LiMn}_2\text{O}_4$ ,  $\text{Li}_2\text{Mn}_4\text{O}_9$  and  $\text{Li}_4\text{Mn}_5\text{O}_{12}$  through NMR and the resonances could be assigned to different local environments. Key et al. [15.19] used in situ Li NMR to study the changes in local structure

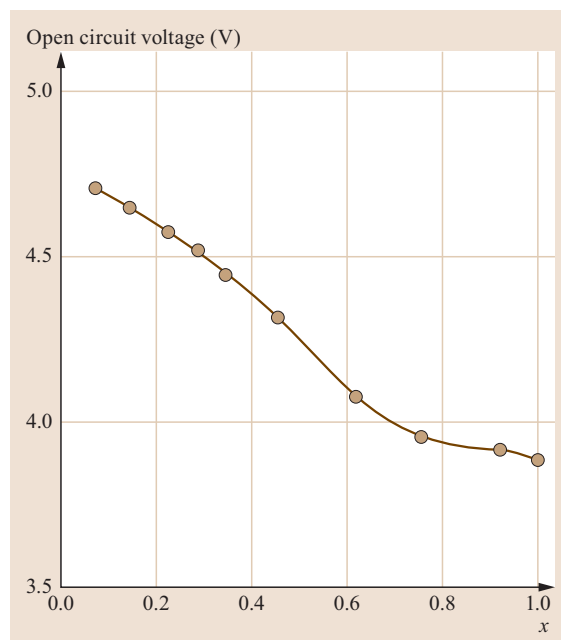


**Fig. 15.3** Open-circuit voltage curve for  $\text{Li}_x\text{Co}_{1.01}\text{O}_2$  as a function of  $x$ . A single-phase region is observed down to about  $x = 0.7$ , after which a two-phase region is observed (plateau-like behavior) (after [15.16], courtesy of Pergamon Press Ltd, 1980)

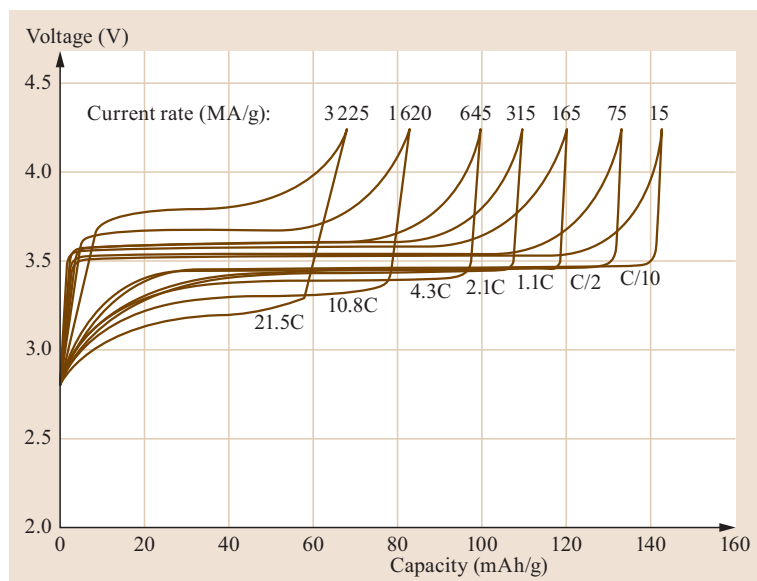


**Fig. 15.4** Discharge capacity curves of carbon coated  $\text{LiFePO}_4$  as a function of discharge capacity (after [15.20], courtesy of Electrochem Soc., 2001)

that occur during the Li intercalation of Si. The authors directly observed formation of isolated Si atoms and a spontaneous side reaction of lithium silicide with the electrolyte via in situ NMR experiments. Mössbauer spectroscopy is another technique which has been used to further the understanding of Li-ion electrode materials. This technique is particularly applicable to materials where the  $^{57}\text{Fe}$  nuclei can be studied. For example, *Andersson et al.* [15.21] used the Mössbauer effect to measure the  $\text{Fe}^{3+}/\text{Fe}^{2+}$  ratio during the Li extraction–insertion in  $\text{LiFePO}_4$ . *Allen et al.* [15.22] used Mössbauer to measure the ratio of  $\text{Fe}^{3+}/\text{Fe}^{2+}$  in Fe-substituted  $\text{LiCoPO}_4$  and to study the local coordination environment. *Dunlap et al.* [15.23] used the  $^{119}\text{Sn}$  Mössbauer effect to study the local environment of Sn during Li intercalation.

### Electrochemical

Electrochemical techniques have been used to probe the electrode behavior and in particular the diffusion of Li into and out of the electrode material. It can be also used to probe the kinetics of phase transitions. Electrochemical techniques directly measure the battery performance, primarily the amount of energy stored and the rate at which the energy can be utilized. The most simple but informative technique is to build an electrochemical cell, apply a constant current to the cell and monitor the cell voltage as a function of time to a certain cutoff voltage that varies by cathode material. Based on the time of discharge (or charge) the cathode capacity is calculated, which can be expressed in mAh/g or in Wh/kg, which is more useful when comparing materials with different voltage profiles. The rate of the battery

or power can be compared by measuring the discharge at different constant currents.

Figure 15.2 shows an example of a galvanostatic discharge and charge curve for  $\text{LiFePO}_4$  showing the cell voltage as a function of capacity [15.8]. The curve shows a voltage plateau over a large range of Li content, which the authors explain is indicative of a two-phase interface. This method is used to evaluate the capacity (amount of Li that can be removed and reinserted). In this original paper on the use of  $\text{LiFePO}_4$  as the cathode, a capacity of about 100 mAh/g was shown for the 3.4 V plateau, which corresponds to an energy content of 340 Wh/kg ( $3.4 \text{ V} \times 100 \text{ mAh}$ ).

A sloping voltage curve indicating a solid-solution-type behavior for the Li intercalation is shown for  $\text{Li}_x\text{CoO}_2$  in Fig. 15.3 [15.16]. A single phase region is observed from  $1 < x < 0.7$ . The capacity obtained for full delithiation is about 274 mAh/g, however in practice the discharge is limited to about  $x = 0.5$  ( $\approx 137 \text{ mAh/g}$ ) in a rechargeable cell because of poor reversibility at high delithiation. The capacity and voltage will vary as a function of rate. As the current increases, the usable capacity of the cell decreases. An illustrative example is shown in Fig. 15.4 [15.20]. In this case the rate capability is determined by measuring the capacity of a  $\text{LiFePO}_4$  cathode by varying the current during a constant current discharge.

Cyclic voltammetry (CV) is a useful technique in which the voltage is linearly scanned in both directions while measuring the current response. A very small amount of material can be used and it can give insights into many of the physical processes occurring within the cell. For example, *Levi et al.* [15.24]

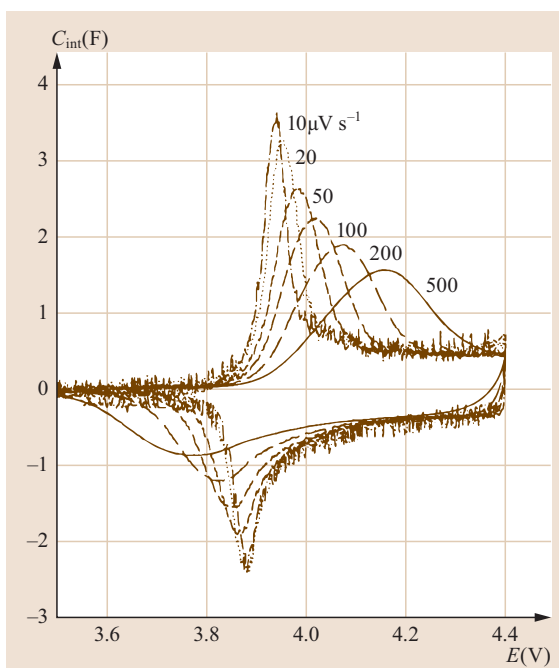


**Fig. 15.5** Multiple variable-rate, slow-scan cyclic voltammograms of  $\text{LiCoO}_2$  showing the differential intercalation capacity  $C_{\text{int}}$  as a function of the electrode potential. The positive peak and negative peaks indicate intercalation and deintercalation of Li into and out of  $\text{LiCoO}_2$ , respectively (after [15.24], courtesy of Electrochem. Soc., 1999)

combined the use of CV, (Fig. 15.5) potentiostatic intermittent titration (PITT) techniques and electrochemical impedance spectroscopy (EIS) to understand the behavior of  $\text{Li}_{1-x}\text{CoO}_2$  electrodes. This study gave information concerning the solid-state diffusion of Li within the electrode material. The CV technique using a thin sample enabled the use of a Frumkin isotherm to characterize the intercalation process. The PITT technique estimated the chemical diffusion coefficient from application of a potential and measurement of the resultant current. EIS applies a small (AC) potential to the cell and measures the current through the cell. Owing to the small amplitude of the AC potential, the system is close to equilibrium. Levi used an equivalent circuit to obtain information about the Li-ion diffusion coefficient. A further example is that of *Takahashi et al.* [15.25] using cyclic voltammetry (CV) and EIS (Fig. 15.6) to evaluate the activation energy for Li diffusion of  $\text{LiFePO}_4$ .

Phase transformation has been studied using electrochemical methods. For example, the electrochemical  $\text{FePO}_4$  to  $\text{LiFePO}_4$  phase transition was studied by *Allen et al.* [15.26]. By measuring the conversion of  $\text{FePO}_4$  to  $\text{LiFePO}_4$  by galvanostatic discharge at differ-

ent temperatures, Avrami plots were obtained enabling an understanding of the dimensionality and the quantification of the activation energy of the phase transition (Fig. 15.7).

### Thermal

Thermal studies of electrode materials are particularly useful in order to understand the thermal stability of the electrode and consequently the safety under abusive conditions. An illustrative example of the utility of thermal studies is the work of *Dahn et al.* [15.27]. The authors studied the stability of  $\text{Li}_x\text{CoO}_2$ ,  $\text{Li}_x\text{NiO}_2$  and  $\text{Li}_x\text{Mn}_2\text{O}_4$  in order to understand the safety of Li-ion cells that utilize these cathodes. The fully lithiated cathodes,  $\text{LiCoO}_2$ ,  $\text{LiNiO}_2$  and  $\text{LiMn}_2\text{O}_4$  were shown to be fully stable in air up to high temperatures. However, partially delithiated samples,  $\text{Li}_x\text{CoO}_2$ ,  $\text{Li}_x\text{NiO}_2$  and  $\text{Li}_x\text{Mn}_2\text{O}_4$  ( $x < 1$ ) were shown to be only metastable. At moderate temperatures,  $\text{O}_2$  was shown to be liberated. Furthermore,  $\text{Li}_x\text{Mn}_2\text{O}_4$  was suggested to be superior in thermal stability relative to  $\text{Li}_x\text{CoO}_2$  or  $\text{Li}_x\text{NiO}_2$ . *MacNeil et al.* [15.28] reported on the reaction of electrode materials with electrolyte materials. Differential scanning calorimetry (DSC) was used to show the differences in reactivity with electrolyte between a number of Li-ion cathode materials including  $\text{LiCoO}_2$ ,  $\text{LiMn}_2\text{O}_4$  and  $\text{LiFePO}_4$ .

### Electrode Pairs

A successful Li-ion cell depends on the interaction of the spatially separated positive electrode (cathode) with the negative electrode (anode). In the Li-ion cell, the first charge involves the net transfer of Li from the cathode to the anode to form a passivation layer, which is a combination of the electrode surface and electrolyte components as is discussed elsewhere in this chapter. Electrochemical methods have been used to study the cathode–anode mass ratio, which is important for long cycle life. For example, *Moshtev et al.* [15.29] studied the effect on performance of the ratio of  $\text{LiNiO}_2$  to petroleum coke in Li-ion cells. *Tarascon and Guyomard* [15.30] reported on the  $\text{Li}_{1+x}\text{Mn}_2\text{O}_4/\text{C}$  system.

## 15.2.2 Electrolytes and Interphases

The electrolyte is an essential component in any electrochemical device. It acts as the ionic conductor and electronic barrier between the two reactants of the cell chemistry: oxidant (cathode) and reductant (anode). During the cell reaction, the electrolyte should maintain its mechanical, chemical and electrochemical inertness toward both electrodes. In rechargeable batteries, how the electrolyte interacts with electrodes often dictates



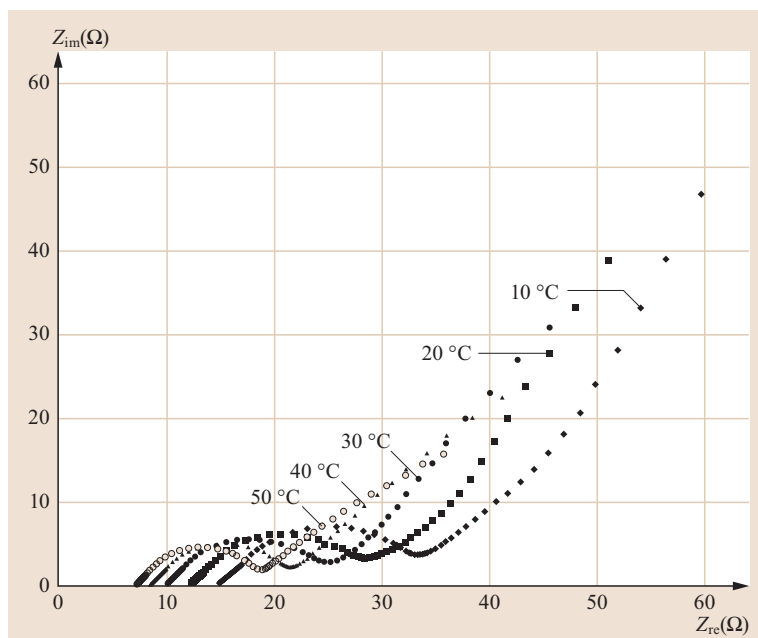


**Fig. 15.6** Electrochemical impedance spectrum of  $\text{LiFePO}_4$ , shown as a function of temperature. From this data a plot of the activation energy for Li-ion diffusion was derived (after [15.25], courtesy of Elsevier, 2002)

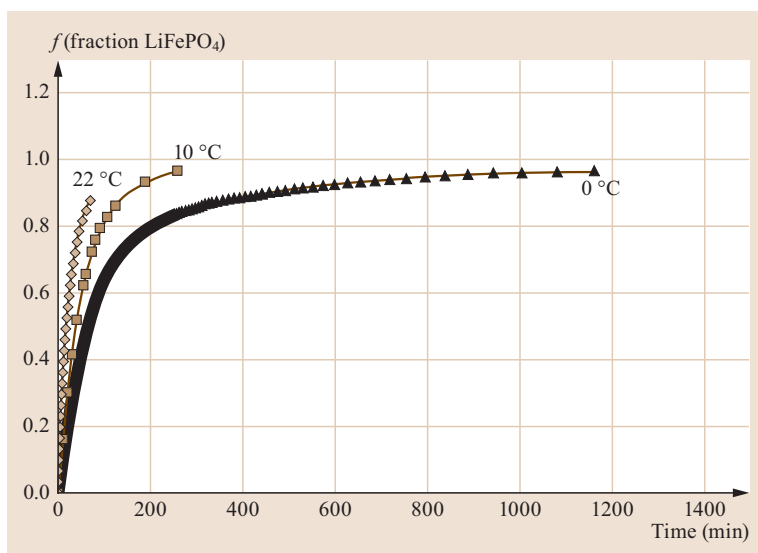


**Fig. 15.7** Fraction of  $\text{LiFePO}_4$  electrochemically formed from  $\text{FePO}_4$  as a function of time and temperature measured by recording the current as a function of time at a fixed voltage of 3 V. The assumption was that the current measured corresponded to the reaction  $\text{FePO}_4 + \text{e}^- + \text{Li}^+ \rightarrow \text{LiFePO}_4$ . From this data Avrami plots were obtained in order to gain insight into the mechanism of phase transformation (after [15.26])

the cycle life and power density of the device, and an electrochemical stability window is the most important requirement for successful electrolytes besides their capability of conducting ions [15.31].

In devices of low operating voltages ( $< 2.0$  V), such as aqueous-based batteries supercapacitors and fuel cells, etc., the electrochemical inertness of electrolytes is usually realized via the thermodynamic stability of each individual electrolyte component (solvent, salt, additive) against the electrodes. However, when operating voltages of 3.0 V or higher are pur-

sued for the sake of higher energy densities, almost no electrolyte components can remain thermodynamically stable against the strong reducing power of the anode or oxidizing power of the cathode; rather, the stability is achieved through a process called *passivation*, i.e., part of the electrolyte components sacrifice themselves by decomposing, and their products combine to form a protection layer to stop the same decomposition from occurring sustainably. The new interfacial phase is named *interphase* [15.32]. Li-ion batteries rely on such interphases to operate, because

the potential of their graphitic anode sits near 0.20 V for Li (or -3.0 V for SHE), which is far beyond the reduction potential of most known nonaqueous electrolyte components. The interphase on the graphitic anode is also known as the SEI (solid electrolyte interphase) after its  $\text{Li}^+$ -conducting/electronic insulating nature, and has become a topic of focused research in the past two decades. The existence of the cathode equivalent of the SEI is debated. The potential of the cathode in Li-ion batteries varies between 3.5 V of  $\text{LiFePO}_4$  to 4.2 V of diversified transition metal oxides  $\text{LiM}_x\text{O}_y$  ( $\text{M} = \text{Co}, \text{Ni}, \text{Mn}$  etc.), which correspond to 0.5–1.1 V for SHE, which is on the border of oxidation stability limits for most electrolyte components. What is beyond controversy is that, when the cathode potential is pushed higher than 4.5 V with the new 5 V class chemistries (e.g.,  $\text{LiNi}_{0.5}\text{Mn}_{1.5}\text{O}_4$ ,  $\text{LiCoPO}_4$  etc.), the appearance of interphases will become a certainty [15.33, 34].

This section will review the established method of characterizing electrolytes and the resultant interphases, which, unless specified, refer to the SEI on the graphitic anode surface.

### Bulk and Transport Properties

The state-of-the-art Li-ion batteries use electrolytes typically consisting of Li salts with fluorinated inorganic anions ( $\text{LiPF}_6$ ,  $\text{LiBF}_4$ ) dissolved in organic aprotic solvents consisting of carbonic dialkyl-esters or carboxylic esters. With few exceptions ethylene carbonate (EC) is almost an indispensable component due to its role in SEI formation [15.31]. There are also often ingredients at rather small concentrations (from ppm to a few percent), which are called *additives* [15.35]. The role of additives varies from preserving cell safety as *redox shuttles* or *flame retardants*, to assisting interfacial formation chemistry, and remain as unique trade secrets with each manufacture. However, the skeleton composition of most commercial electrolytes is based on solutions of  $\text{LiPF}_6$  in mixtures of EC with one or more of acyclic carbonic dialkyl esters, such as dimethyl carbonate (DMC) and ethylmethyl carbonate (EMC). The formulation of these state-of-the-art electrolytes is the result of a compromised consideration of the following list of requirements:

1. High ionic and low electronic conductivity
2. Wide liquid range (low liquidus temperature and low vapor pressure)
3. Ability to wet the polyolefin separator whose porous structure is usually lipophilic
4. Inertness to other cell parts such as substrates, binders, current collectors and tabs
5. High safety
6. Low toxicity (therefore of little disposal concern)
7. Low cost.

**Phase Diagram.** The service temperature range of electrolytes is actually determined by two different sets of standards: the *wider* range by their thermodynamic properties, beyond which the electrolytes would no longer be in the liquid state, and the *narrower* range by the corresponding electrochemical properties, only within which could the desired performances be delivered. The *wider* range is best represented in the form of phase diagrams and serves as the *minimum standard* a nonaqueous electrolyte must meet.

The classical phase diagrams for carbonate-based electrolyte solvent systems were mapped out by Ding and coworkers using conventional thermal analysis techniques such as DSC, where all possible combinations of the commonly used carbonates were found to be simple eutectic types [15.36, 37]. The typical binary phase diagram between EC and DMC and how it was constructed by DSC traces is schematically shown in Fig. 15.8a, where the solidus line defines the lower temperature limits for these systems. When mixtures of more than two solvents are used to formulate the electrolytes, the corresponding phase diagrams become increasingly complicated. Figure 15.8b shows one such diagram for the ternary system EC/DMC/EMC, in which the ternary liquidus and solidus faces were calculated based on the individual binary phase diagrams [15.38].

While a common feature of binary eutectic systems is the depression of liquidus temperatures for the mixtures, an important discovery by Ding et al. is that the effectiveness of such depressions are determined by two factors:

1. Molecular structure similarity
2. Melting point proximity of the two solvents.

For example, the mismatch between the high melting, cyclic EC (mp 37 °C) and low melting, acyclic EMC (mp -53 °C) results in a liquidus line that approaches the mp of EC for most of the compositions, so that the liquid range actually shrinks as compared with the EC/DMC binary system. A similar mismatch exists for almost all electrolyte compositions as long as EC is used, and it has led to a consistent issue of narrow service temperature ranges for all Li-ion batteries [15.36, 37].

**Solvation.** In order for Li salts to be dissolved into electrolyte solutions,  $\text{Li}^+$  must be stabilized by solvent molecules through coulombic coordination, which compensates the free energy increase as result of the



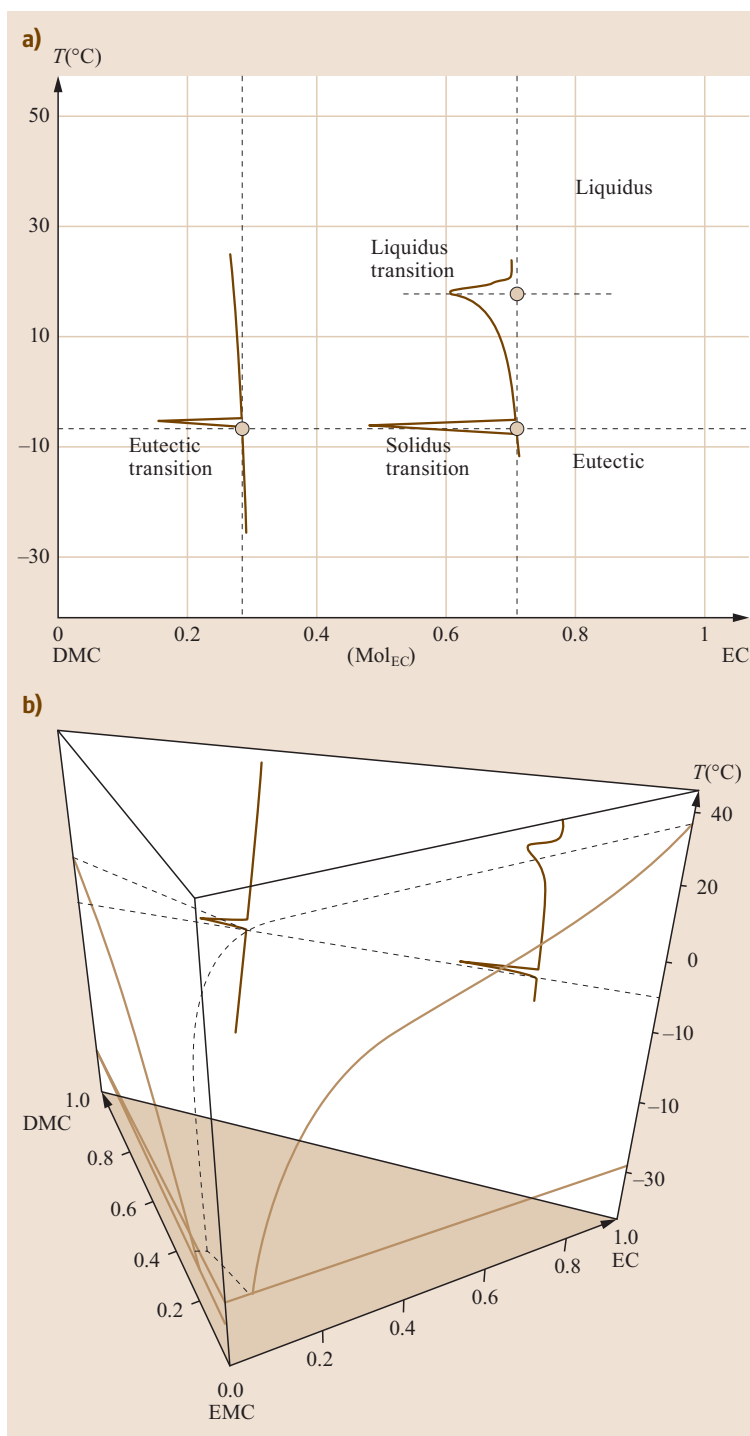


**Fig. 15.8** (a) Binary phase diagram of EC/DMC constructed by differential scanning calorimetry (DSC) experiments (marked by red traces), whose two peaks mark the temperature ranges where liquid and solid phases coexist. Above liquidus line the electrolyte is in true (or thermodynamically stable) liquid state, while in reality the liquid range could be significantly wider due to supercooling (metastable liquid state) (b) Ternary phase diagram of EC/DMC/EMC as calculated from thermodynamic non-ideal models based on experimental feedings from corresponding binary phase diagrams. The DSC traces shown in Fig. 15.8 were also shown on the EC/DMC plane. Again, above liquidus surfaces the electrolytes are *true liquids* (after [15.38])

lattice disruption. That is why nonaqueous electrolyte solvents are almost exclusively nucleophilic molecules that have nonpaired electrons. Each  $\text{Li}^+$  wrapped in such nucleophilic environments actually forms a solva-

tion sheath. The innermost layer of the sheath is called the *primary solvation sheath*, whose composition is relatively static during ionic movement; while solvent molecules more remote from the central  $\text{Li}^+$  consti-

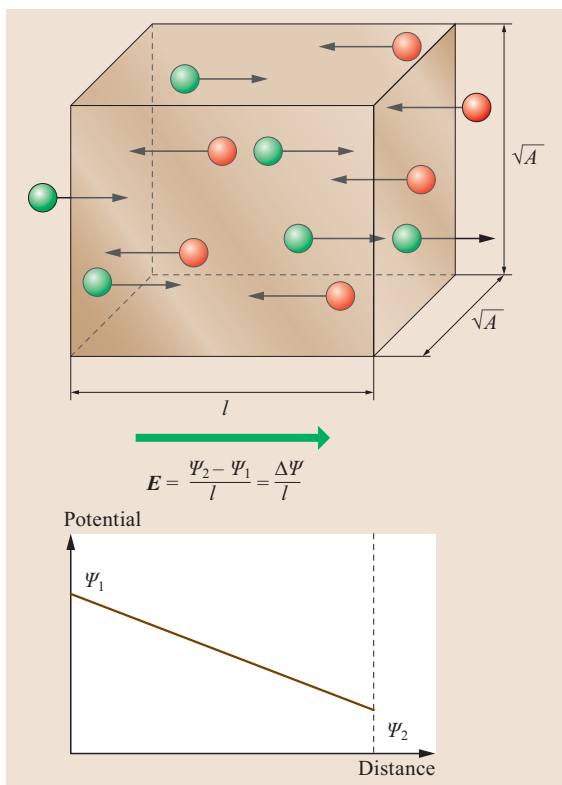


**Fig. 15.9** Schematic definition of ion conductivity in an electrolyte block of length  $l$  and cross-area  $A$ , which is subject to a DC field of  $E$

tute a *secondary solvation sheath*, which is loosely associated with  $\text{Li}^+$  and whose composition is more dynamic [15.39]. As described later in this chapter, the structure of such  $\text{Li}^+$ -solvation sheaths plays critical roles both in defining the interphase chemistry and in dictating  $\text{Li}^+$ -migration after such interphases are formed.

Based on spectroscopic observations and computation, it is generally accepted that  $\text{Li}^+$  can accommodate 3–5 organic solvent molecules in its primary solvation sheath [15.31]. However, little has been known about how  $\text{Li}^+$  interacts with those solvent molecules on an atomistic level, or whether  $\text{Li}^+$  shows preference toward some of the solvent molecules against others. This latter knowledge becomes critical when one tries to understand the manner in which a solvated  $\text{Li}^+$  desolvates in order to intercalate into a host electrode, or a naked  $\text{Li}^+$  solvates while leaving a lithiated host electrode [15.40].

**Ionic Conductivity.** While redox reactions occur within both anode and cathode materials at the influx or exodus of electrons from external circuits during charg-

ing or discharging of the batteries, the electrolytes must act as the ionic reservoir or sink to compensate for any disturbance in electroneutrality therein; thus one of the basic requirements for any electrolytes is the capability to transport ions across the device. Such capability is quantified by ionic conductivity  $\sigma$ , which essentially represents the amount of charge carried by the ions through a cubic unit of electrolyte in unit time under unit electric field (Fig. 15.9).

$$\sigma = \frac{l}{RA} = \frac{JzFA}{\Delta\psi} \frac{l}{A} = \frac{JzF}{X}, \quad (15.7)$$

where  $J$ ,  $z$ ,  $F$  and  $X$  stand for ion flux, ionic valence, Faraday constant and electric field strength, respectively;  $\psi$  is the potential.

Ionic conductivity is defined by an imaginary orientational movement of ions along a (DC) electric field as shown in Fig. 15.10. However, under DC conditions it is very difficult to accurately measure this quantity because of the instantaneous deviation from ideal Ohmic behavior, either caused by the accumulation of charges at electrolyte–electrode interfaces when blocking electrodes are used, or by the slow charge-transfer processes at electrolyte–electrode interfaces when nonblocking electrodes are used. Figure 15.10a,b show the equivalent circuits for both scenarios under DC condition, using a  $\text{Li}^+$ -containing electrolyte as an example. The ion accumulation at interfaces is represented by a double layer and geometric capacitor ( $C_{\text{dl}}$  and  $C_{\text{g}}$ ), and slowed-down ionic migration by additional resistors at interfaces ( $R_{\text{i}}$  and  $R_{\text{ct}}$ ).

EIS methodology provides an effective approach to circumvent the unwanted interferences from these electric components, based on the different relaxation time scales with which each of those components responds to an applied AC field [15.41]. For example, the electronic conduction of the circuits and capacitance would respond at extremely high frequencies ( $> 10^4$  Hz) due to the rapid movement of electrons in metals and relatively fast formation of electrified double layers, while the much slower ion migration within solid electrodes or charge transfer processes, including either ion movement across the interfaces or reduction/oxidation of ionic species at the interfaces, can only occur at extremely low frequencies ( $< 10^2$  Hz). The ion conduction within bulk electrolyte usually lies in the medium frequencies ( $10^2$ – $10^3$  Hz). By applying an AC field at varying frequencies, it is possible to differentiate ion conduction from those above common interferences.

Figure 15.11 graphically shows the basic setup of a typical EIS analysis using blocking electrodes as represented by the equivalent circuit in Fig. 15.10a, where

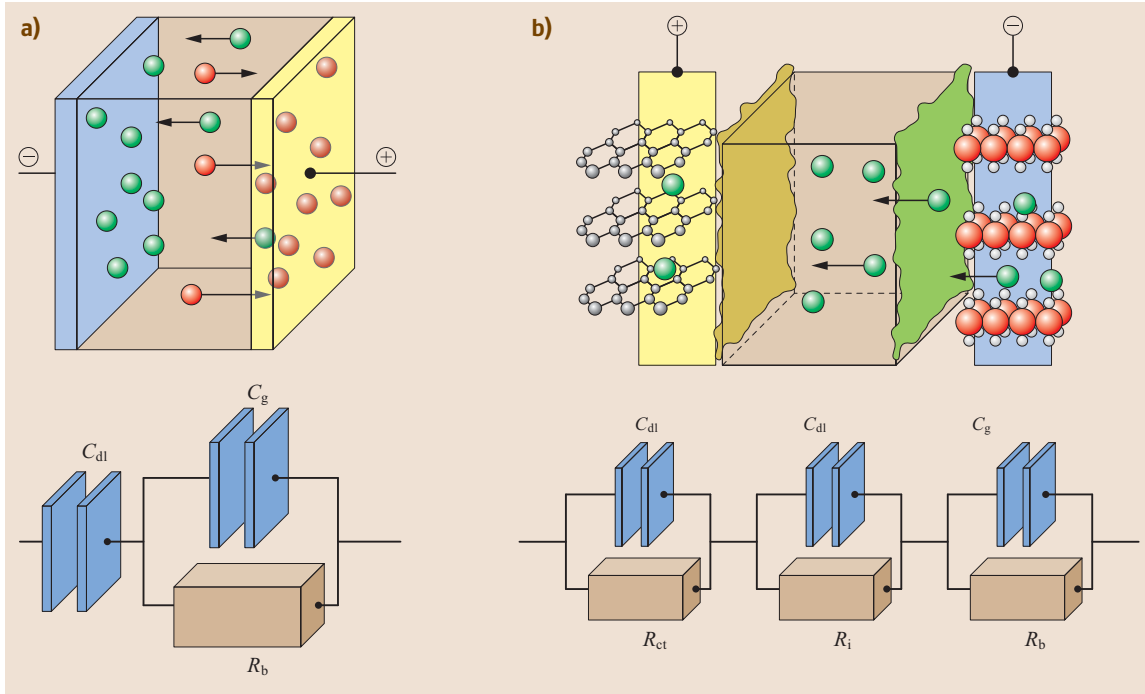


**Fig. 15.10a,b** Under DC conditions, it is impossible to accurately measure the ionic conductivity of an electrolyte ( $\sigma$  corresponding to bulk resistance component  $R_b$ ) due to interferences from capacitances (from double-layer  $C_{dl}$  and from cell geometry  $C_g$ ) and other resistor components ( $R_i$  and  $R_{ct}$ ). **(a)** When blocking electrodes are used, neither cation ( $\text{Li}^+$ ) nor anion can travel across the electrode–electrolyte interfaces, thus accumulating opposite charges at the interfaces and forming a double-layer capacitor. **(b)** When nonblocking electrodes are used, such as in a typical  $\text{Li}^+$ -ion battery, the resistance to  $\text{Li}^+$  crossing electrode–electrolyte interfaces far outweighs that of bulk resistance of the electrolyte. If electrode passivation occurs, additional resistance components would arise, such as from interphases ( $R_i$ )

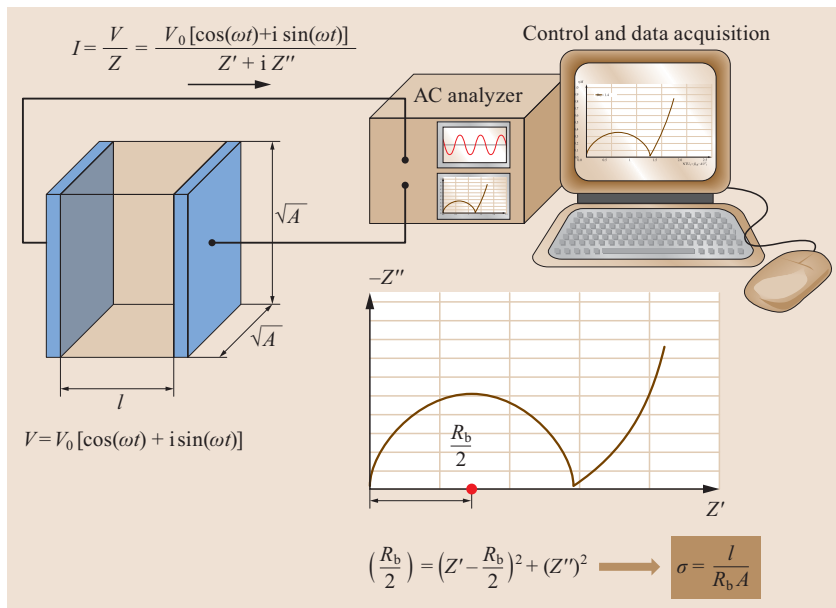


**Fig. 15.11** Graphic illustration of a typical AC impedance analysis setup and the evaluation of ionic conductivity  $\sigma$ . Impedance analyses using AC technology can be used to deconvolute the different contributions from various components, enabling accurate measurement of ionic resistance (or conduction)

a symmetrical cell containing the electrolyte under investigation is subject to a sinusoidal voltage of varying frequency  $\omega$  and constant amplitude  $V_0$ ,

$$V = V_0[\cos(\omega t) + i \sin(\omega t)] . \quad (15.8)$$

The current response  $I$  is recorded as function of  $V$ . Since all electric components will contribute to the overall impedance  $Z$ , which is now a complex quantity, according to Ohmic law

$$I = \frac{V}{Z} = \frac{V_0[\cos(\omega t) + i \sin(\omega t)]}{Z' + iZ''} . \quad (15.9)$$

Solution to the complex equation leads to the real ( $Z'$ ) and imaginary ( $Z''$ ) parts of the overall impedance as

$$Z' = \frac{R_b}{1 + (\omega C_g R_b)^2}$$

and  $Z'' = \frac{\left[1 + (\omega C_g R_b)^2 \left(1 + \frac{C_{dl}}{C_g}\right)\right]}{\omega C_{dl} [1 + (\omega C_g R_b)^2]} , \quad (15.10)$

where  $R_b$  is our goal (bulk electrolyte resistance to ionic movement). Despite their complicated expressions,  $Z'$  and  $Z''$  can be rearranged, after reasonable approximations, into a very useful expression that sets the foundation of practical impedance spectroscopy

$$\left(\frac{R_b}{2}\right)^2 = \left(Z' - \frac{R_b}{2}\right)^2 + (Z'')^2 . \quad (15.11)$$

In other words, when  $-Z''$  is plotted against  $Z'$  on a complex plane, the relation will produce a semicircle that centers at  $(\frac{R_b}{2}, 0)$  on the real axis (Fig. 15.12). Thus the semicircle intercepts the real axis at  $(R_b, 0)$ . In reality, deviation from the ideal equivalent circuit distorts the semicircle, but the basic feature remains, and ionic conductivity should always be evaluated from the intercept of  $Z$  on real axis

$$\sigma = \frac{l}{R_b A} . \quad (15.12)$$

For most liquid electrolyte at room temperature, whose ionic conductivity remains higher than 1.0 mS/cm, the semicircle corresponding to  $R_b$  could *shrink* or entirely merge with the interphase component, and the intercept at the high frequency end is usually used in place of  $R_b$ .

**Lithium Ion Transference Number.** The ionic conductivity determined before includes the contributions from the movements of both cations and anions. In most electrochemical devices, only one ionic species partici-

**Fig. 15.12 (a)** Schematic illustration of the *steady-state current* approach to measuring  $\text{Li}^+$  transference number. At  $t = 0$ , both cation and anion migrate under the DC field and contribute to ionic current; at *steady state*, most anions are accumulated at the electrode surface, while  $\text{Li}^+$  is the only species carrying ionic current because it can travel across the interphase and enter the nonblocking electrode. **(b)** Typical AC impedance analysis setup and the evaluation of the  $\text{Li}^+$ -transference number,  $t_{\text{Li}}$ . The working electrode (WE) must be a nonblocking electrode to  $\text{Li}^+$  so that it can become the only ionic species carrying the current at *steady state* ►

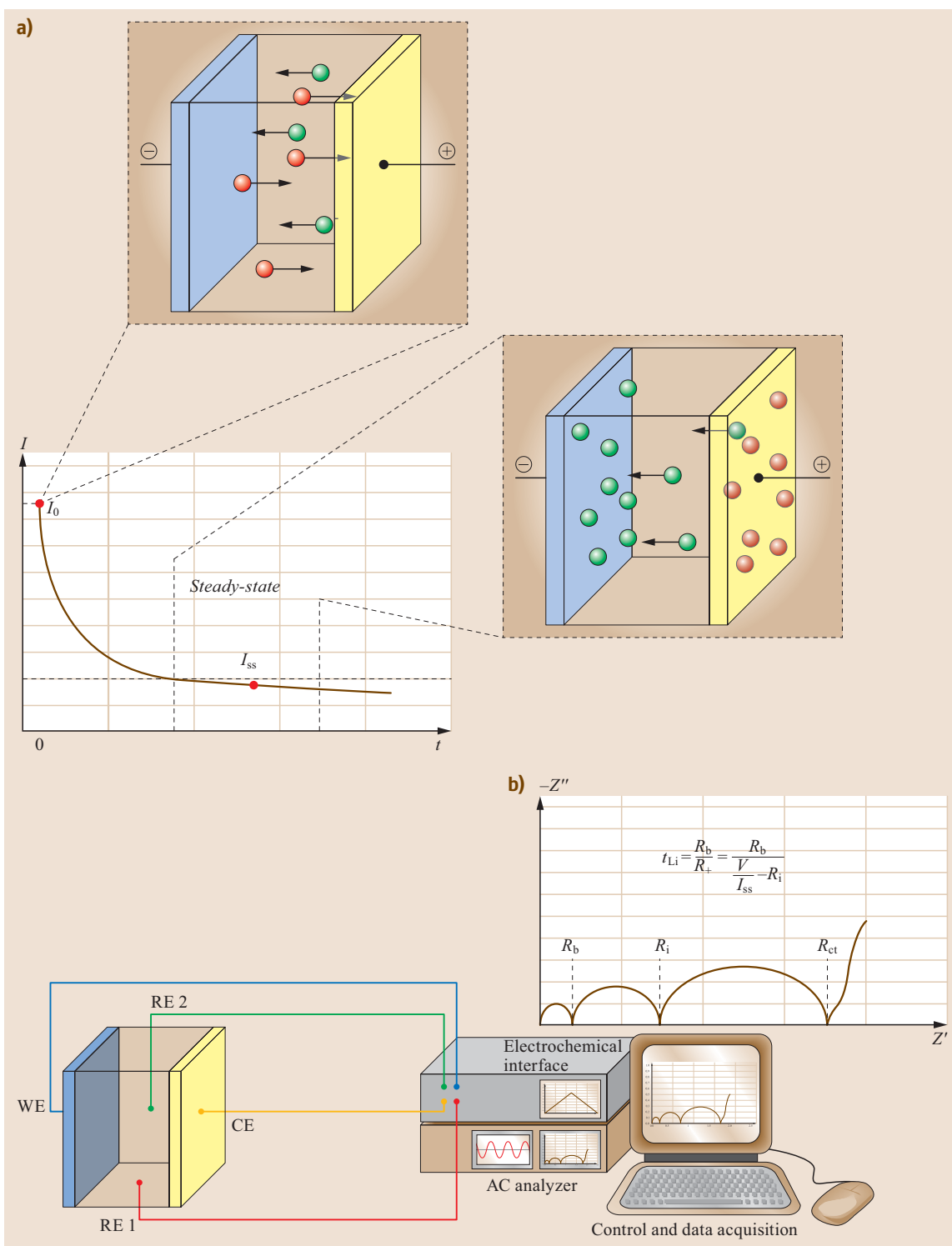
pates in the cell chemistry. For proton fuel cells this ion would be  $\text{H}^+$ , for alkaline fuel cells  $\text{OH}^-$ , and for Li-based batteries  $\text{Li}^+$ . Therefore, sometimes it becomes necessary to know the portion of current that is solely caused by the movement of that ionic species. Thus, ionic transference number is defined as

$$t_+ = \frac{\sum \sigma_+}{\sigma_i} = \frac{\sum \mu_+}{\mu_i} = \frac{I_+}{I_+ + I_-}$$

and  $t_- = 1 - t_+ . \quad (15.13)$

Apparently ion pairs contribute nothing to the overall current and the presence of ion aggregations significantly reduces the available free ions that can carry current.

As one of the smallest cations (radius  $\approx 0.09$  nm),  $\text{Li}^+$  exerts strong Coulombic attraction to solvent molecules in nonaqueous electrolytes, such that on average 4–5 such molecules coordinate with each  $\text{Li}^+$ . This ion-molecule coordination complex is called the *primary solvation sheath*, which remains intact even when  $\text{Li}^+$  moves. Since a solvated  $\text{Li}^+$  far outsizes its less-solvated counter ions and is therefore less mobile, most current through nonaqueous electrolytes is not carried by  $\text{Li}^+$  itself but by the anion [15.42]. While the presence of anion in the electrolyte is indispensable in maintaining global and regional electroneutrality, anionic current is useless for a Li-ion battery device because anions cannot cross interphases and participate in intercalation chemistries (Fig. 15.13). A direct consequence of this parasitic current is the formation of a concentration polarization, which generates additional resistance against  $\text{Li}^+$  conduction. An ideal electrolyte thus should not only show apparent high ion conductivity, but also the maximized  $\text{Li}^+$  conduction, although in reality the overall ion conductivity as measured by impedance techniques has been used to characterize and evaluate electrolytes, with an incorrect implication that it is proportional to  $\text{Li}^+$  conduction.



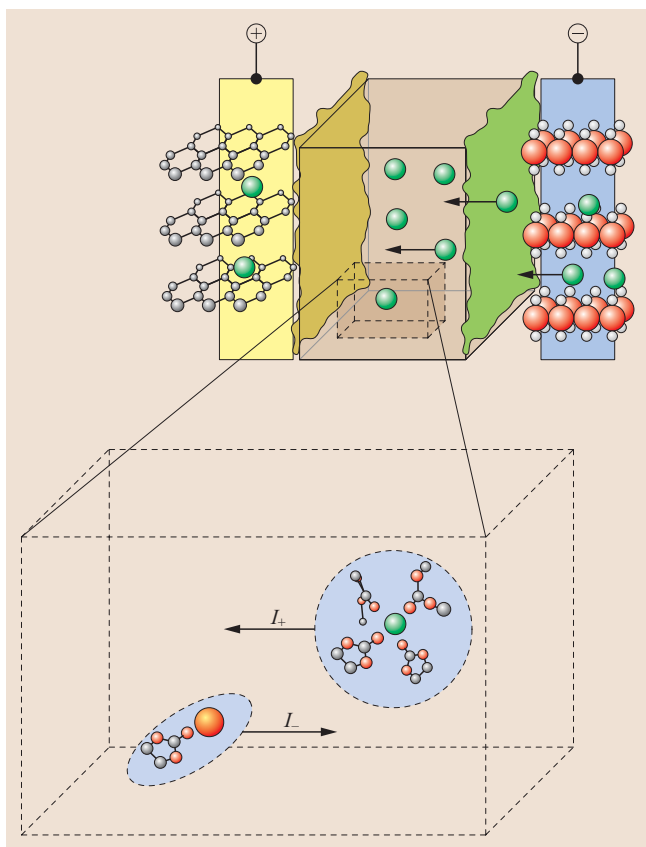


**Fig. 15.13** The ionic current consists of contributions from parallel cationic and anionic movements. Solvated  $\text{Li}^+$  usually moves much slower than its counter ion in nonaqueous electrolytes due to its much larger solvation sheath, hence the cationic transference number is usually less than 0.5

Accurate measurement of  $\text{Li}^+$  transference number is always a topic of controversy. Scattered and even conflicting results are often produced by various methods. The classical *steady-state current approach* was developed by Evans et al., who devised a symmetric cell consisting of two identical Li-metal electrodes (Fig. 15.12a) [15.43]. When a small DC field, e.g., 10 mV, is applied to such a cell, Li is oxidized to  $\text{Li}^+$  at the positively-polarized electrode (cathode), while  $\text{Li}^+$  is reduced to Li at the negatively-polarized electrode (anode). In an ideal scenario, the initial current  $I_0$  consist of both anionic as well as cationic contributions, while after equilibrium is reached, the steady-state current  $I_{ss}$  should only be carried by  $\text{Li}^+$ . Thus,

$$t_{\text{Li}} = \frac{I_{ss}}{I_0}. \quad (15.14)$$

In reality, various complications, especially surface passivation of metallic Li, cause deviation from

the ideal scenario. In order to correct the interference from interphase resistance, Bruce and Vincent coupled the techniques of DC polarization and AC impedance so that the interphase resistances before and after the steady state is accounted for. Figure 15.12b shows the typical setup for the electrochemical impedance spectrum (EIS) to measure interphase resistances, where an additional electrochemical interface is needed to generate and control precisely the DC potential across the test cell. Because nonblocking electrodes are used, the equivalent circuit would be similar to what Fig. 15.11b shows, and the resultant impedance plot,  $-Z''$  versus  $Z'$  on a complex plane, would consist of two or three adjoining semicircles, depending on the relative magnitudes and characteristic frequencies of bulk and interphase resistor components. Figure 15.12b schematically illustrates an ideal scenario where all three resistor components ( $R_b$ ,  $R_i$  and  $R_{ct}$ ) are well resolved.

Bruce and Vincent noticed that  $R_i$  increases as the cell is being polarized, which reflects the growth of the passivation layer on metallic Li as a consequence of the reaction between the electrolyte and the freshly deposited Li crystal on the anode. They modified the definition of  $\text{Li}^+$  transference number

$$t_{\text{Li}} = \frac{\frac{1}{R_+}}{\frac{1}{R_+} + \frac{1}{R_-}}, \quad (15.15)$$

where  $R_+$  and  $R_-$  are resistance to cation ( $\text{Li}^+$ ) and anion movements, respectively. Obviously the overall ion conduction can be viewed as cationic and anionic currents in parallel circuits

$$\frac{1}{R_b} = \frac{1}{R_+} + \frac{1}{R_-}, \quad (15.16)$$

then

$$t_{\text{Li}} = \frac{R_b}{R_+} = \frac{R_b}{\frac{V}{I_{ss}} - R_i}, \quad (15.17)$$

where  $V$  is the applied DC potential in both DC and AC experiments,  $R_b$  and  $R_i$  the first and second intercept on the impedance plot, respectively, and  $I_{ss}$  the steady-state current obtained from DC experiment.

A more popular form of the same practice is

$$t_{\text{Li}} = \frac{I_{ss}(V - I_0 R_0)}{I_0(V - I_{ss} R_{ss})}, \quad (15.18)$$

where  $R_0$  and  $R_{ss}$  are the interphase resistances at  $t = 0$  or at steady-state, respectively. For most nonaqueous liquid and polymer electrolytes investigated with this



approach, the  $\text{Li}^+$  transference number ranges between 0.2–0.4, confirming the fact that solvated  $\text{Li}^+$  is a less mobile species as compared with its counter anion.

Besides the above DC-polarization combined with AC impedance approach, there are several variations based on galvanostatic polarization or electromotive force, but so far none is perfect in terms of accuracy and easiness, while all involve more or fewer assumptions and arbitrariness. For example, the determination of  $I_{ss}$  value, which constantly decays (Fig. 15.12a), varies depending on the individual judgment by the experimentalist.

Different from electrochemical approaches that consider long-range movement of ions, nuclear magnetic resonance (NMR) can probe local mobility of these ions (as long as the nucleus of each interested ionic species is NMR sensitive), thus providing a means to evaluate the  $\text{Li}^+$  transference number

$$t_{\text{Li}} = \frac{\mu_+}{\mu_+ + \mu_-} = \frac{D_+}{D_+ + D_-}, \quad (15.19)$$

where  $\mu$  and  $D$  stand for mobility and diffusivity of individual ionic species, respectively. A commonly used technique, pulse field gradient NMR (PFG-NMR), can directly measure translational self-diffusivities of  $^7\text{Li}$  and its anions (such as  $^{31}\text{P}$  in hexafluorophosphate  $\text{PF}_6^-$ ,  $^{19}\text{F}$  in *bis*(trifluoromethanesulfonyl)imide (TFSI), or  $^{11}\text{B}$  in tetrafluoroborate  $\text{BF}_4^-$  or *bis*(oxalato)borate (BOB) [15.44]. In contrast to the electrochemical methods described above, NMR independently monitors both anion and cation; however, this advantage is somewhat diluted by the fact that all ions in the same species are monitored, whether they are free, in ion pairs or in aggregations. Considering that ion pairs do not contribute to ion conduction and aggregations causes reduction in net ionic current, the ionic self-diffusivities as obtained by PFG-NMR are generally overestimated

$$D_{\text{obs}} = xD_{\text{ion}} + (1-x)D_{\text{pair}}. \quad (15.20)$$

Unfortunately, this overestimation becomes substantial for electrolytes of practical salt concentration ( $\approx 1.0\text{ M}$ ), where the ion-ion interaction is expected to be significant.

A modified NMR technique, electrophoresis NMR (eNMR), sought to differentiate the mobile ionic species from those not participating in orientational movement by applying a DC field on the investigated solution while monitoring spin-echo relaxation of  $^7\text{Li}$  and other nuclei under pulse gradient conditions. Figure 15.14 shows one of the designs for eNMR experiments, in which the drift velocity of  $\text{Li}^+$  and a chosen nucleus of its anion can be measured. The  $\text{Li}^+$  transference number obtained in this manner should be closer to

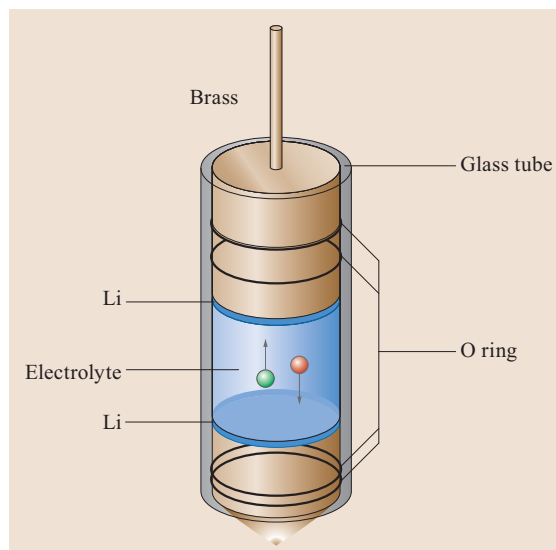


**Fig. 15.14** eNMR tube for  $\text{Li}^+$ -transference number measurement, where the relative diffusivities of each individual nucleus can be directly measured under the DC field based on their relaxation times

reality [15.45]. Despite the widely scattered data available in the literature, the general agreement is that in nonaqueous electrolytes the  $\text{Li}^+$  transference number is less than half, reaffirming the knowledge that  $\text{Li}^+$  is the less mobile species [15.31, 46].

In addition to the difficulty of measuring the  $\text{Li}^+$  transference number accurately, the limited usage of this quantity for characterizing and evaluating electrolytes is also attributed to its insignificant influence over the electrochemical performances of the device. As mentioned above, the concentration polarization built up by transport and accumulation of counter ions introduces additional resistance to  $\text{Li}^+$  conduction; however, in most liquid electrolytes, this concentration polarization could be easily eliminated through convection and self-diffusion. Only in more viscous media such as polymer electrolytes, or at subambient temperatures, could the small  $\text{Li}^+$  transference number be a factor that significantly affects the device performance.

### Interphase Processes: Formation Stage

The characterization of interphase formation has been especially challenging due to the fact that an effective and noninvasive in situ technique is still unavailable. EIS, dilatometry and in situ x-ray diffraction (XRD) are such few rare tools, but each with their individual restrictions. Although most information provided by ex situ techniques such as FTIR, XPS NMR and (TEM)/SEM proved useful and in many cases critical

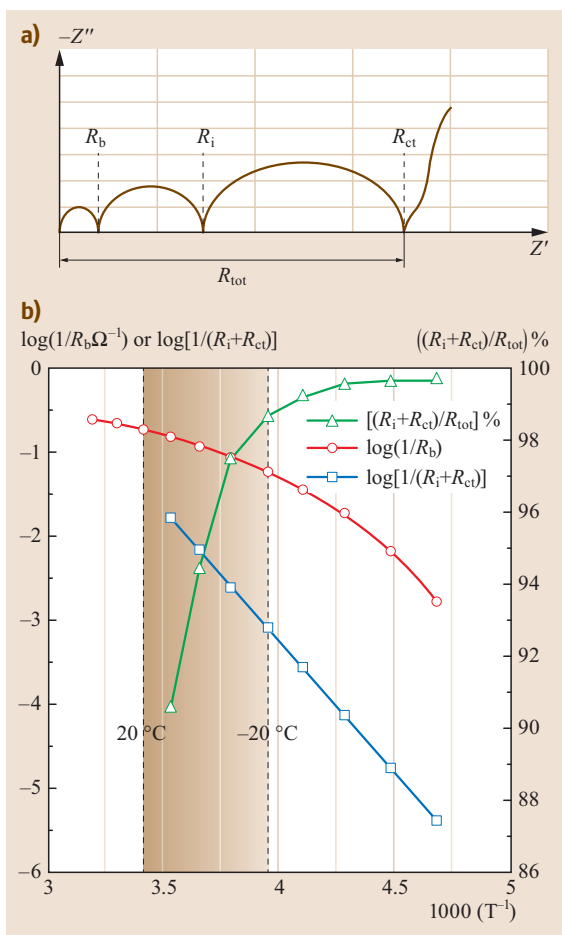


**Fig. 15.15a,b** Interphase resistance constitutes the main kinetic control over cell chemistry by limiting  $\text{Li}^+$  transport rate. **(a)** Schematic breakdown of contributions to overall cell impedance from various bulk and interphase components. **(b)** Resistances of these components measured in a Li-ion cell with  $\text{LiCoO}_2$  and MCMB chemistry in 1.0  $\text{LiPF}_6/\text{EC}/\text{EMC}$  electrolyte at different temperatures

in understanding interphase formation, their invasive nature always cast a shadow of suspicion over the possibility that the actual interphase had been altered during the sample preparation stages, both chemically and morphologically.

From the previous section we have shown that the interphase causes constant interference in the accurate measurement of transport properties in the bulk electrolyte (ion conductivity, ionic transference number). Indeed, more than 90% of the overall cell impedance ( $R_{tot}$ ) comes from the interphase contribution ( $R_i + R_{ct}$ ), as Fig. 15.15 shows, especially under low temperatures [15.47].

The existence of an interphase on the graphitic anode in Li-ion batteries has been proven beyond any doubt, and in the past two decades ample understanding has been achieved. Early ex situ surface analyses by Aurbach and coworkers established the substantial presence of alkylcarbonates in the anode interphase with spectroscopic signatures (e.g., absorption at  $1350\text{ cm}^{-1}$  in FTIR and binding energy at 289 eV for C1s electrons in XPS) [15.48, 49]. The alkylcarbonate is likely the product of an incomplete reduction route pathway from the carbonate solvents. This incomplete reduction was attributed to a single-electron mechanism, primarily due to the poor electron availability during the interphase formation on graphitic anodes [15.50]. More sophisticated diagnosis, performed recently using isotope  $^{13}\text{C}$  labeling and high precision FTIR in combination with quantum chemistry (QC) computation, further identified two additional pathways involving acyl-O cleavage and radical recombination, leading to the presence of oxalate and alkoxide species [15.51].

Polymerization might also appear in some scenarios, leading to speculation that interphases actually consist of those inorganic Li salts embedded in the matrix of amorphous polymeric; although it should be pointed out that the polycarbonate structure proposed is actually not thermodynamically stable and tends to lose  $\text{CO}_2$  to form the more favored poly(ethylene oxide). Most likely the polymeric species present in interphase is a random copolymer of polycarbonate and polyether. Despite the wide variety of compounds identified, it seems that alkylcarbonate remain the majority interphase species in most cases.

A rather controversial component in the interphase is  $\text{Li}_2\text{CO}_3$ . While organic carbonate can undergo a complete two-electron reduction leading to  $\text{Li}_2\text{CO}_3$ , its presence in the anode interphase has usually been attributed to be the consequence of moisture invasion rather than electrochemical reduction. With an elegant XPS experiment Edstrom et al. showed how the binding energy of carbonyl C1s shifts from 289 eV to  $> 290\text{ eV}$  upon controlled exposure to ambient, indicating a fast conversion of alkylcarbonate to  $\text{Li}_2\text{CO}_3$ . They suggested that, since alkyl-carbonates are extremely sensitive to moisture, any less than rigorous handling of the samples could lead to misinterpretation [15.52].

Unlike the chemistry, the understanding of the morphology or structure of the interphase is less understood. Peled speculated a mosaic pattern, with inorganic and organic microregimes patterned randomly, while Kanamura proposed a more organized structure of organic and inorganic layers situated closer to or remote from the electrode surface, respectively. The most detailed work was performed by Bar-Tow et al. [15.53], whose XPS analysis on basal and edge facets of

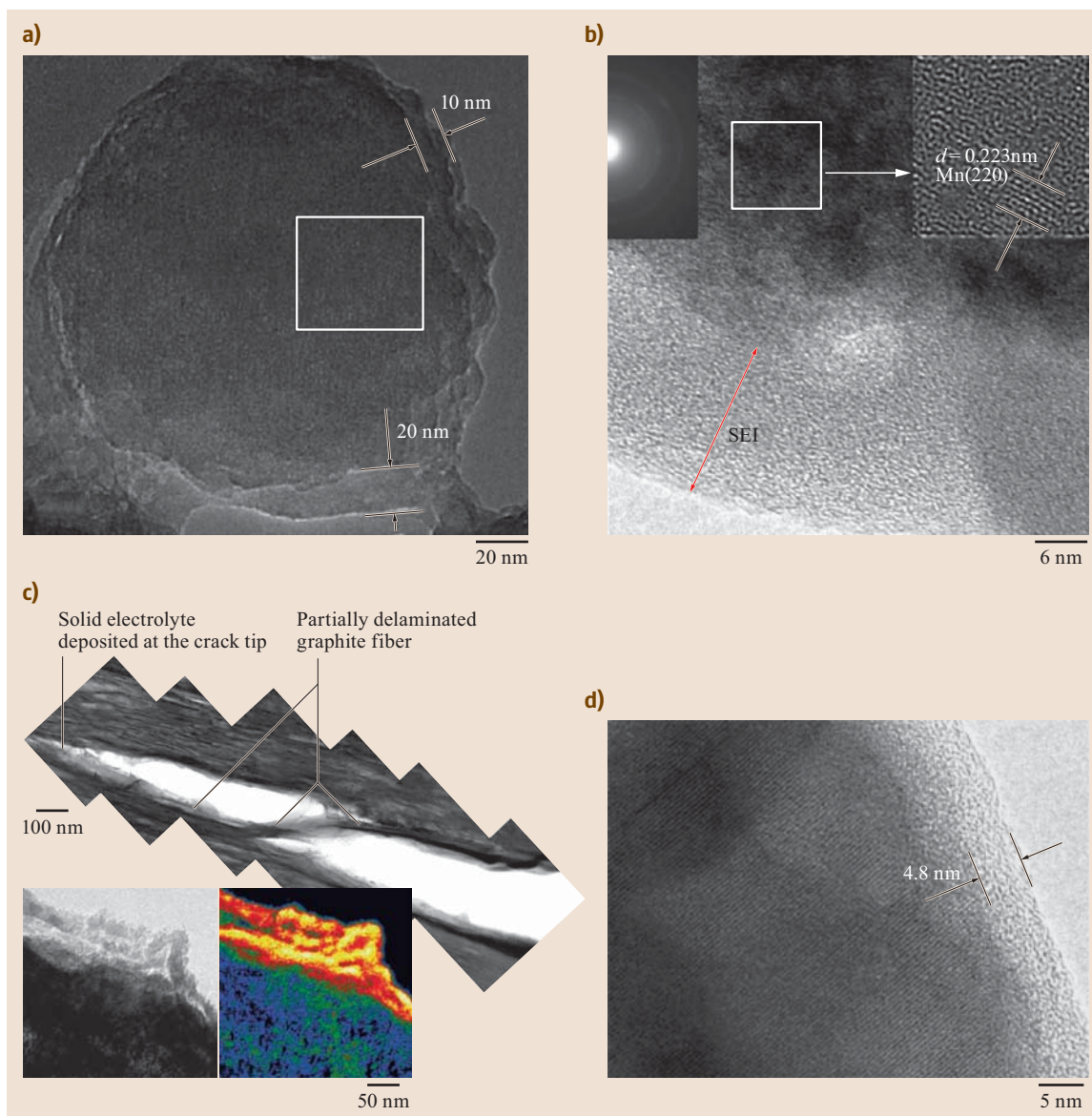


**Fig. 15.16a–d** TEM images of SEI layers grown on anodes and cathodes after cycling in nonaqueous electrolytes. **(a)** Hard carbon sphere; **(b)** a partially exfoliated graphite sheet still connected by a string of graphene sheets that has been covered with an SEI; and **(c)** bright-field TEM graph of a cycled graphitic anode and its corresponding  $\text{Li}^+$ -concentration map

graphite placed the former as an inorganic-enriched and the latter as an organic-enriched region.

The structured interphase was further confirmed by recent work by *Lu* and *Harris* [15.54] who employed isotopic  $^6\text{Li}$  and  $^7\text{Li}$  to label the interphase and bulk electrolyte, respectively, and found that interphase can be roughly divided into two regions:  $\approx 5$  nms of *diffuse* layer that is close to the electrolyte side and that can be penetrated with bulk electrolyte, and  $\approx 15$  nms of *dense*

layer on the current collector side that only desolvated  $\text{Li}^+$  can migrate into.

In recent years TEM has become an increasingly popular tool employed to image interphases. The amorphous nature of interphases usually appear in strong contrast to the crystalline electrode bulk, however, its instability under electron beam makes the imaging a nontrivial task. Figure 15.16 shows interphases observed on several carbonaceous anodes after cycling in

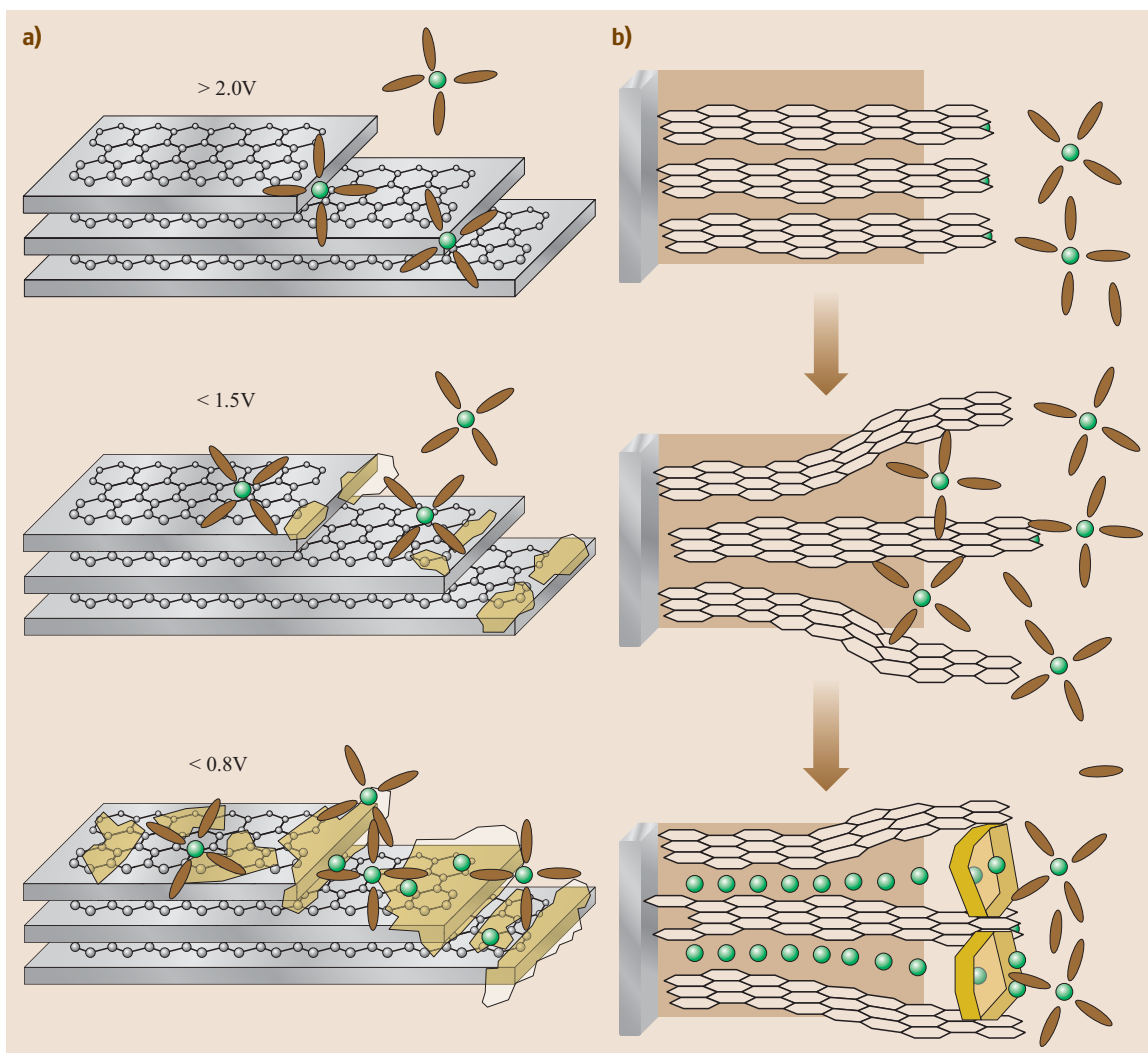


**Fig. 15.17** (a) Schematic drawing of AFM imaging of interphase formation: Two basic characteristics of interphase formation on graphitic surface, i. e., stepwise and region-differentiation (after [15.55]) (b) Schematic drawing of 3-D formation mechanism proposed by Besenhard et al. (after [15.56])

electrolytes, whose thickness of 10–50 nm agrees with the general estimate from other techniques [15.33, 34].

In-depth understanding of the interphase formation mechanism on graphite has been achieved as result of intense investigation since the 1990s. This formation process involves close interaction between graphite and electrolytes; therefore it is specific both to the properties of the electrode (graphitic lattice structure) and electrolyte ( $\text{Li}^+$ -solvation shell).

Pioneering AFM work by Farrington and coworkers [15.55] revealed the two most conspicuous characteristics of interphase formation on graphite that differs from typical electrodes in conventional electrochemistry, i. e., stepwise and regiospecific. Fig-

ure 15.17a schematically summarizes their observations. While interphase species start to accumulate at edge sites at high potentials ( $\approx 1.0$  V), the basal plane remains clean until much lower potentials. This stepwise formation provides the possibility that certain electrolyte components could be preferentially reduced at edge sites prior to other components, thus giving the Li-ion industry valuable leverage to manipulate interphase chemistry via the use of additives [15.55].

The early dilatometry studies indicated large volume expansion during the first lithiation process, leading Besenhard et al. to propose a 3-D mechanism that is schematically depicted in Fig. 15.17b [15.56]. The essential element of this model is that a solvated  $\text{Li}^+$



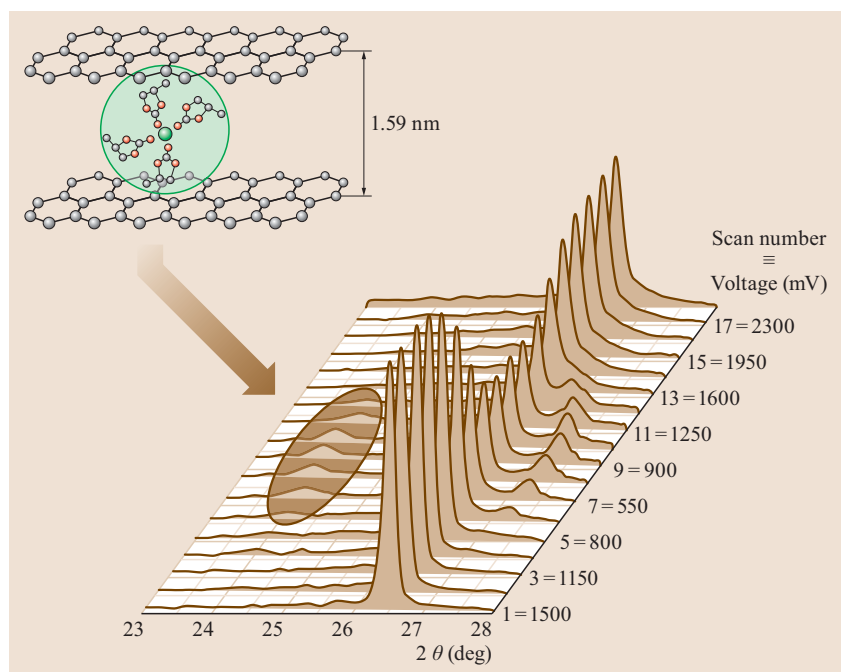


**Fig. 15.18** Transient existence of ternary GIC captured by in situ XRD of graphitic anode cycling in PC-based electrolytes. The peaks at  $2\theta = 24^\circ$  correspond to an interlayer distance of approximately 1.5 nm, a gap that is wide enough to accommodate a solvated  $\text{Li}^+$  with 3–4 solvation sheath members (after [15.57])

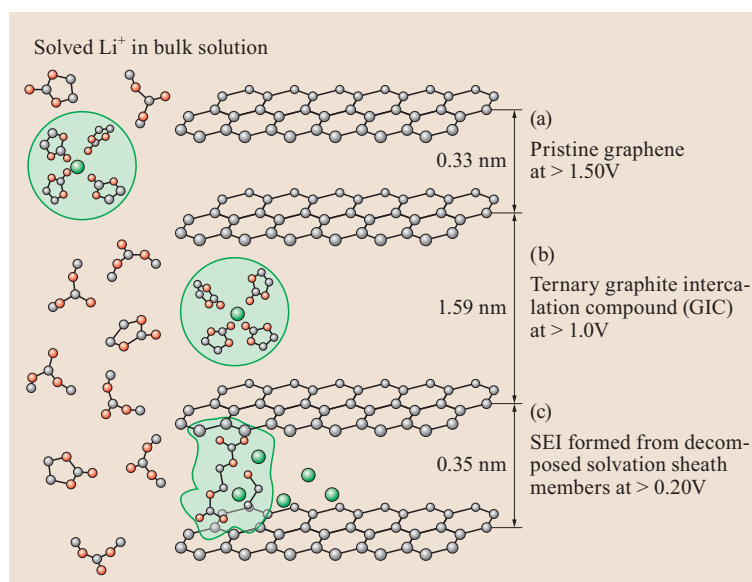


**Fig. 15.19** Schematic illustration of the *solvation-driven* model for interphase formation mechanism. (a) Above 1.50 V the pristine graphite maintains the original interlayer distance of 0.33 nm; (b) While solvated  $\text{Li}^+$  intercalates above 1.0 V, this distance widens briefly to  $\approx 1.59$  nm, accommodating the bulky solvated  $\text{Li}^+$  and forming the ternary GIC; (c) The solvent members in the solvated  $\text{Li}^+$  break down reductively, forming the precursor of SEI, and the interlayer distance of graphite reverts back to  $\approx 0.35$  nm, which would remain during the subsequent lithiations (after [15.58])

intercalates into graphite before interphase formation, thus the eventual interphase would partially penetrate into the interior of graphite from the edge sites. Although circumstantial evidence from electrochemical impedance studies and surface analyses with FTIR, NMR and Raman already favor this *3-D mechanism*, the most direct support comes from the capture of the intermediate graphite intercalation compound (GIC) by in situ XRD, as shown in Fig. 15.18, in which the

smaller angle peaks during the transient cointercalation of propylene carbonate (PC) above 0.5 V versus Li indicates a interlayer distance of  $\approx 1.6$  nm [15.57]. It was speculated that similar cointercalation by other carbonate molecules should happen, except these ternary GICs are too short-lived before the solvent molecules decompose reductively into interphase. A more recent refinement of the 3-D mechanism was made by Xu et al. [15.58], who suggested that the  $\text{Li}^+$ -solvation-

sheath structure plays a critical role in determining the chemical composition of interphases (Fig. 15.19). Thus, any preferential solvation of  $\text{Li}^+$  by an electrolyte solvent would cause unsymmetrical contributions from electrolyte components to the resultant interphase chemical composition. This uneven distribution of the chemical sources of the SEI had been observed earlier via FTIR and NMR [15.58, 59].

The interphase on the cathode remains a topic of debate. Systematic TEM observations made by *Li* and coworkers did reveal the presence of an SEI on certain materials, but absence of it on others (Fig. 15.16) [15.33, 34]. It seems the complication arises not only from the different chemical natures and operating voltages, but also from less controllable factors such as preparation route, porosity, and surface morphology. A surface-catalytic mechanism was speculated, but experimental evidence is still weak, calling for more investigation. What seems to be rational is multiple mechanisms that depends on both chemical state and potential of the cathode, i.e., the interphase nature would be determined by what component of the cathode is exposed to electrolytes: An oxygen layer that nucleophilically attacks solvent molecules at low potential, or a transition metal core layer that reacts electrophilically with solvent molecules at high potential.

#### Post-Formation: Transport Across Interphases and Growth

Once interphase is formed, it acts as a thin-layer solid electrolyte at the edge sites of graphite, allowing  $\text{Li}^+$  migration but insulating electrons (at least under normal operating conditions). Its  $\text{Li}^+$  conduction is known but is far from being well understood, as almost no effort has been made to accurately measure the conductivity. The only experiment that sheds light on the  $\text{Li}^+$  movement across SEI was performed by *Lu* and *Harris*, who used isotopic  $^6\text{Li}$  and  $^7\text{Li}$  to form SEI and bulk electrolyte separately, and then monitored the exchange of these two isotopes upon immersion [15.54]. It was observed that after short exposure ( $\approx$  mins),  $^6\text{Li}^+$  already immobilized in interphase can be swapped by  $^7\text{Li}^+$  in the bulk electrolyte, suggesting a *Grotthuss-like* conducting mechanism as illustrated in Fig. 15.20a. The computational simulation further revealed possible mechanisms as to how a  $\text{Li}^+$  is coordinated within the interphase. Using crystalline  $\text{Li}_2\text{CO}_3$  as a matrix, *Qi* et al. suggested that the transport energy barrier could be significantly reduced if a moving  $\text{Li}^+$  sees a series of transition states with penta- or tetra-coordinated O-ligands [15.60]. This would only happen when this  $\text{Li}^+$  replaces another  $\text{Li}^+$  in its original position, otherwise a longitudinal direct diffusion would encounter much higher energetic barriers (Fig. 15.20b).

The dense interphase not only insulates against electron tunneling, but also prevents solvent molecules from diffusing across it; thus, desolvation must occur at the electrolyte–interphase junction when a solvated  $\text{Li}^+$  migrates to a graphitic anode during lithiation (charge of Li-ion cell). *Ogumi* et al. were the first to realize that  $\text{Li}^+$  desolvation creates additional resistance when a graphitic anode is being charged, thus explaining the unsymmetrical property of Li-ion cells of fast discharging but slow charging [15.61, 62]. *Xu* et al. [15.63] went further to deconvolute the contribution from  $\text{Li}^+$  desolvation to the overall cell resistance by using a nearly SEI-free electrode, and concluded that  $\text{Li}^+$  desolvation could constitute the significant part of the activation energy barrier to  $\text{Li}^+$  migration across the interphase.

Even after SEI formation, it was speculated that SEI does not stop growing all together. This *leaking* nature of the SEI has been confirmed with various evidence of electron tunneling under given circumstances, such as the redox reaction of overcharge-protection shuttles at high voltages, the *Li-ion flow battery* concept, and the ever-increasing impedance at elevated temperatures [15.64, 65]. Even with normal operation, the SEI still continues to grow, at a rate that varies with the voltage, temperature and chemistry of the interphase itself. *Dahn* and coworkers [15.66, 67] developed a high-precision Coulometry technique to monitor this *parasitic* process. Assuming that all irreversible capacities are consumed to make up the SEI, they showed that under a given temperature and similar electrochemical history, the SEI grows at a rate defined by

$$\frac{dx}{dt} = \sqrt{\frac{k}{2}} t^{-\frac{1}{2}}. \quad (15.21)$$

This parabolic relation states that mathematically the growth of SEI never stops; instead, it can only be slowed down (by reducing  $k$ ) with effective electrolyte additive use or with better matching between electrode and electrolytes. In reality, *Smith* and *Burns* et al. [15.66, 67] observed with their high-precision coulometry that irreversible loss on most anode materials requires at least 25 cycles to stabilize asymptotically.

#### Additives

There are many additives used in state-of-the-art electrolytes, but descriptions in the open literature are rather limited. They can be roughly classified into three groups:

1. Interphase additives
2. Overcharge protection additives
3. Safety-trigger additives [15.35].



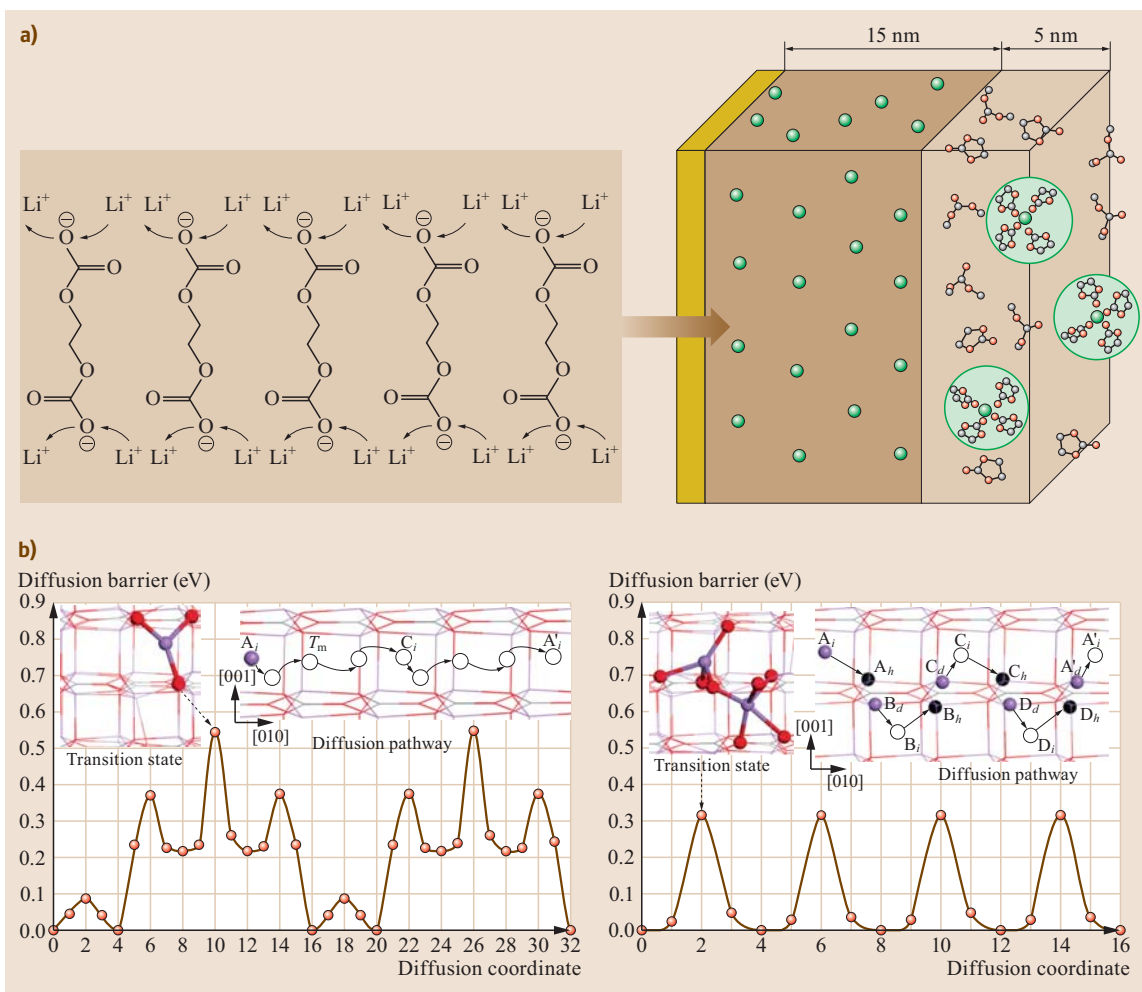


**Fig. 15.20** (a) Grothuss-like transportation mechanism of  $\text{Li}^+$  across an interphase. It was proposed that the dense layer of interphase is impenetrable for solvent molecules, so that solvated  $\text{Li}^+$  has to desolvate and exchange with the  $\text{Li}^+$  already in the interphase (after [15.54]). (b) Computation simulations depict the corresponding energy barriers of direct longitudinal  $\text{Li}^+$  diffusion through an interphase and Grothuss-like mechanism where  $\text{Li}^+$  is better stabilized. The tetra- or penta-coordinated transition states available only in the latter case effectively reduce the barrier height (after [15.60])

While interphase additives are almost entirely consumed in the forming cycles of Li-ion batteries, overcharge protection additives exist inertly in the electrolyte and can only be activated at high potentials when the cells are overcharged by creating an internal soft-short within the cell. Safety-trigger additives, on the other hand, are activated only once, whose consequence is to end the cell life under certain conditions (high voltage, elevated temperatures, excessive rate etc.), in order to evade a catastrophic scenario.

The concept of *interphase additives* was established on the basis that an interphase on an electrode in Li-ion batteries is formed when the potential of the electrodes changes gradually. This stepwise nature makes

it possible to manipulate the chemistry by using certain ingredients that can react before bulk electrolyte components can. The purpose of manipulating interphase chemistry versus that of a *natural grown* is to make the interphase thinner and more conductive. The sacrificial additives are used at rather small concentrations, so that their presence is completely consumed after the decomposition upon the initial cycling.

Although theoretically additives should have electrochemical signatures upon decomposition, an effective additive leaves little trace behind. Such an example is vinylene carbonate (VC), whose high reduction potential on graphite was only speculated, while neither cyclic voltammetry nor differential capacity derived from gal-

vanostatic experiments yields any evidence of this reduction. Thus, quantum chemistry (QC) computation was usually resorted to to predict their decomposition potential and possible products. A popular approach employed is to calculate energy levels of the highest occupied molecular orbital (HOMO) and lowest unoccupied molecular orbital (LUMO), based on the belief that the ingredient with the lower LUMO serves as a better electron donor and therefore will be selectively reduced, while the higher HOMO makes a better electron acceptor and selective oxidation is expected [15.68]. For SEI chemistry designed for graphitic anodes, compounds of low LUMOs are sought after, and plethora of LUMO/HOMO data have been reported in the literature with different levels of computations, providing useful guidelines. However, it must be emphasized here that, despite the theoretical appearance of this approach, the selection based on HOMO/LUMO information is still semiempirical, because the compound that is reduced at higher potential does not necessarily lead to a more stable interphase. So far computational chemistry still cannot accurately predict the physicochemical properties of the decomposed products.

Compared with its anode counterparts there is less understanding of interphases on cathode surfaces, and in certain cases even its existence is under debate. It was believed though that once the cathode operates at potentials beyond 4.5 V, surface depositions do occur, and probably an interphase-like layer could exist. With the introduction of 5 V class cathode chemistries such as  $\text{LiMn}_{1.5}\text{Ni}_{0.5}\text{O}_4$  (LMNO, 4.6 V) and  $\text{LiCoPO}_4$  (LCP, 4.8 V), the research on additives for cathodes also became active [15.69, 70]. Fluoroalkyl phosphates and alkylthiophenes have been reported as effective in stabilizing nonaqueous electrolytes on these high voltage cathode materials [15.71], while sulfones and nitriles were also used as high voltage stable electrolyte solvents [15.72, 73].

*Overcharge protection additives* are also known as *redox shuttles*. They were so chosen that their activation potentials rest slightly above the normal operating potentials of the cathode. In case of overcharge, these additives are oxidized on the cathode surface, and the products subsequently migrate to the anode surface where they receive electrons and reduce back to their original form. The overall thermodynamics would dictate that the dissipation of excessive energy would be in the form of heat, so that cathode materials would not be moved to a higher energy level by this excessive energy, otherwise over-delithiation of the cathode would result in hazardous reactive decomposition [15.74, 75]. Most of the reported additives under this category are based on aromatic compounds, whose activation potential can be tuned with the location and the chemistry of ring

substitutes. Since the rate of energy dissipation depends on both the solubility and diffusivity of these additives, these additives might not be effectively enough to handle the overcharge under high rates. Additionally, the heat engendered by the *soft short* tends to warm up the device, and the integration of these additives into large format Li-ion cells or battery packs will still need to be thoroughly investigated.

Differing from *interphase* and *overcharge protection additives*, *safety-trigger additives* are designed to be activated only when the cell is on the verge of a catastrophic failure, and the activation marks the end of cell life. These are usually of *gas-generating type*, such as polyphenyl compounds, which build high pressures at high voltages or temperatures and force the cells to open in a mild manner. Many additives under this category remain trade secrets of battery manufacturers or electrolyte suppliers.

### 15.2.3 Separators

The separator is an essential component for liquid electrolyte and polymer gel electrolyte battery cells. It is generally a porous membrane placed between the positive and negative electrode to prevent physical contact of the electrodes. The liquid and gel electrolytes are absorbed into the pores of the separator and serve as the media for the transport of ions accompanied by the reaction between the two electrodes. The separator itself does not participate in the reaction, however, it critically affects the cell performance, especially the power capability and safety. The essential properties required for a separator are mechanical strength, thickness and porosity for ionic conductivity, and chemical and thermal stability for cycle life and safety. Since many of these properties are fundamentally opposed to each other, a separator with an optimum combination of these properties is needed for Li-ion batteries.

In standard Li-ion batteries, the microporous polyolefin membrane has been most widely used as the separator. In the current market, there are two types of separators, dry-processed and wet-processed, based on the process of pore-forming as shown in Fig. 15.21, both of which are made of either polyethylene (PE) or propylene (PP) [15.76, 77]. The dry-processed membranes have an orientated pore structure and tensile strength, while the wet-processed membranes contain a tortuous pore structure and isotropic tensile strength. From the viewpoint of pore structure, the open and straight pores favor fast ionic transport while the tortuous pores favor preventing the growth of Li dendrites. Therefore, the dry-processed membranes are more suitable for high power batteries, while the wet-processed membranes for long cycle life batteries.

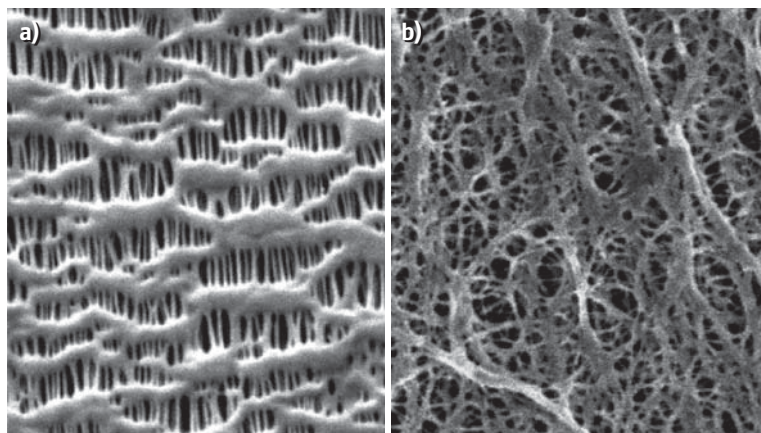


**Fig. 15.21a,b** SEM images of two types of polyolefin separators. **(a)** Celgard membrane by dry process, and **(b)** tone membrane by wet process (after [15.76, 77])

For safety reasons, thermal shutdown and ceramic separators have been developed for Li-ion batteries. The shutdown separator is a multilayer structural membrane with a PE layer laminated between two PP layers. Its shutdown function is based on a difference in the melting points of PE and PP. Since PE has a lower melting point ( $mp = 125\text{--}135^\circ\text{C}$ ) than PP ( $mp = 160\text{--}165^\circ\text{C}$ ), the PE layer is able to shutdown cell current by closing its pores to prevent ionic transport at the temperatures above the melting point of PE while the PP layers still retains dimensional integrity when the temperature is lower than the melting point of PP. Therefore, the shutdown separator protects the cell only in the temperature range between the melting points of PE and PP. Ceramic separators are also multilayer structural membranes with a porous ceramic layer coated on the surface of one or two sides of a porous polyolefin membrane, where the polyolefin membrane can be a porous membrane or a porous nonwoven cloth. The ceramic separator has excellent dimensional integrity at elevated temperatures because of the negligibly thermal expansion of the ceramic coating.

A variety of evaluations have been applied to the separator of Li-ion batteries, which can be classified as the two aspects of structure and property. The structural evaluations include thickness and porosity. The thickness determines the distance for ionic transport between the two electrodes, whereas the porosity affects uptake of liquid electrolyte and consequently the ionic conductivity in the membrane. The porosity can be evaluated directly by measuring porosity, pore size, pore distribution and orientation of the membrane, or indirectly by measuring gas permeability and gurley across the membrane. Property evaluations include the chemical and electrochemical stability against the cell's conditions, especially at the charged state, the wettability (contact angle), wetting rate, and retention of liquid electrolyte, mechanical stability such as puncture strength and ten-

sile strength, and thermal behavior such as shutdown temperature and dimensional integrity (or shrinkage) at elevated temperatures. Detailed descriptions on the measurements can be found in [15.76, 77].

With advances in technologies and the ever-increasing importance of Li-ion batteries, various in situ techniques have been employed in combination with real-time electrochemistry to observe the dynamic chemistries and processes inside a operational Li-ion battery. The information and the understanding of the failure mechanisms provide valuable feedbacks to the synthesis of new battery materials and cell engineering. This section briefly summarizes this emerging front.

#### 15.2.4 Advanced/In Situ Spectroscopy

There are limited numbers of in situ tools that are noninvasive, noninterfering, and operative in the same chemical environments as Li-ion batteries. As described in the section on ionic conductivity, the AC method of EIS is one of the few that meet these stringent requirements; however, the trade-off is that the information is usually too nonspecific, because a working Li-ion cell is a complicated system that involves many electrochemically-active parts contributing to AC stimulus, such as  $\text{Li}^+$  movements in bulk electrolyte, across electrolyte-electrode interphases, and within both cathode and anode bulk, etc. Accurate deconvolution of individual contributions from these components is nearly impossible even with sophisticated model equivalent circuits; therefore so far EIS remains a tool for phenomenological analysis [15.78].

##### AC Impedance Analyses/Electrochemical Impedance Spectroscopy

Differing from ion conductivity or transference number measurements, the cell impedance for an active battery varies significantly with the chemical state of the elec-

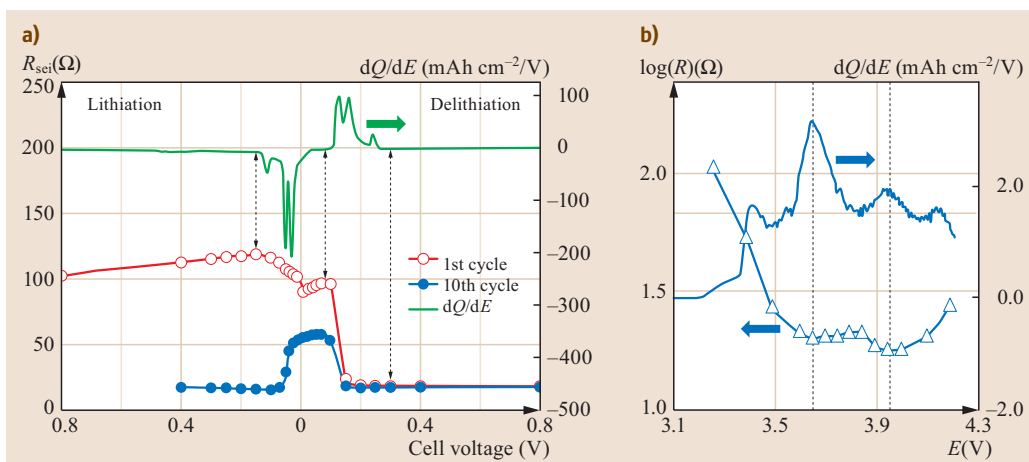


**Fig. 15.22a,b** In situ impedance spectroscopy of Li-ion electrodes under electrochemical cycling. **(a)** Graphitic anode that shows complete lithiation–delithiation cycles before and after the formation of SEI; and **(b)** a full Li-ion cell based on the same graphite anode and a  $\text{LiNi}_{0.85}\text{Co}_{0.10}\text{Al}_{0.05}\text{O}_2$  cathode. The overall cell resistance is obviously the combination of the interphase resistance and phase changes within the electrodes, complicated with SEI formation processes (after [15.79, 80])

trodes; therefore it is critical to precisely control the potential of the working electrode (WE) in order for the data be comparable. In the previous section we have shown the basic setup for EIS (Fig. 15.11), in which a four-electrode configuration is recommended for the electrochemical cell (although three- or even two-electrode alternatives are usually adopted experimentally). While the potential between WE and RE 1 is held at certain preset values by the electrochemical interface, an AC signal of varying frequencies is generated by the impedance analyzer, and impedance responses are recorded and analyzed. Figure 15.22a shows the interphase resistance measured on a graphitic anode during a complete lithiation–delithiation cycle, before and after the formation of the interphase, and Fig. 15.22b shows the corresponding full Li-ion cell with the same graphite anode and  $\text{LiNi}_{0.85}\text{Co}_{0.10}\text{Al}_{0.05}\text{O}_2$  cathode [15.79, 80]. However, it is not always possible to unambiguously separate interphase components. More often than not overall impedance of Li-ion cells was adopted as an indicator of how the kinetics of electrochemical reactions evolves with cell aging. Nevertheless, EIS still provides a rare means to peek into the elusive interphase formation process.

#### In Situ Synchrotron XRD Studies

In situ diffraction (XRD) studies of an operating Li-ion cell are desirable in order to directly relate the structure of the electrode material to the voltage of the cell and the corresponding level of Li intercalation. However, this level of analyses is often not available through conventional x-ray sources, due to either awkward ge-

ometries or low penetration depth of the x-rays. The latter is of particular concern for an intercalation reaction in which the surface may differ significantly from the bulk. Synchrotron facilities, on the other hand, provide high energy x-ray beams that are strong enough to *see* through ordinary stainless steel coin cell hardware, thus making it possible to continuously perform diffraction studies while the Li-ion cells operate. The information revealed paints dynamic pictures of how electrode bulk structure changes when responding to external electrochemical or thermal stimuli, thus allowing us to evaluate cycling stability as well as safety features of these materials more accurately.

An excellent description of the utility of the synchrotron technique relative to a conventional x-ray source has been given by Mukerjee et al. [15.81]. The high resolution of the synchrotron enables accurate lattice constant determination along with the observation of the development and disappearance of single- and multiphase regions as Li is intercalated into or out of the electrode material. An example from Mukerjee et al. is shown in Fig. 15.23. From the measurement at many increments along the charge curve, a two-phase region was observed. An example of the electrochemical data and its corresponding XRD pattern as a function of state of charge is shown in Fig. 15.24 [15.82]. In this study the authors documented a *crystallization delay* in which the  $\text{FePO}_4/\text{LiFePO}_4$  ratio appears to be lower than what should be observed based on counting the number of coulombs during the charge. This observation may result from of an unobservable amorphous intermediate phase.

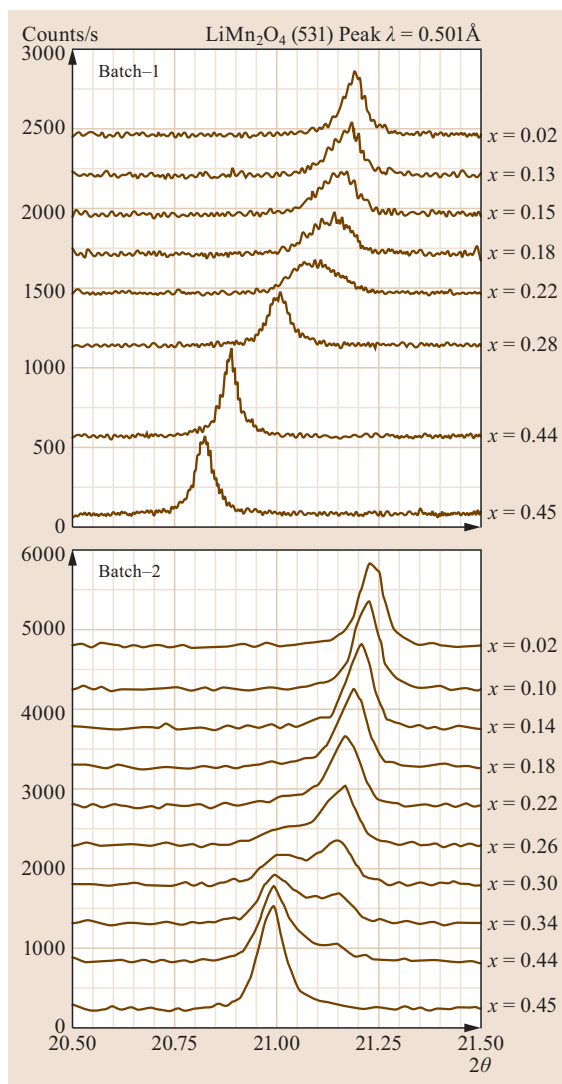


**Fig. 15.23** An example of synchrotron x-ray diffraction data showing the 531 peak of  $\text{LiMn}_2\text{O}_4$  during charge of the electrode material. A distinct two-phase region is observed at  $x = 0.30$ , and  $x = 0.34$  (after [15.81])

A more recent example of in situ XRD was conducted by Sun et al., in which the thermal stability of concentration gradient cathode material was evaluated. High resolution diffraction peaks were continuously collected on a fully delithiated sample (4.3 V) while the sample experienced a thermal ramping from RT up to  $370^\circ\text{C}$  (Fig. 15.25a) [15.83]. The contour plot in Fig. 15.25b summarizes the structural spectra of such nanostructured Ni-Mn-Co mixed layer oxides in response to the rising temperature. It is clearly seen that (101) peaks (located at  $2.57^\circ$ ) start low angle shift at  $\approx 110^\circ\text{C}$ , indicating a major phase transformation of

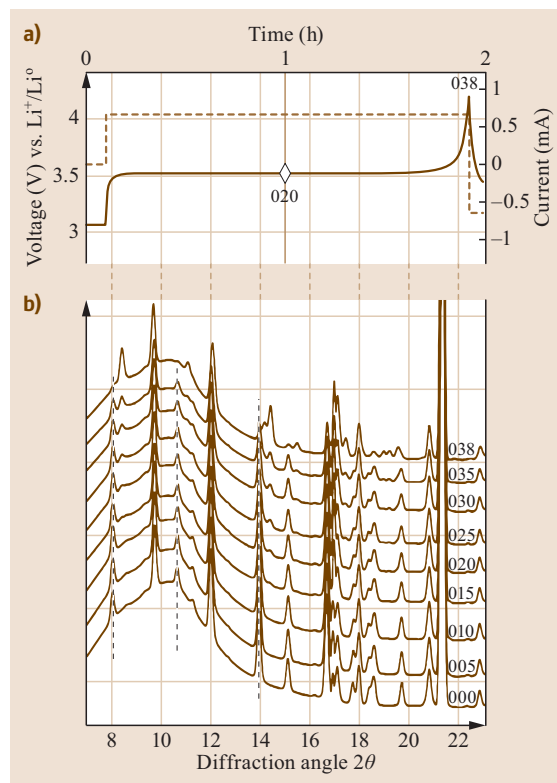


**Fig. 15.24a,b** An example of synchrotron XRD patterns recorded during the operation of charging  $\text{LiFePO}_4$  (after [15.82])

these oxides. Although this structural degradation is not necessarily associated with onset of a safety runaway, it could result in loss of electrochemical performance. The level of complexity and relevance of the information obtained on these reactive materials in this single experiment are unprecedented.

#### In Situ High Resolution Transmission Electron Microscopy

A dream for battery chemists has been to directly observe what transpires at the micro-/nanoscopic scale when electrochemistry proceeds in a battery. In situ transmission electron microscope TEM techniques may have made this dream a reality with reasonable approximations.

Modern high resolution TEM (HRTEM) has enabled visualization at subangstrom scales, but since all electronic microscope must work under high vacuum, the application of it on an operating battery has not been straightforward because of the liquid electrolyte. While state-of-the-art battery packaging may maintain its hermeticity under high vacuum, the packaging materials themselves (stainless steel or aluminum alloy



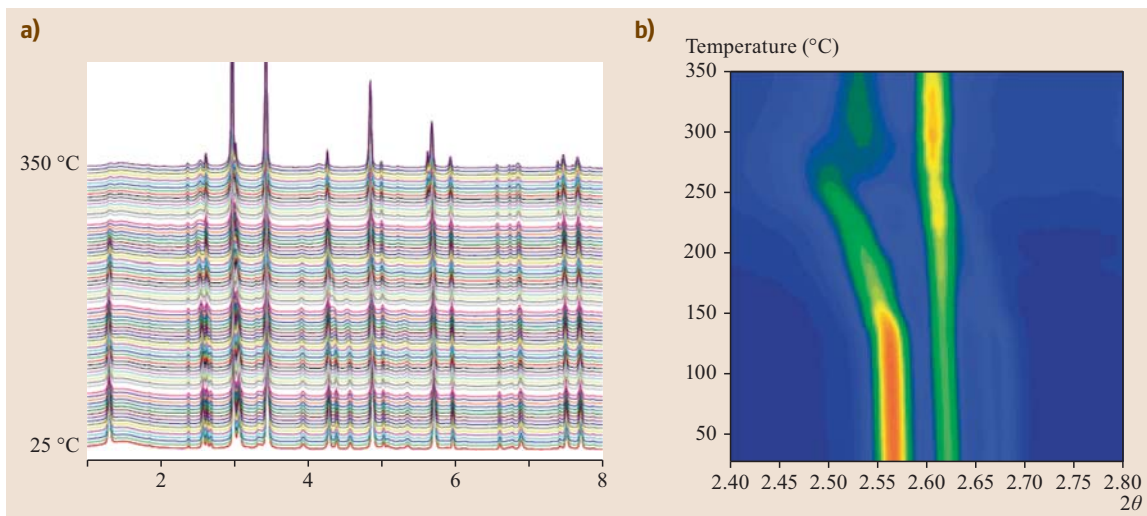


**Fig. 15.25** (a) In situ high-energy x-ray diffraction profiles of a delithiated cathode in the presence of a nonaqueous electrolyte; (b) contour plots showing the phase transformation occurring above 110 °C as indicated by the shift as well as peak abundance of (101) peak (after [15.83])

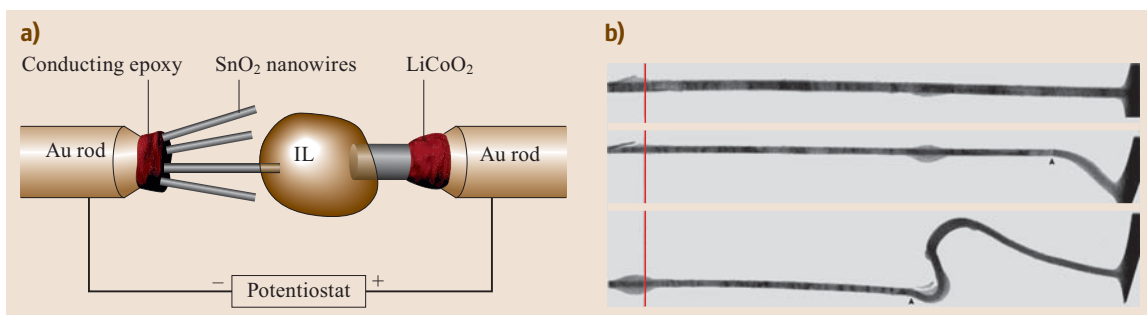


**Fig. 15.26a,b** In situ TEM graphs showing lithiation of a  $\text{SnO}_2$  nanowire in ionic liquid-based electrolyte. (a) Instrumental setup; (b) volume expansion of  $\text{SnO}_2$  nanowire and propagating of amorphous phase upon lithiation (after [15.84])

casing) serve as strong electron barriers that prevent imaging. On the other hand, light plastic packaging materials such as those used in pouch cell configurations cannot survive the high vacuum condition although they do allow electron transmission. To circumvent these issues, Huang et al. [15.84] constructed inside a TEM chamber a nanosized battery that employs ionic liquid based on pyrrolidinium *bis*(trifluoromethane sulfonyl)imide salt as electrolyte and  $\text{SnO}_2$  nanowire and  $\text{LiCoO}_2$  nanoparticle as anode and cathode respectively (Fig. 15.26a). The nonvolatile nature of ionic liquid enables direct visualization of this nanosized electrochemical cell without any casing. In the virgin experiment of this technology, they observed real-time images of  $\text{SnO}_2$  nanowire during lithiation–delithiation, as shown in Fig. 15.26b, where a reaction front moves longitudinally along the wire, while the swelling caused by lithiation of Sn turns the wire spirally into *Medusa's*

*hair*. This mechanical stress has been responsible for the well-known poor cycling reversibility of  $\text{SnO}_2$  anode materials. The same group has used this setup to visualize other anode materials such as aluminum and silicon that face the same challenges.

Because the ionic liquid electrolyte differs from its liquid counterparts used in real-life batteries in terms of electrochemical stability, certain aspects such as interphase chemistry and processes cannot truthfully revealed by the above technique. On the other hand, TEM is not really a noninvasive tool to battery materials, as the electron beam can inflict damage on the target, especially organic materials such as ionic liquids or the SEI grown on the electrode surface. Therefore it should be kept in mind that the in situ observation in this case is under the interference from the observer. Alternative approaches need to be developed so that conditions approximating real-life Li-ion batteries more closely may



be realized while electron beams are shed to image the electrochemical process.

### NMR Techniques

Nuclear magnetic resonance (NMR) has been used to study various nuclei in different chemical environments for a long time. With the high abundance of NMR-active  $^7\text{Li}$  nuclei in nature ( $\approx 93\%$ ), its application in the battery field is well represented by the works of *Greenbaum et al.* and *Grey et al.*, with the former reputed for characterization of interphase components and  $\text{Li}^+$ -transport phenomena in liquid electrolytes, and the latter for local structure of  $^7\text{Li}$  in transition metal oxide cathode. Chapter 12 by *Tong* also gives a detailed discussion of electrochemical NMR.

NMR is noninvasive to all battery components, but its application on an operating battery is difficult. The earliest such attempt was made by *Gerald et al.* who designed a toroid cavity cell and fit it into a wide-bore magnet so that  $^7\text{Li}$ -NMR could be recorded to monitor the lithiation–delithiation of carbonaceous materials [15.85]. Such a configuration does not well simulate a realistic Li-ion battery, and also severely restricts the signal-to-noise ratio. Because almost all of the more interesting activities of  $\text{Li}^+$  in a live battery are in the solid rather than liquid phases (migration across the interphases or diffusion within cathode and anode bulk materials), the resulting featureless, broad signals often impose hurdles for meaningful analysis and understanding. The effective convention of narrowing solid NMR signals, i. e., magic angle spinning (MAS), is not easily applied to an operating battery, because the need for rotating the sample at high speed (1–70 kHz) not only makes it physically difficult to maintain electric contacts for the current collectors, but will cause cell failures due to electrolyte depletion under the centrifugal force. Nevertheless, efforts are being made to overcome these technical difficulties, and in near future in situ NMR is expected to reveal more helpful information about battery materials in operation.

*Grey et al.* developed a combined approach of MAS/ex situ as well as static/in situ NMR [15.86]. Their setup is shown in Fig. 15.27a, where a plastic-packaged pouch electrochemical NMR cell was constructed. Using this realistic cell configuration, they have investigated the lithiation process of Si anode materials and attempted to quantify the growth of metallic Li dendrites, respectively. Figure 15.27b describes the dynamic  $^7\text{Li}$  signal for a crystalline Si anode during its initial lithiation. This study demonstrated that in situ techniques can capture certain Li processes that cannot be resolved with ex situ NMR. The future application of in situ NMR to other battery processes can be expected.

### Scanning Probe Microscopy

Scanning probe microscopy (SPM) covers a range of microscopic techniques where a physical tip is moved by piezoelectric actuators to probe the sample surface in a manner of raster scan, so that surface images of the sample could be generated by monitoring and analyzing the tip-surface interaction. The most conspicuous examples from the SPM family are scanning tunneling microscopy (STM), which measures the electronic current between the surface and the tip, and atomic force microscopy (AFM), which measures mechanical force and has been shown to be useful in characterizing the height change of and SEI growth on the graphitic anode in electrolyte.

A more useful variation of the technique is electrochemical strain microscopy (ESM), which records ionic flow between the tip and sample surface with a periodic bias applied, so that the  $\text{Li}^+$  distribution can be mapped dynamically on the nanoscale. Figure 15.28a,b shows the basic setup and application of this technology to various Li storage materials [15.87, 88].

One aspect that needs to be emphasized is that the electrochemical conditions under which Li-ion batteries operate cannot be precisely applied to the ESM tip, therefore questions as to whether these measurements simulate real cell situation were often raised. For example, with large bias (12 V) alternating at high frequency, the local electrochemical environment that a  $\text{Li}^+$  feels and the subsequent intercalation–deintercalation could involve experimental artifacts. Further development is needed to fully establish ESM as a useful technique for researchers in the community.

### Acoustic Emission

A rather unexpected but surprisingly informative in situ technique is acoustic emission measurement. *Ohzuku et al.* were perhaps the first to point out that the acoustic events accompanying the mechanical stress between the reacted and unreacted regions of electrode materials could be used to monitor in situ electrochemical reactions in these materials, and their pioneering work using acoustic emission (AE) on electrolytic manganese dioxide proved that acoustic events are closely associated with particle fracturing upon initial lithiation [15.90]. After a hiatus of a decade, researchers' interest in this technique is renewed due to the advantage of its intrinsic passive nature (hence nondestructive) and high sensitivity. The more interesting work was performed on materials of emerging chemistries such as Sn-, Si- as well as conversion reaction electrodes.

*Rhodes et al.* applied it to investigate the deleterious volume changes in crystalline Si electrodes and performed the first rigorous waveform analysis (Fig. 15.29a), where the duration, amplitude, counts

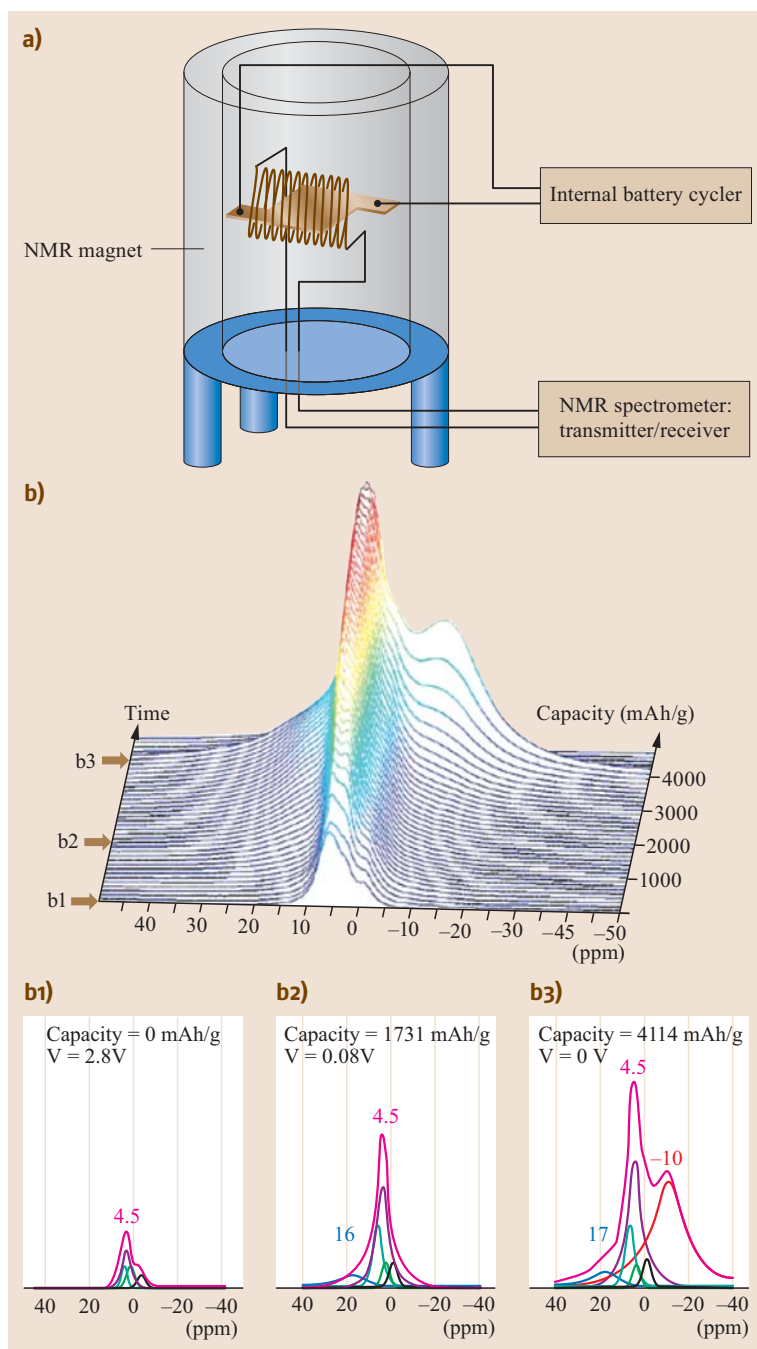


**Fig. 15.27** (a) Schematic setup of  $^7\text{Li}$ -NMR study on a crystalline Si anode under electrochemical lithiation. (b) Stacked plots of  $^7\text{Li}$  spectra obtained and the deconvolution at various states of charge (after [15.86])

and frequency were correlated with corresponding electrochemical information so that AES can not only tell when an event occurs but also what it is [15.89]. It was found that the initial lithiation of Si is accompanied with the largest number of emissions, mainly caused by surface fracture of Si particles, while in the subsequent charging–discharging cycles, the emis-

sion events are characterized by distinct bursts, reflecting reversible volume expansion–contraction due to formation or disappearance of various  $\text{Li}_x\text{Si}$  alloy phases (Fig. 15.29b). In combination with modeling studies, they concluded that maximum tensile stress occurring at the particle surface is responsible for the largest acoustic events at the initial lithiation. Appar-

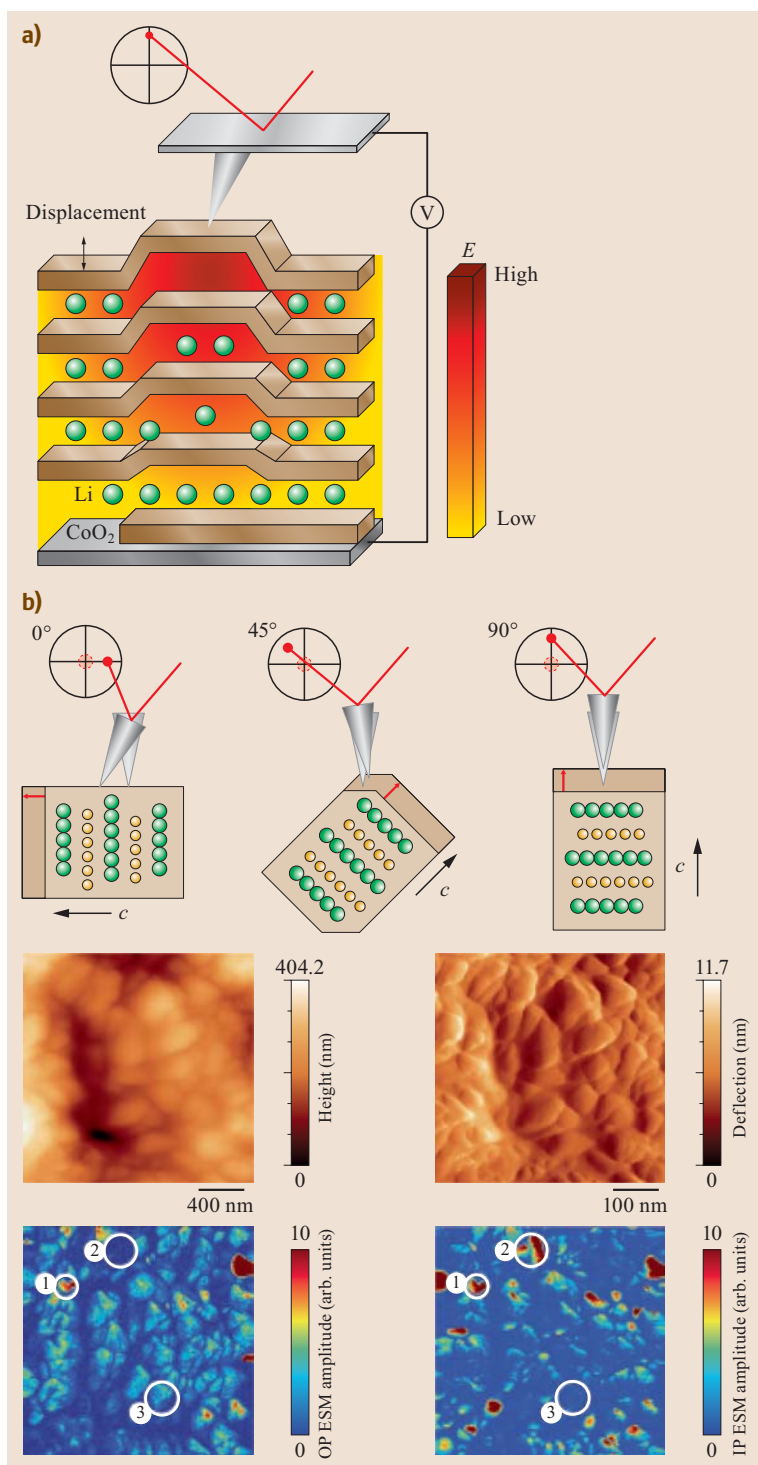


**Fig. 15.28** (a) Schematic illustration of SPM probe applied on an intercalation electrode; (b) SPM experiments on electrode surfaces (after [15.87, 88])

ently, the most severe challenge of Si-based electrodes comes from the initial lithiation process, where not only the crystalline Si turns amorphous to accom-

modate the incoming  $\text{Li}^+$ , but also new surfaces created in the process induce consumption of electrolyte solvents and  $\text{Li}^+$  as reflected by the irreversible capacity

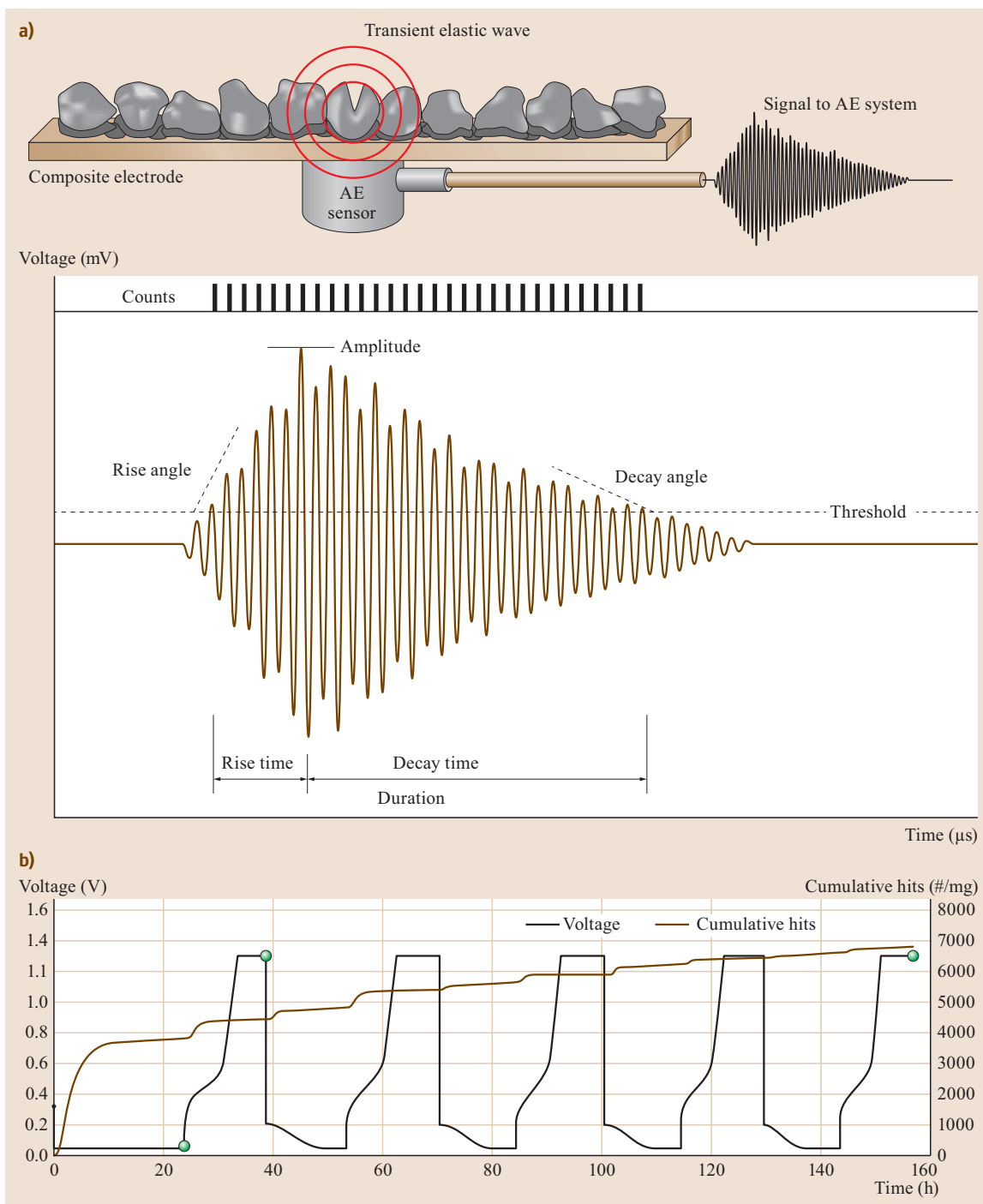


**Fig. 15.29** (a) Schematic drawing of in situ acoustic emission measurement on an Si electrode and the waveform analysis. (b) The voltage profile of an Si electrode cycled in cell and the cumulative acoustic emissions during the cycling (after [15.89])

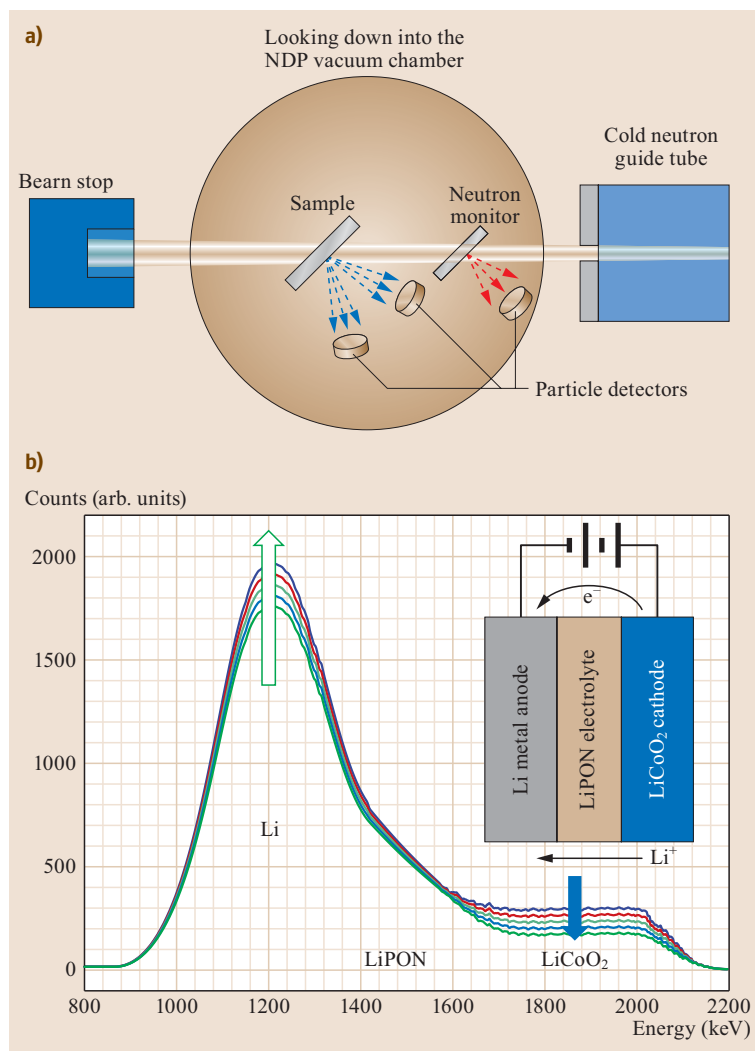


**Fig. 15.30** (a) The setup of a neutron diffraction experiment. (b) Time-resolved in situ neutron diffraction on a thin film battery during charging. The electrode and electrolyte layers are assigned in the spectra. Arrows indicate the flow of Li in each electrode (after [15.91], courtesy of American Chemical Society)

loss. The volume change certainly causes mechanical stress, which can be solved through cell engineering, but to compensate the loss in the first cycle calls for excessive amounts of  $\text{Li}^+$  and electrolyte solvents and ultimately leads to high surface impedance. This vicious cycle has to be addressed before practical deployment of Si in actual Li-ion devices can be realized.

### Neutron Techniques

An underexplored in situ tool is neutron techniques, apparently due to its limited availability to most potential users. In fact, the sensitivity of neutron techniques to light atoms such as Li makes it a unique complement to TEM, while the low energy (meV) of cold neutrons makes it an essentially nondestructive probing particle that can monitor the dynamic distribution

of  $\text{Li}^+$  throughout the battery during electrochemical reactions.

In *neutron depth profiling*, space- and time-resolved depth profiles of  $\text{Li}^+$  in a Li-ion battery configuration can thus be obtained by bombarding the target with an incoming neutron of 4 meV. Figure 15.30a shows such a typical setup at the National Institute of Standards and Technology (NIST), where the neutron interacts with  $^6\text{Li}$  in different electrochemical environments producing a tritium and an  $\alpha$  particle



Tritium and  $\alpha$  particles travel diagonally away from the interaction center, and their energy level reveals the ionic and electronic structures of the matrix where the interaction occurs. The initial locations of the interaction can be traced back using the recorded stopping

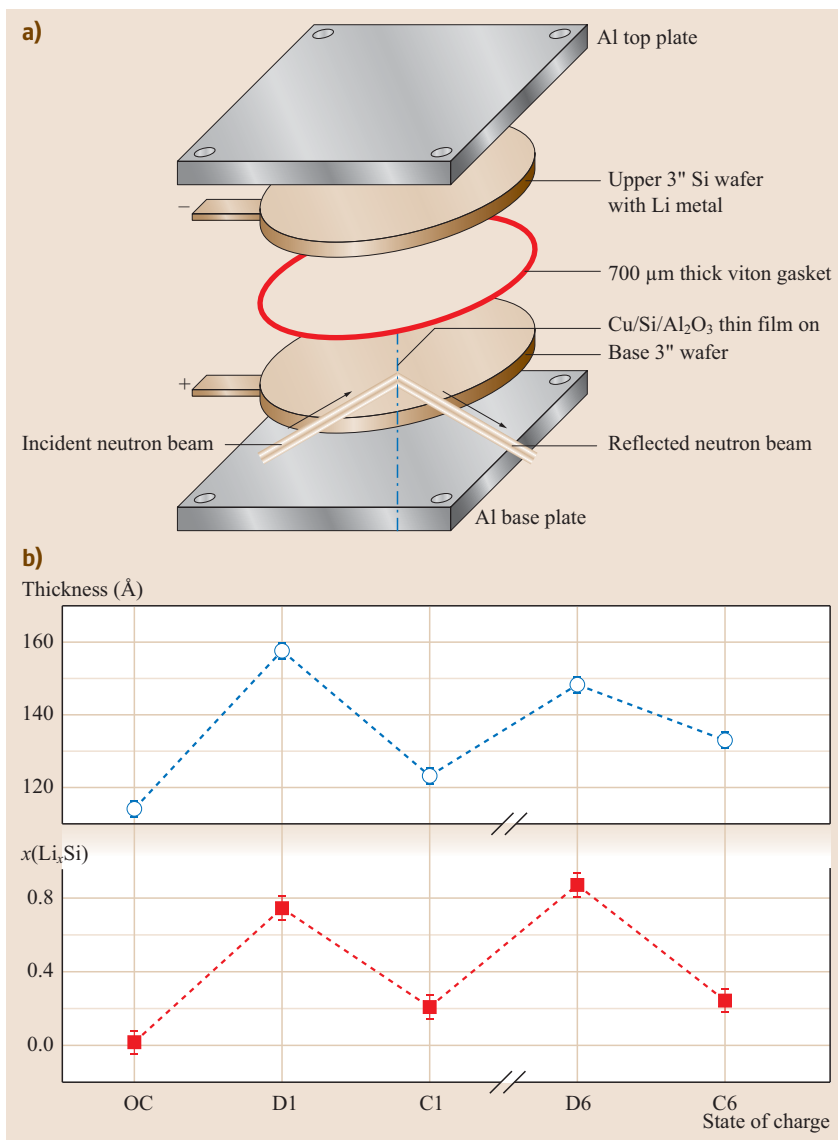


**Fig. 15.31** (a) Schematic illustration of a battery configuration used for an in situ neutron reflectivity study. (b) The thickness of an Si electrode and corresponding Li composition at various states of charge (after [15.91])

power. The relative abundances of  $^6\text{Li}$  can be calculated using the normalized counts of these charged particles, as shown in Fig. 15.30b, where Li distributions in cathode ( $\text{LiCoO}_2$ ), solid electrolyte LiPON and Li metal anode are clearly resolved [15.91].

Another neutron technique variation is its reflectivity on surfaces of different density. While the diffraction is only sensitive to ordered crystalline structures, *neutron reflectivity* sheds rare light on the amorphous phases such as interphase layers on top of bulk electrodes. This high-resolution tool can probe structure and composition with subangstrom accuracy. Typically a monochromatic neutron is directed onto target at a certain angle, and the intensity of the reflecting beam

is recorded as the function of the density of isotopes at varying lengths, as Fig. 15.31 shows for a Si-based anode half cell. The atomic dependence established serves as a compositional profile for the interphase, and the dynamic mapping of various interphase layers during charge–discharge provides valuable insight into how interphase thickness changes with the electrochemical states of the batteries. In a recent neutron reflectometry study by Owejan et al. the progressive growth of SEI thickness was monitored from 4.0–4.5 to 8.9 nm as a potentiostatic hold was placed on the studied electrode [15.92].

The subangstrom sensitivity of neutron reflectivity proves to be a *double-edged sword*. It could pro-



vide well-resolved information about the targets investigated, but it also imposes stringent, sometimes prohibitive, restrictions on the roughness of the target surface, which could be extremely difficult to satisfy. This latter feature severely limits its application for both materials and environments close to real-life devices. Seeking a technique of both high resolution and low intolerance toward surface roughness, or at least finding a balance in between, remains a challenge for neutron spectroscopists and battery and material scientists.

Other potentially useful neutron tools also include *small angle neutron scattering* and *neutron imaging*. The former is useful in measuring the nanoscale structure of grains and how they behave under the stress induced by lithiation, while the latter provides direct visualization of *hot spots* and nonuniformity in  $\text{Li}^+$ -distribution in various electrode materials. Both techniques were summarized in a recent rather comprehensive review by Wang et al. [15.91]. Their application in Li-ion battery fields are just at the budding stage.

## 15.3 Evaluation at the Cell–Battery Level

After the Li-ion anode and cathode materials, separator and the compatible electrolyte are evaluated as discussed in Sect. 15.2, and these components need to be evaluated as a complete electrochemical system at a cell or a battery level for a comprehensive assessment of the performance, life and safety. A cell, which is made of anode, cathode, separator and electrolyte, is a system and needs to function well together as a cell or a battery.

### 15.3.1 Cell Configurations

A cell can be made into a coin cell, pouch cell, prismatic, bobbin or spirally wound cell. For a practical cell, the electrode, either anode or cathode, is typically made by coating a slurry, which is made by blending together a mixture of electrode active material, conductive diluents and binder, which is dissolved in a solvent or solvent mixtures, on both sides of a current collector, copper for anode and aluminum for cathode. Figure 15.32 shows a wound cell assembly with positive electrode, negative electrode and separator, double-side coated porous electrodes, and high surface area particles with small primary particles.

Coin cells [15.93] are also a commonly used testing vehicle for battery materials researchers. These cells can easily be assembled in Argon-filled dry boxes and in dry rooms with simple crimping tools. A test using coin cells will provide information on initial capacity and voltage profile of active anode or cathode materials using half-cell configurations. The electrode-electrolyte stability can also be studied using coin cells with half-cell and full-cell configurations.

Pouch cells are also used for researchers or battery developers for testing battery materials with larger size electrodes. The pouch cells can mimic a practical cell better than coin cells and uncover problems that are hidden in the coin cells such as gas evolution during cycling. A further advantage of using this configuration

is that a reference electrode such as Li can easily be incorporated into the cell for the study of electrochemical behavior of both electrodes at the same time [15.94].

The power capability, or the ability to charge and discharge effectively at different rates, is best evaluated in a range of test cells. The cell resistance determines how much energy is lost to heat rather than electricity ( $I^2R$  losses). Accordingly, the power performance varies greatly with how the electrodes are fabricated, the thickness of the electrode, and how the cell is packaged, in addition to the inherent materials' ionic and electronic conductivities, its morphology and the contacts' resistance within the electrodes and between the electrodes and the cell.

### 15.3.2 Performance Characteristics

The evaluation of Li-ion battery materials at the cell level is necessary for assessing the viability of an electrochemical pair for practical use. Well fabricated electrodes assembled in industrial packaged cells such as 18650 cylindrical cells as well as prismatic cells will be ideal for full assessment. At the cell level, the following important data can be obtained:

1. Discharge capacity and voltage profile
2. Discharge capacity at different rates
3. Charge (capacity) retention and recovery
4. Cycle life (endurance in cycles)
5. Internal resistance
6. Safety.

There are international standards published by the International Electrotechnical Commission (IEC) that *define a minimum required level of performance and standardized methodology by which testing is performed and the results of this testing reported to the users* [15.95]. IEC 61960 is an international standard for *secondary cells and batteries containing alkaline or other nonacid electrolytes – secondary Li cells and bat-*

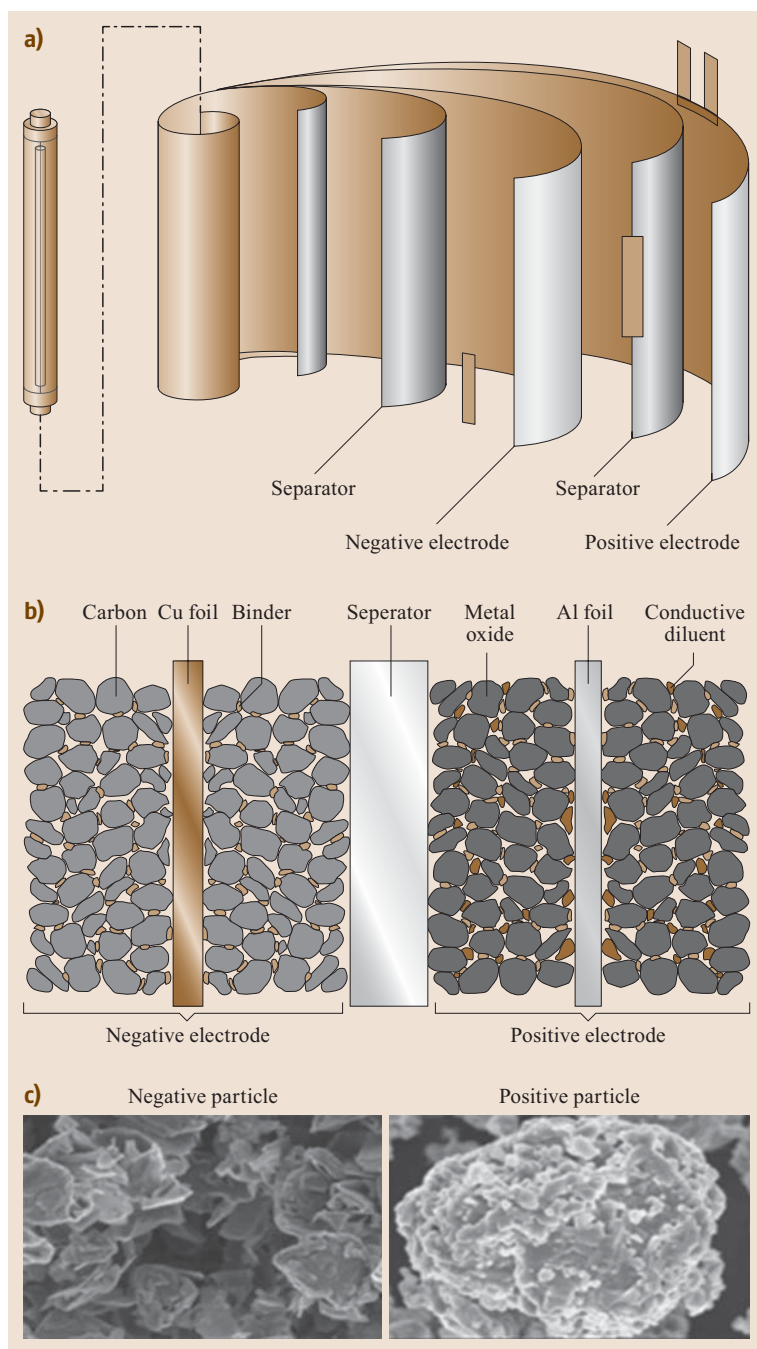


**Fig. 15.32** (a) Wound cell assembly with positive electrode, negative electrode and separator. (b) Double-side coated porous electrodes. (c) High surface area particles with small primary particles (courtesy Saft batteries)

series for portable applications. The standardized tests can also be adopted by researchers for evaluating cells.

The terms and definition used in the standard are also commonly adopted in the electrochemical materials and battery research community. The *rated capacity* is a quantity of electricity  $C_5$  or  $C$  in Ah declared by the battery manufacturer that a single cell or battery

can deliver during a 5 h period when charged, stored and discharged at a constant current of  $0.2 I_t$  A (ampere) down to a specified end-of-discharge voltage in an ambient temperature of  $20^\circ\text{C} \pm 5^\circ\text{C}$ , where  $I_t$  A =  $C$  Ah/1 h. The charge or discharge current are expressed as a multiple of  $I_t$  A. A rate of  $1 I_t$  is equivalent to  $1C$  rate, which means the capacity will be discharged in 1 h

**Table 15.1** Theoretical and actual energy densities of selected Li-ion chemistries (after [15.96])

Chemistry	Size	Theoretical (Wh/l)	Actual (Wh/l)	(%)	Theoretical (Wh/kg)	Actual (Wh/kg)	(%)
LiFePO <sub>4</sub>	54 208	1980	292	14.8	587	156	26.6
LiFePO <sub>4</sub>	16 650	1980	223	11.3	587	113	19.3
LiMn <sub>2</sub> O <sub>4</sub>	26 700	2060	296	14.4	500	109	21.8
LiCoO <sub>2</sub>	18 650	2950	570	19.3	1000	250	25.0
Si-LiMO <sub>2</sub> Panasonic	18 650	2950	919	31.2	1000	252	25.2

The theoretical values in the table assume only the active components, and no volume or weight for Li beside that in the cathode

at this rate. A rate of  $0.2 I_t$  A is often called  $0.2 C$  rate and  $5 I_t$  A is equivalent to  $5 C$  rate.

*Dahn and Ehrlich* [15.97] have recently provided an excellent overview of the state-of-the-art Li-ion batteries that were available before 2010. New Li-ion batteries of different variations of anode and cathode and configuration have appeared since then. The information regarding these batteries can be found at their websites. The most important characteristics of a Li-ion cell or battery are energy density, power capability, cycle life and storage life, and safety. The related methods for understanding these characteristics are discussed below.

### 15.3.3 Energy Density

The energy density of an electrochemical pair at the materials level that has been discussed in Sect. 15.2.1 is often called the theoretical energy density of the cell. The energy density of an electrochemical pair at the cell level varies with the tap density of anode and cathode materials, contents of conductive diluents, contents of binder, porosity of the electrode, and tightness of the winding. The inclusion of safety devices in the cell will also affect the energy density of the cell. At the battery level, a battery management system will be installed to ensure the proper operation of the cells or batteries. The energy density values at the cell and the battery levels can be found at the battery manufacturers' websites. Table 15.1 shows the difference between theoretical and actual energy densities of some selected Li-ion chemistries [15.96]. The actual energy density is only a fraction of the theoretical energy density. Further improvement in actual energy density is possible through improvements in materials morphology, processes for fabricating electrodes with reduced nonactive materials contents, and packaging methods.

### 15.3.4 Power Capability

The power performance is one of the very important performance characteristics of batteries for a number of applications requiring high power including power tools and hybrid electric vehicles. The power performance or rate capability of a cell is determined in part

by the internal resistance in the cell as the power is the product of the cell voltage and cell current, which is determined by the cell voltage divided by the cell resistance. In short, the power that can be delivered by a cell is proportional to the square of the voltage and inversely proportional to the cell resistance. The cell resistance is mostly affected by the ability of the electrode materials to conduct electrons and ions. Electrolytes also affect the cells' resistance especially at low temperatures as the charge transfer resistance at the graphite anode–electrolyte interface substantially increases at temperatures below  $-20^\circ\text{C}$  [15.94] and their viscosities increase. However, the cell resistance can also be reduced by engineering efforts including the incorporation of conductive diluents, optimization of electrode porosity, reduction of contact resistance between electrode and current collector and between current collector and cell terminals and reduction of electrode thickness.

The cell resistance  $R_{\text{cell}}$  is the sum of several resistances existing in the cell as expressed in equation

$$R_{\text{cell}} = R_e + R_{\text{electrolyte}} + R_{\text{SEI}} + R_{\text{ct}}, \quad (15.23)$$

where  $R_e$  represents all of the contact resistance within the electrodes, electrode–current collector contact resistance and current collector–cell terminals contact resistance;  $R_{\text{electrolyte}}$  is the resistance of the electrolyte;  $R_{\text{SEI}}$  is the resistance of the SEI layers on the electrodes; and  $R_{\text{ct}}$  represents the charge transfer resistance at the electrodes and electrolyte interfaces.

The cell internal resistance can be measured using DC and AC methods. The international standard IEC 61960 [15.95] for secondary Li cells and batteries for portable electronics and IEC 62620 [15.98] for large format secondary Li cells and batteries for industrial applications have described the methods for measuring both resistances in detail. These methods are discussed later.

#### Internal DC Resistance

The internal DC resistance can be determined by discharging a cell, when the cell is at the 50% SOC, at a specified current  $I_1$  for a period of time, e.g., 30 s, and measuring the voltage,  $U_1$ , at the end of 30 s and then

immediately increasing the current to a higher specified  $I_2$  and continued discharge for 5 s and recording the voltage  $U_2$  at the end of 5 s. The internal DC resistance  $R_{DC}$  is calculated using

$$R_{DC} = \frac{U_1 - U_2}{I_2 - I_1} (\Omega), \quad (15.24)$$

where  $I_1$  and  $I_2$  are the constant discharge currents, and  $U_1$  and  $U_2$  are the appropriate voltages measured under load.

For hybrid vehicle applications, the hybrid pulse power characteristics (HPPC) test described in PNGV battery test manual [15.99] is used to determine the pulse discharge or charge resistance or the power capability of cells or batteries. The same relationship as shown in (15.24) is used to determine the pulse discharge resistance or power. But the discharge–charge current and discharge–charge time period are different from that specified in IEC 61960 and 62620.

**HPPC Test.** The HPPC Test is intended to determine the power capability of a cell or battery at the end of 18 s discharge, as a function of depth of discharge, or the power capability of a cell or battery at the end of a 2 s regeneration as a function of the state of charge (SOC) of the cell or battery for hybrid vehicle applications. For different operational modes, the discharge and charge time periods can be different. The test current selected is 5C rate or 25% of the maximum of the manufacturer's absolute maximum allowable pulse discharge or charge current. The discharge power at the specific SOC can be determined using the voltage measured at the end of the 18 s discharge and the discharge current. Figure 15.33 shows one example of the pulse power capability versus depth of discharge of a battery at power assist mode and dual mode. The details of the test procedures can be found in the PNGV battery test manual [15.99].

Pulse discharge resistance and pulse charge resistance, or area specific impedance (ASI) in  $\Omega \text{ cm}^2$ , can be obtained using the HPPC test [15.99, 100]. The cell is charged to 100% SOC and allowed to rest for 1 h. Subsequently, the cell is discharged 10% and allowed to rest for 1 h. Next, a 5C rate discharge pulse is applied for 10 s. After the pulse, the cell is allowed to rest for 40 s, after which a 10 s charge pulse is applied. After the 10 s charge pulse, the cell is discharged to the next state of charge of 80%. After the cell reaches 90% SOC, it is allowed to rest for 1 h. Subsequently, the discharge and charge pulses are applied again and the cell is then taken to 70% SOC. This continues until the cell can no longer complete the discharge pulse or the cell reaches 0% SOC. The voltages at the end of the 1 h rest and at the end of the discharge pulse are used to calculate the

ASI for discharge, and the voltages at the end of the 40 s rest and at the end of the charge pulse are used to calculate the ASI for charge.

### Internal AC Resistance and AC Impedance

The AC resistance is determined by measuring the alternating root mean squared (RMS) voltage  $U_a$ , while applying an alternating rms current,  $I_a$ , at the frequency of  $1.0 \pm 0.1 \text{ kHz}$ , to the battery, for a period of 1–5 s. All voltage measurements should be made at the terminals of the battery independently of the contacts used to carry current. The internal AC resistance  $R_{AC}$  is given by

$$R_{AC} = \frac{U_a}{I_a} (\Omega), \quad (15.25)$$

where  $U_a$  is the alternating rms voltage and  $I_a$  is the alternating rms current.

Instead of determining the AC resistance at a single frequency, EIS can be used as described in Sect. 15.2.2 and Sect. 15.2.4, whereby an electrochemical pair at the cell level is measured over a wide frequency range from  $10^{-3}$  to  $10^6 \text{ Hz}$ .

An impedance measurement of commercial 18 650 LiCoO<sub>2</sub>/graphite based Li-ion cells reveals that the charge-transfer resistance  $R_{ct}$  varied with temperature following an Arrhenius relationship [15.101],

$$\frac{I}{R_{ct}} = A_0 e^{-E_a/RT}, \quad (15.26)$$

where the  $E_a$  is the activation energy, which is about 70 kJ/mol for this case [15.102]. As identified using Li as a reference electrode in three-electrode Li-ion cells with graphite as an anode and either LiFePO<sub>4</sub> or LiCo<sub>0.15</sub>Ni<sub>0.8</sub>Al<sub>0.05</sub>O<sub>2</sub> as a cathode, the activation energy for the charge transfer at the graphite anode is also found to be about 67–68 kJ/mol. This suggests that the Li-ion cell is dominated by the charge transfer process across the graphite–electrolyte interface [15.94].

EIS is also a powerful tool in assessing the dynamic power performance dependence on temperature as well as SOC through the impedance measurement at all operating conditions in a wide frequency range. The different electrochemical processes in a cell can also be observed. The study of VL6P, a commercial 6.5 Ah high power Li-ion cell from Saft – a cylindrical cell optimized for the use in hybrid vehicles – using impedance method was recently reported by Andre et al. [15.103].

EIS can also be used to study the aging mechanisms of LiFePO<sub>4</sub>/graphite [15.104] and Li(Co<sub>0.2</sub>Ni<sub>0.8</sub>)O<sub>2</sub>/graphite [15.105] Li-ion chemistries by monitoring the impedance evolution over the cell's cycle life.

Srinivasan et al. [15.106] and Srinivasan [15.107] demonstrated the existence of an intrinsic relationship

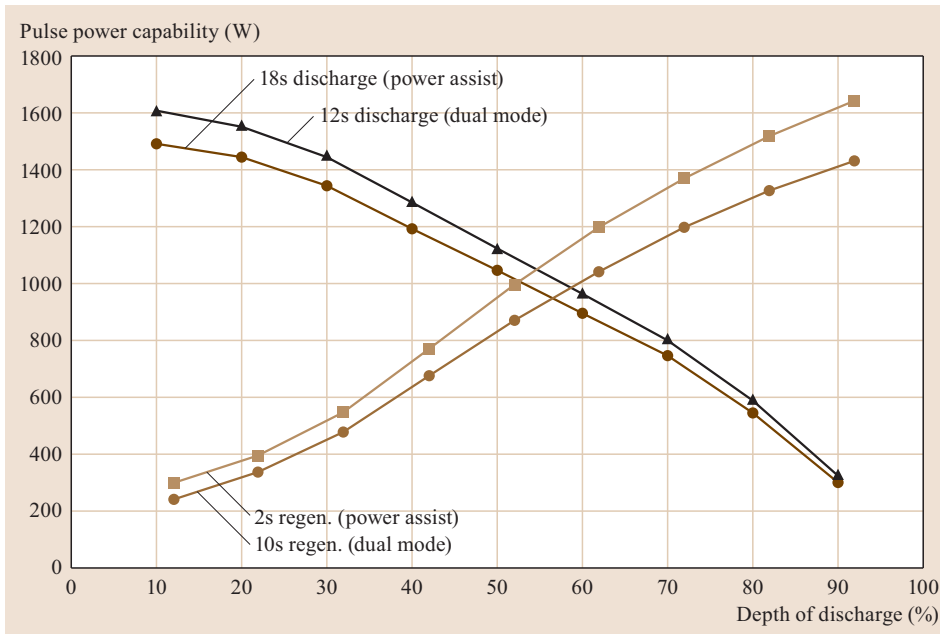


**Fig. 15.33** Pulse power capability versus depth of discharge

between a cell's internal temperature and a readily measurable electrical parameter, the phase angle between an applied sinusoidal current and the resulting voltage in three different Li-ion cells, a 53 Ah GS-Yuasa LSE50-002, a 2.3 Ah ANR26650 and a 4.4 Ah Boston Power Swing 4400. This is an interesting application of the EIS method in assessing the thermal behavior inside the Li-ion cells.

### 15.3.5 Cycle Life and Storage Life (or Calendar Life)

The Li-ion cells lose their capacities during cycling and storage. The cycle life is important for space, automotive and grid energy storage applications, which require services of over 10 years and often involve heavy duty cycling. The storage life is especially important for standby applications including standby power for telecom operations.

The cycling life of a cell or battery is given by the total number of discharge–charge cycles, in which the cell is discharged to the specified end-of-discharge voltage and charged to the specified voltage, performed to reach 60% of the initial capacity at the 0.2  $I_L$  A (or 0.2 C) rate at  $25 \pm 5^\circ\text{C}$  based on the IEC 61690 for secondary Li cells and batteries for portable applications and IEC 62620 for large format secondary Li cells and batteries for use in industrial applications. For a 500 cycling life test at a rate of 0.2 C, the test time will be 5000 h, which equals over 208 d. Higher rates can be used for shorter term tests. The storage life test calls for

a cell or battery to sustain a minimum of 75% of capacity after 6 months of storage at a constant voltage corresponding to 100% SOC at a temperature specified by the manufacturer.

For different applications such as hybrid electric vehicles, the cycling test profile and the required cycle life could vary and would demand a much longer real life testing. Therefore, the understanding of the capacity fading rate and fading mechanism are the keys in predicting and improving life of the batteries. The life prediction and aging mechanisms are mostly investigated on mature battery chemistries with consistent products available for specific applications in mind.

Electrochemical techniques such as galvanostatic charge–discharge at different rates, AC impedance, and HPPC measurements have been used to characterize the source of capacity fading. The use of a Li reference electrode allows identification of whether the fading is coming from the cathode or anode.

In characterizing the cells made of graphite/ $\text{LiCo}_{0.15}\text{Ni}_{0.8}\text{Al}_{0.05}\text{O}_2$ , Zhang et al. [15.108], using a Li reference electrode, identified that the capacity fade during cycling is primarily caused by the positive electrode as shown in the increase in impedance at the cathode, where discharge capacity may be limited by a decrease in active Li intercalation sites in the oxide particles. Different from graphite/ $\text{LiCo}_{0.15}\text{Ni}_{0.8}\text{Al}_{0.05}\text{O}_2$  batteries, the graphite/ $\text{LiFePO}_4$  batteries as reported by Liu et al. [15.104] do not experience appreciable resistance increase under a variety of cycling conditions.



The loss of active Li results from the repairing of the SEI at the graphite anode [15.104].

### High Precision Coulometry

Smith et al. [15.109] of Jeffrey Dahn's group in Dalhousie University, Canada, recently have suggested that high precision coulometry (HPC) can indicate the relative cycle and calendar life of cells by measuring the extent of parasitic reactions in coulombic efficiency (CE) in only a few weeks of testing. Parasitic reaction rate,  $k$  ( $\text{h}^{-1}$ ), for  $\text{LiCoO}_2$ ,  $\text{LiFePO}_4$ , and  $\text{LiMn}_2\text{O}_4$ /graphite Li-ion cells at different temperatures can be determined from CE and the time of one cycle using the relationship

$$1.0000 - \text{CE} = k \quad (\text{time of one cycle}) . \quad (15.27)$$

High precision coulombic efficiency measurements can detect problems occurring in half cells that do not lead to capacity loss, but would in full cells, and can measure the impact of electrolyte additives and electrode coatings [15.110]. This is a powerful tool for researchers who do not have access to packaged cells.

### 15.3.6 Safety

Safety has been a concern for the users of Li-ion batteries as a number of incidents of fire have been reported in the news. Safety is also an important area in research and development of Li-ion batteries because it is intimately related to the electrode and electrolyte materials selected and their chemistries under various electrical, electrochemical, thermal and heat conditions.

Commercial Li-ion cells and batteries have to pass a number of safety tests under the conditions of *intended use* and *reasonably foreseeable misuse* as described in IEC 62133 [15.111]. The tests include 1) continuous low-rate charging under *intended use* and 2) external short circuit, thermal abuse, crushing of cells, overcharge, forced discharge, and protection of cells under high rate charging current under the *reasonably foreseeable misuse* conditions. The test conditions and procedures are detailed in the safety standards such as IEC 62133 [15.111], an emerging unified international safety standard at a product level for rechargeable batteries, and UL 1642 [15.112], a standard for safety developed by Underwriters Laboratories Inc. (UL) for Li batteries. IEC 62133 (secondary cells and batteries containing alkaline or other nonacid electrolytes) – general guidelines, is expected to replace UL 1642 by 2012. UL's battery testing laboratories are accredited to do the testing and certification to IEC 62133.

The criteria for passing these tests are that the cells shall not cause fire or explosion under the above test

conditions. The commercial Li-ion cells such as VL cells from Saft batteries also feature various redundant safety features (electronic protection circuit, built-in circuit breaker in case of faulty chargers, safety valve, shut down separator), which makes them ideal for demanding applications (military, medical, etc.).

The evaluation of safety aspects of a cell or battery starts by assessing the electrochemical stability of the battery components including electrode materials and electrolytes as discussed in Sect. 15.2.1 and 15.2.2. The ability of the cell or battery to withstand the electrical misuse including short circuit, overcharge, overdischarge, and high rate charging is largely determined by the chemistry and electronic structure of cathode materials. For example, Li can be completely removed from the fully lithiated  $\text{LiFePO}_4$  of olivine structure at a fully discharged state and leave a stable delithiated phase  $\text{FePO}_4$  at a fully charged state [15.113] resulting in a much safer  $\text{LiFePO}_4$ /graphite Li-ion cell. A layer structured  $\text{LiCoO}_2$  would not be able to remove Li completely before the oxygen is removed from the structure and reacted with the flammable electrolyte made of carbonate-based solvents and the Al current collector, causing a thermal runaway.

Physical damage such as crushing, which is similar to a short circuit in the cell, will cause substantial heat generation. Under thermal abuse, the cell or battery is exposed to accelerated reactions between electrode materials and the electrolyte, which will also cause heat generation. Therefore, thermal characterization of Li-ion cells under various electrical conditions is the main characterization tool for the study of the safety of Li-ion at the cells or batteries level.

Thermal characterization techniques including the following are used to assess the safety level of the battery materials and cells:

1. Differential scanning calorimetry (DSC). This technique allows the measure of the thermal response of individual and selected combinations of cell components over a broad temperature range by scanning temperature at a fixed rate. MacNeil et al. [15.115] used DSC to compare the thermal stability of seven different charged cathodes in 1 M  $\text{LiPF}_6$  EC/DEC electrolyte. It was concluded that the cathode materials can be ranked from most safe to least safe in the following order:  $\text{LiFePO}_4$ ,  $\text{LiNi}_{3/8}\text{Co}_{1/4}\text{Mn}_{3/8}\text{O}_2$ ,  $\text{Li}_{1-x}\text{Mn}_{2-x}\text{O}_4$ ,  $\text{LiCoO}_2$ ,  $\text{LiNi}_{0.7}\text{Co}_{0.2}\text{Ti}_{0.05}\text{Mg}_{0.05}\text{O}_2$ ,  $\text{LiNi}_{0.8}\text{Co}_{0.2}\text{O}_2$  and  $\text{LiNiO}_2$ .
2. Accelerated-rate calorimetry (ARC). This technique applies to full cells as well as cell components under adiabatic conditions. Under this condition,

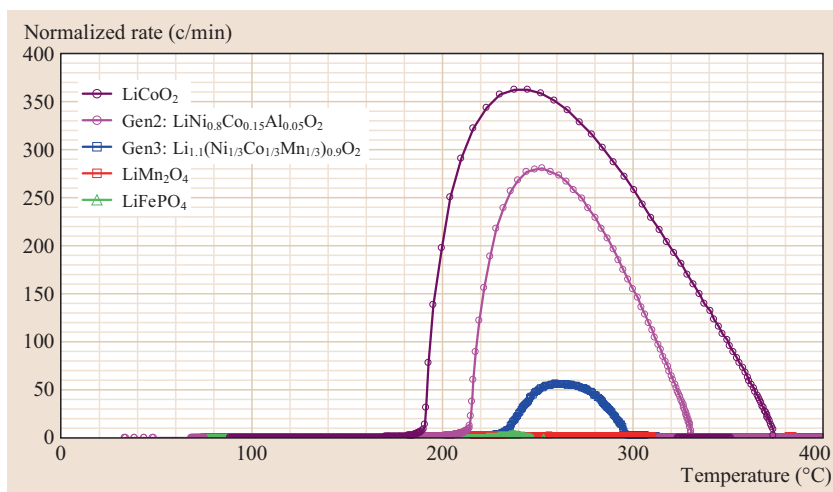


**Fig. 15.34** Self-heating rate of 18 650 full cells of different cathodes including  $\text{LiCoO}_2$ ,  $\text{LiNi}_{0.8}\text{Co}_{0.15}\text{Al}_{0.05}\text{O}_2$ ,  $\text{Li}_{1.1}(\text{Ni}_{1/3}\text{Co}_{1/3}\text{Mn}_{1/3})_{0.9}\text{O}_2$ ,  $\text{LiMn}_2\text{O}_4$  and  $\text{LiFePO}_4$  measured by ARC. Improved cathode stability results in higher thermal runaway temperature (increased stability) and reduced peak heating rate (after [15.114])

the cell heating rate is strictly a function of the intrinsic heat generating reactions in the cell and the thermal heat capacitance of the cell components [15.114]. Figure 15.34 shows the self-heating rate of 18 650 full cells of different cathodes measured by ARC. Improved cathode stability results in higher thermal runaway temperature and reduced peak heating rate [15.116].

3. **Thermal Ramp Test.** The thermal stability of cells can be studied by linear programmed heating to cell failure. In this test, the cells are heated at a programmed heating rate,  $5^\circ\text{C}/\text{min}$  is typical, from

room temperature to  $250^\circ\text{C}$  or higher, at which temperature the cell fails by initiating a thermal runaway. The flammability of the vent gases and electrolyte solvent vapor can be determined by placing spark ignition sources in critical locations around the cell fixture [15.114].

A series of articles relating to Li-ion battery safety published in 2012 *Electrochemical Society Interface Magazine* [15.117] provide an excellent overview of the Li-ion battery safety issues, which included how electrolytes influence battery safety [15.118].

## 15.4 Beyond Li-Ion

The maximum energy density that can be expected for Li-ion batteries is about  $275\text{ kWh/kg}$ , which is limited by the stoichiometric  $\text{Li}^+$  ion amount of the intercalation electrode materials. In order to meet the emerging energy capacity needs for batteries, alternative chemistries are being proposed. As suggested by the name, the batteries beyond Li-ion do not use  $\text{Li}^+$  ion intercalation compounds as the electrode material, instead, these types of batteries are based on the alternative Li-based redox couples with significantly higher specific capacity than Li-ion batteries. Typical examples of the batteries beyond Li-ion are lithium-sulfur (Li-S) battery and Li-air battery (or  $\text{Li}-\text{O}_2$  battery).

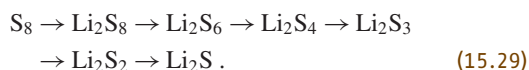
### 15.4.1 Li-S Battery

Lithium-sulfur (Li-S) batteries offer a theoretical specific capacity of  $1675\text{ Ah/kg}$  and a theoretical specific energy of  $2500\text{ Wh/kg}$  (or  $2800\text{ Wh/l}$ ) based on the complete reduction from elemental sulfur to lithium

sulfide by



The high theoretical specific capacity and low cost of sulfur makes Li-S batteries attractive. In nature, sulfur exists mainly in the form of ring-structural cycloocta-sulfur ( $\text{S}_8$ ), thus the reduction of sulfur in a Li-S cell is a multistage process through a series of lithium polysulfide ( $\text{PS}$ ,  $\text{Li}_2\text{S}_x$ ) intermediates, as [15.118]



These multistage reductions are reflected in the voltage curve of the first discharge, and can be divided into such four general stages as:

1. A solid-to-liquid phase reaction from sulfur ( $\text{S}_8$ ) to dissolved  $\text{Li}_2\text{S}_8$ , which corresponds to an upper voltage plateau at  $\approx 2.3\text{ V}$

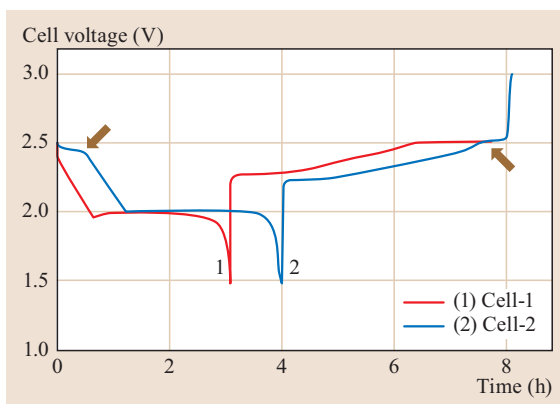


**Fig. 15.35** Typical discharge and charge voltage curves of Li-S cells at constant current rate. (1) Baseline cell, and (2) cell with the suppression of redox shuttle reaction by  $\text{LiNO}_3$  in the electrolyte

2. A single liquid phase reaction from high-order  $\text{Li}_2\text{S}_8$  to low-order  $\text{Li}_2\text{S}_4$ , which corresponds to a linear voltage decline
3. A liquid-to-solid phase reaction from the soluble  $\text{Li}_2\text{S}_4$  to insoluble  $\text{Li}_2\text{S}_2$  or  $\text{Li}_2\text{S}$ , which corresponds to a lower voltage plateau at  $\approx 2\text{ V}$  and contributes to the major capacity of a Li-S cell
4. A solid-to-solid phase reaction from insoluble  $\text{Li}_2\text{S}_2$  to insoluble  $\text{Li}_2\text{S}$ , which corresponds to a steep voltage decline.

Since PS intermediates are soluble in nonaqueous electrolytes and their solubility increases with the length of PS anion chain (i.e.,  $x$  value in  $\text{Li}_2\text{S}_x$ ), the Li-S cell is indeed a liquid electrochemical system. In discharge, sulfur is first reduced into highly soluble  $\text{Li}_2\text{S}_8$ , which dissolves into the electrolyte and serves as the *liquid cathode*. However, the dissolution of PS in liquid electrolyte causes many problems, which include:

1. The dissolution of PS results in a loss in the sulfur active material
2. PS diffuses to the Li anode and reacts with metal Li, which corrodes the Li anode and increases the cell's self-discharge
3. PS is electrochemically reduced on the surface of the Li anode, which reduces charging efficiency
4. PS in electrolyte solution might disproportionate into insoluble species, which precipitates out of the electrolyte to become inactive sulfur.

On the other hand, the dissolution of PS is essential for the kinetics of the cell's reaction. Since sulfur and its reduction intermediates and products are neither

electronically conductive nor ionically conductive, the dissolution transfers PS into solution so that the cell's reaction can easily take place on the interface between carbon and electrolyte solution.

While charging, the dissolved PS can be chemically (i.e., directly reacting with metal Li) and electrochemically reduced on the Li anode in addition to being electrochemically oxidized to higher order PS on the cathode. This phenomenon, called a *redox shuttle effect*, significantly affects the charging efficiency and the cell's performance. Figure 15.35 shows typical discharge and charge voltage curves of Li-S cells without and with suppression of redox shuttle by using a  $\text{LiNO}_3$ -contained electrolyte to protect the Li anode (Cell-1 and Cell-2, respectively). Cell-1 can only be charged to 2.5 V, at which point the cell's voltage remains unchanged until the end of the charging process, showing a strong redox shuttle effect. As a result, the following discharge does not show the upper voltage plateau. Cell-2 passes the upper voltage plateau at 2.5 V and reaches the charging cut-off voltage, showing effective suppression of the redox shuttle effect, so that the following discharge shows an upper voltage plateau.

Due to the dissolution of PS and its resulting redox shuttle effect, the theoretical specific capacity and energy density of Li-S cells are not easily obtained, and most of the known problems with Li-S cells are related to the dissolution of PS. Therefore, effective evaluations of Li-S cells are focused on PS-related effects, which include:

1. Cycle life, which reflects the overall effect of the PS dissolution and its resulting effects, including the loss of sulfur active material, Li corrosion, and chemical stability of electrolyte solvents against PS intermediates and metal Li.
2. Charging efficiency, which is a good measure for the redox shuttle reactions of PS in charging process. The redox shuttle reactions not only involve chemical reaction between PS and metal Li but also include electrochemical reduction of PS on the Li surface. High charging efficiency may result from either the suppression of PS diffusion out of the cathode or the protection of Li anode.
3. Self-discharge, which relates to the chemical reactions between the dissolved PS and Li anode, and to the disproportionation of PS in electrolyte solution, which occurs spontaneously during storage.
4. Safety. Direct chemical reactions between the dissolved PS and the Li anode at elevated temperatures is a major source affecting the safety of Li-S batteries, therefore hot-oven storage test is a good measurement for the safety of Li-S batteries.

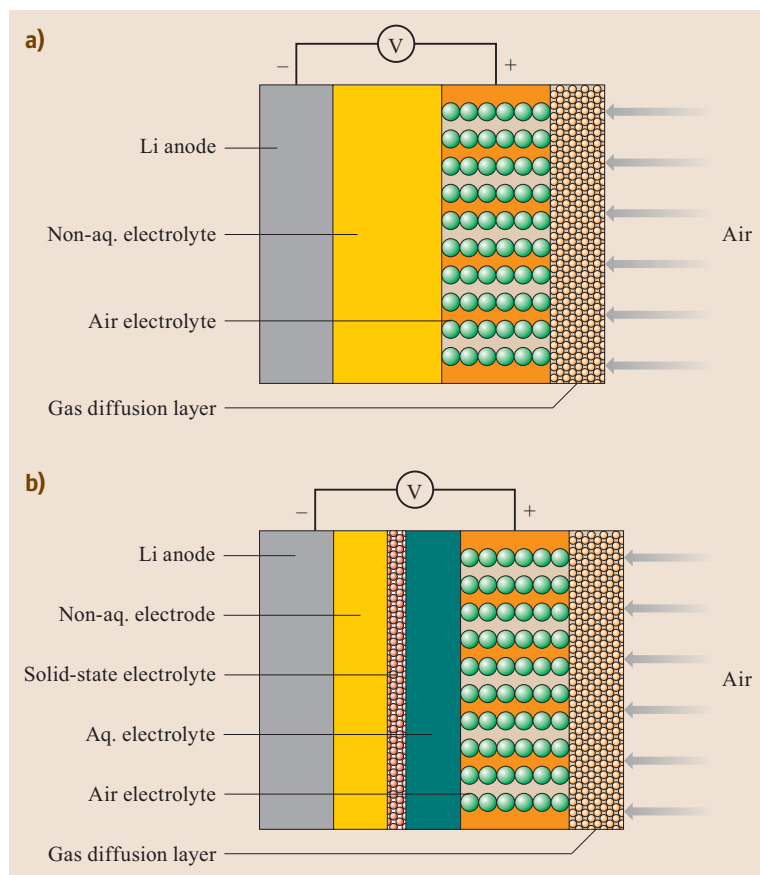


**Fig. 15.36a,b** Schematic structure of Li-air cells. **(a)** Nonaqueous electrolyte, **(b)** hybrid electrolytes

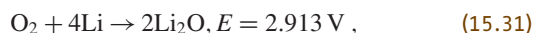
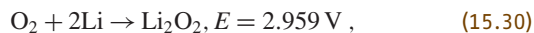
5. Low-temperature performance. Dissolution of PS increases the viscosity of the electrolyte solution, which mostly affects the power capability and low temperature performance of Li-S cells.

### 15.4.2 Li-Air Battery

Li-air cells are a class of metal-air batteries. According to the atomic weight of metal Li, the Li-air cell has a theoretical specific capacity of 3862 Ah/kg and a theoretical energy density of 11 425 Wh/kg, which are among the highest values in the known metal-air chemistries. In general, the Li-air cell is composed of a gas diffusion layer (GDL), an air electrode, a separator/electrolyte, and a Li anode. Since metal Li reacts with moisture and CO<sub>2</sub> in the air, the Li anode needs a nonaqueous electrolyte. The Li-air cell can be configured in two electrolyte protocols, i.e., nonaqueous electrolyte system and hybrid nonaqueous-aqueous electrolyte system, as shown in Fig. 15.36.

In the nonaqueous electrolyte Li-air cell, the GDL should be able to isolate moisture and CO<sub>2</sub> from the cell in addition to distributing O<sub>2</sub> evenly into the air

electrode and preventing the evaporation of electrolyte solvents out of the cell. The air electrode is a porous carbon sheet without or with the loading of a oxygen reduction reaction (ORR) catalyst. In many cases, the ORR is a mixed process of a two-electron reduction and a four-electron reduction, as described by



which depends on the ORR catalyst, electrolyte solvents, and discharge conditions. The discharge products of Li-air cells are often a mixture of Li<sub>2</sub>O<sub>2</sub> and Li<sub>2</sub>O. Since both Li<sub>2</sub>O<sub>2</sub> and Li<sub>2</sub>O are insoluble in nonaqueous electrolytes, they deposit and accumulate on the surface of air electrodes, which consequently clog the access of oxygen into catalytic sites of catalyst and halt the cell's operation. Therefore, the specific capacity and energy density of a Li-air cell are expressed in reference to the mass of carbon. Since the ORR occurs on the *solid-liquid* interface between the catalytic sites and dissolved oxygen, an optimized *solid-liquid* two-phase reaction zone is required for high capacity and

power [15.119]. A general rule is that high capacity requires a large reaction area and high power requires a thin liquid electrolyte film on the catalyst.

For primary Li–air cells, there are no special requirements for ORR catalyst and electrolyte solvents. Especially for low power applications, the catalytic activity of carbon itself is high enough to meet ORR without need of an additional catalyst. For rechargeable Li–air cells, however, there are critical requirements for both the ORR catalyst and electrolyte solvents. First, the reversibility requires a two-electron ORR catalyst because the four-electron ORR product  $\text{Li}_2\text{O}$  cannot be electrochemically oxidized to  $\text{O}_2$  once it is formed. Second, the electrolyte solvents are required to be chemically stable against the ORR and oxygen evolution reaction (OER) intermediates. In nonaqueous electrolytes, the ORR and OER involve various oxygen radical anions as the intermediate. These intermediates are highly reactive, which will decompose many organic solvents. For example, the main ORR products in carbonate-based electrolytes are the decomposition products of carbonate solvents, instead of the  $\text{Li}_2\text{O}_2$  or  $\text{Li}_2\text{O}$  as predicted by (15.30) and (15.31) [15.120]. Therefore, evaluations on the nonaqueous electrolyte rechargeable Li–air cells are mainly focused on the ORR catalyst and electrolyte solvent, including the catalytic activity and selectivity of the two-electron ORR for catalyst and the chemical stability against oxygen radical anions for the electrolyte solvent. Other evaluations include: (1) diffusivity of gaseous oxygen and the efficiency for oxygen separation and blockage of  $\text{CO}_2$ , moisture, and electrolyte solvent loss for GDL, (2) porosity of carbon material and carbon electrode for the air cathode, and (3) Li stability and cycling efficiency for the electrolyte.

In a hybrid electrolyte Li–air cell, there are two types of electrolytes: one is a nonaqueous electrolyte for the Li anode and the other is an aqueous electrolyte for the air cathode, which are physically isolated by a solid-state  $\text{Li}^+$ -ion conductive electrolyte film (Fig. 15.34b). Because of the change in the electrolyte system, the

overall cell reaction of Li–air cells changes to



in which water becomes a part of the cell's reaction and the ORR is dominated by the four-electron process. More importantly, the ORR product, LiOH, dissociates and dissolves into the aqueous electrolyte, which makes the ORR/OER conversion reversible. In such cells, the solubility and dissolution capacity (relating to the amount of water) of LiOH in the aqueous electrolyte are the important factors for determination of the cell's capacity, and an optimized *solid–liquid–gas* (i. e., catalyst–electrolyte–oxygen) three-phase reaction zone increases the cell's power. In addition to those mentioned in the nonaqueous Li–air cells, the following evaluations are applicable to the hybrid electrolyte Li–air cells:

1. Solid-state electrolyte film: Ionic conductivity, porosity (or called film density), chemical stability against Li metal and two liquid electrolytes, leakage of liquid electrolyte across the film, and mechanical strength for withstanding the cell's stress. Among those, chemical reduction of the electrolyte materials by Li metal and cationic exchange between  $\text{Li}^+$  ions in electrolyte film and protons in water are known to be the major challenges for many NASICON (sodium super ionic conductor)-based  $\text{Li}^+$  ionic conducting glass ceramics such as LATP ( $\text{Li}_{1+x+y}\text{Al}_x\text{Ti}_{2-x}\text{Si}_y\text{P}_{3-y}\text{O}_{12}$ ) glass.
2. Aqueous electrolyte: Ionic conductivity, viscosity, wettability and distribution on the air electrode, and solubility and dissolution capacity of LiOH.
3. Air electrode: Hydrophobicity for optimized three-phase reaction zone, ORR catalyst for cell's power/polarization, and catalyst's chemical stability against the aqueous electrolyte for cycle life.
4. GDL: For fast diffusion of gaseous oxygen, the GDL is required to be highly porous while avoiding water flooding on the GDL and air electrode.

## 15.5 Conclusions

Electrochemical materials and systems can employ a variety of electrochemical characterization techniques as demonstrated in this chapter on Li-ion batteries, which are not available to nonelectrochemical systems. These techniques, in conjunction with other appropriate characterization methods, result in a powerful suite

of characterization tools that aid in the fundamental understanding and advancement of these technologies. Further advances, especially in developing in situ techniques, will allow for more rapid understanding of the nature of the components, their interactions and system behavior.



## References

- 15.1 P.P. Prossini: Modeling the voltage profile for  $\text{LiFePO}_4$ , J. Electrochem. Soc. **152**(10), A1925–A1929 (2005)
- 15.2 M.S. Whittingham: Electrical energy storage and intercalation chemistry, Science **192**(4244), 1126–1127 (1976)
- 15.3 S. Basu, C. Zeller, P.J. Flanders, C.D. Fuerst, W.D. Johnson, J.E. Fischer: Synthesis and properties of lithium-graphite intercalation compounds, Mater. Sci. Eng. **38**, 275–283 (1979)
- 15.4 R. Yazami, P. Touzani: A reversible graphite-lithium negative electrode for electrochemical generators, J. Power Sources **9**, 365–371 (1983)
- 15.5 S. Basu: assigned to Bell telephone laboratories, Rechargeable battery, US Patent 4 304 825 (1981)
- 15.6 J. Goodenough, K. Mizushima: Electrochemical cell with new fast ion conductors, US Patent 4 302 518 (1981)
- 15.7 T. Nagaura, K. Tozawa: *Progress in Batteries and Solar Cells*, Vol. 9 (JECS, Brunswick 1990) p. 20
- 15.8 A.K. Padhi, K.S. Nanjundaswamy, J.B. Goodenough: Phospho-olivines as positive-electrode materials for rechargeable lithium batteries, J. Electrochem. Soc. **144**, 1188–1194 (1997)
- 15.9 I.A. Courtney, J.R. Dahn: Electrochemical and in situ x-ray diffraction studies of the reaction of lithium with tin oxide composites, J. Electrochem. Soc. **144**, 2045–2052 (1997)
- 15.10 A.S. Andersson, J.O. Thomas: The source of first-cycle capacity loss in  $\text{LiFePO}_4$ , J. Power Sources **97–98**, 498–502 (2001)
- 15.11 C. Delacourt, P. Poizot, J.M. Tarascon: The existence of a temperature-driven solid solution in  $\text{Li}_x\text{FePO}_4$  for 01, Nature Mater. **4**, 254–260 (2005)
- 15.12 D. Aurbach, M.D. Levi, K. Gamulski, B. Markovsky, G. Salitra, E. Levi, U. Heider, L. Heider, R. Oesten: Capacity fading of  $\text{Li}_x\text{Mn}_2\text{O}_4$  spinel electrodes studied by XRD and electroanalytical techniques, J. Power Sources **81**, 472–479 (1999)
- 15.13 J.R. Dahn: Phase diagram of  $\text{Li}_x\text{C}_6$ , Phys. Rev. B **44**, 9170–9177 (1991)
- 15.14 T. Ohzuku, Y. Iwakoshi, K. Sawai: Formation of lithium-graphite intercalation compounds in nonaqueous electrolytes and their application as a negative electrode for a lithium ion (shuttlecock) cell, J. Electrochem. Soc. **140**, 2490–2498 (1993)
- 15.15 K.M. Shaju, G.V.S. Rao, B.V.R. Chowdari: Performance of layered  $\text{Li}(\text{Ni}_{1/3}\text{Co}_{1/3}\text{Mn}_{1/3})\text{O}_2$  as cathode for Li-ion batteries, Electrochimica Acta **48**, 145–151 (2002)
- 15.16 K. Mizushima, P.C. Jones, P.J. Wiseman, J.B. Goodenough:  $\text{Li}_x\text{CoO}_2$  ( $0 < x < 1$ ): A new cathode material for batteries of high energy density, Mater. Res. Bull. **15**, 783–789 (1980)
- 15.17 M.D. Johannes, K. Hoang, J.L. Allen, K. Gaskell: Hole polaron formation and migration in olivine phosphate materials, Phys. Rev. B **85**, 115106 (2012)
- 15.18 Y.J. Lee, F. Wang, C.P. Grey:  $^6\text{Li}$  and  $^7\text{Li}$  MAS, NMR studies of lithium manganate cathode materials, J. Am. Chem. Soc. **120**, 12601–12613 (1998)
- 15.19 B. Key, R. Bhattacharyya, M. Morcrette, V. Seznec, J.M. Tarscon, C.P. Grey: Real-time NMR investigations of structural changes in silicon electrodes for lithium-ion batteries, J. Am. Chem. Soc. **131**, 9239–9249 (2009)
- 15.20 H. Huang, S.-C. Yin, L.F. Nazar: Approaching theoretical capacity of  $\text{LiFePO}_4$  at room temperature at high rates, Electrochem. Solid-State Lett. **4**, A170–A172 (2001)
- 15.21 A.S. Andersson, B. Kalska, L. Häggström, J.O. Thomas: Lithium extraction-insertion in  $\text{LiFePO}_4$ : An x-ray diffraction and Mössbauer spectroscopy study, Solid State Ionics **130**, 41–52 (2000)
- 15.22 J.L. Allen, T.R. Jow, J. Wolfenstine: Improved cycle life of Fe-substituted  $\text{LiCoPO}_4$ , J. Power Sources **196**, 8656–8661 (2011)
- 15.23 R.A. Dunlap, D.A. Small, D.D. MacNeill, M.N. Obrovac, J.R. Dahn: A Mössbauer effect investigation of the Li Sn system, J. Alloy. Compd. **289**, 135–142 (1999)
- 15.24 M.D. Levi, G. Salitra, B. Markovsky, H. Teller, D. Aurbach, U. Heider, L. Heider: Solid-state electrochemical kinetics of Li-ion intercalation into  $\text{Li}_{1-x}\text{CoO}_2$ : Simultaneous application of electroanalytical techniques SSCV, PITT, and EIS, J. Electrochem. Soc. **146**, 1279–1289 (1999)
- 15.25 M. Takahashi, S. Tobishima, K. Takei, Y. Sakurai: Reaction behavior of  $\text{LiFePO}_4$  as a cathode material for rechargeable lithium batteries, Solid State Ionics **148**, 283–289 (2002)
- 15.26 J.L. Allen, T.R. Jow, J. Wolfenstine: Kinetic study of the electrochemical  $\text{FePO}_4$  to  $\text{LiFePO}_4$  phase transition, Chem. Mater. **19**, 2108–2111 (2007)
- 15.27 J.R. Dahn, E.W. Fuller, M. Obrovac, U. Vonsacken: Thermal stability of  $\text{Li}_x\text{CoO}_2$ ,  $\text{Li}_x\text{NiO}_2$  and  $\lambda\text{MnO}_2$  and consequences for the safety of Li-ion cells, Solid State Ionics **69**, 265–270 (1994)
- 15.28 D.D. MacNeil, Z.H. Lu, Z.H. Chen, J.R. Dahn: A comparison of the electrode-electrolyte reaction at elevated temperatures for various Li-ion battery cathodes, J. Power Sources **108**, 8–14 (2002)
- 15.29 R.V. Moshtev, P. Zlatilova, B. Puresheva, V. Manev: Material balance of petroleum coke/ $\text{LiNiO}_2$  lithium-ion cells, J. Power Sources **56**, 137–144 (1995)
- 15.30 D. Guyomard, J.M. Tarascon: The carbon/ $\text{Li}_{1+x}\text{Mn}_2\text{O}_4$  system, Solid State Ionics **69**, 222–237 (1994)
- 15.31 K. Xu: Nonaqueous liquid electrolytes for lithium-based rechargeable batteries, Chem. Rev. **104**, 4303–4418 (2004)
- 15.32 M. Winter: The solid electrolyte interphase – The most important and the least understood solid electrolyte in rechargeable Li batteries, Z. Phys. Chem. **223**, 1395–1406 (2009)

- 15.33 Y. Zeng, L. Li, H. Li, X. Huang, L. Chen: TG-MS analysis on thermal decomposable components in the SEI film on  $\text{Cr}_2\text{O}_3$  powder anode in Li-ion batteries, *Ionics* **15**, 91–96 (2009)
- 15.34 J. Zhang, R. Wang, X. Yang, W. Lu, X. Wu, X. Wang, H. Li, L. Chen: Direct observation of inhomogeneous solid electrolyte interphase on mmo anode with atomic force microscopy and spectroscopy, *Nano Lett.* **12**, 2153–2157 (2012)
- 15.35 S.S. Zhang: A review on electrolyte additives for lithium-ion batteries, *J. Power Sources* **162**, 1379–1394 (2006)
- 15.36 M.S. Ding, K. Xu, T.R. Jow: Liquid–solid phase diagrams of binary carbonates for lithium batteries, *J. Electrochem. Soc.* **147**, 1688–1694 (2000)
- 15.37 M.S. Ding, K. Xu, S. Zhang, T.R. Jow: Liquid–solid phase diagrams of binary carbonates for lithium batteries, Part II, *J. Electrochem. Soc.* **148**, A299–A304 (2001)
- 15.38 Z.K. Liu: Thermodynamic modeling of organic carbonates for lithium batteries, *J. Electrochem. Soc.* **150**, A359–A365 (2003)
- 15.39 J. O'M Bockris, A.K.N. Reddy: *Modern Electrochemistry*, Vol. 2, 2nd edn. (Plenum, New York 2000)
- 15.40 K. Xu: Charge-transfer process at graphite/electrolyte interface and the solvation sheath structure of  $\text{Li}^+$  in nonaqueous electrolytes, *J. Electrochem. Soc.* **154**, A162–A167 (2007)
- 15.41 R.G. Linford (Ed.): *Electrochemical Science and Technology of Polymers*, Elsevier Applied Science, Vol. 2 (Elsevier, London 1990) p. 281
- 15.42 G.E. Blomgren: Properties, structure and conductivity of organic and inorganic electrolytes for lithium battery systems. In: *Lithium Batteries*, ed. by J.P. Gabano (Academic, London 1983)
- 15.43 J. Evans, C.A. Vincent, P.G. Bruce: Electrochemical measurement of transference numbers in polymer electrolytes, *Polymer* **28**, 2324–2328 (1987)
- 15.44 H. Dai, S. Sanderson, J. Davey, F. Uribe, T.A. Zawodinski: Electrophoretic NMR measurements of lithium transference numbers in polymer gel electrolytes, *Proc. Electrochem. Soc.*, Vol. 96–17 (1996) pp. 111–120
- 15.45 H.J. Walls, T.A. Zawodinski: Anion and cation transference numbers determined by electrophoretic NMR of polymer electrolytes sum to unity, *Electrochem. Solid State Lett.* **3**, 321–324 (2000)
- 15.46 R. Jasinski: *High Energy Batteries* (Plenum, New York 1967)
- 15.47 K. Xu: *Encyclopedia of Electrochemical Power Sources*, Vol. 5 (Elsevier, Amsterdam 2009) p. 51
- 15.48 D. Aurbach, M.L. Daroux, P.W. Faguy, E. Yeager: Identification of surface films formed on lithium in propylene carbonate solutions, *J. Electrochem. Soc.* **134**, 1611–1620 (1987)
- 15.49 D. Aurbach, A. Zaban, A. Schecheter, Y. Ein-Eli, E. Zinigrad, B. Markovsky: The study of electrolyte solutions based on ethylene and diethyl carbonates for rechargeable Li batteries, *J. Electrochem. Soc.* **142**, 2873–2882 (1995)
- 15.50 K. Xu, U. Lee, S. Zhang, T.R. Jow: Syntheses and characterization of lithium alkyl mono- and dicarbonates as components of surface films in Li-ion batteries, *J. Phys. Chem. B* **110**(15), 7708–7719 (2006)
- 15.51 M. Onuki, S. Kinoshita, Y. Sakata, M. Yanagidate, Y. Otake, M. Ue, M. Deguchi: Identification of the source of evolved gas in Li-ion batteries using labeled solvents, *J. Electrochem. Soc.* **155**, A794–A797 (2008)
- 15.52 S. Malmgren, H. Rensmo, T. Gustafsson, M. Gorgoi, K. Edstrom: Nondestructive depth profiling of the solid electrolyte interphase on  $\text{LiFePO}_4$ , *Electrochem. Soc. Trans.* **25**(36), 201–210 (2010)
- 15.53 D. Bar-Tow, E. Peled, L. Burstein: A study of highly oriented pyrolytic graphite as a model for the graphite anode in Li-ion batteries, *J. Electrochem. Soc.* **146**, 824–832 (1999)
- 15.54 P. Lu, S.J. Harris: Lithium transport within the solid electrolyte interphase, *Electrochem. Commun.* **13**, 1035–1037 (2011)
- 15.55 A.C. Chu, J.Y. Josefowicz, G.C. Farrington: Electrochemistry of highly ordered pyrolytic graphite surface film formation observed by atomic force microscopy, *J. Electrochem. Soc.* **144**, 4161–4169 (1997)
- 15.56 J.O. Besenhard, M. Winter, J. Yang, W. Biberacher: Filming mechanism of lithium-carbon anodes in organic and inorganic electrolytes, *J. Power Sources* **54**, 228–231 (1993)
- 15.57 M.R. Wagner, J.H. Albering, K.C. Moeller, J.O. Besenhard, M. Winter: XRD evidence for the electrochemical formation of in PC-based electrolytes, *Electrochem. Commun.* **7**, 947–952 (2005)
- 15.58 K. Xu, Y. Lam, S. Zhang, T.R. Jow, T. Curtis: Solvation sheath of  $\text{Li}^+$  in nonaqueous electrolytes and its implication of graphite/electrolyte interface chemistry, *J. Phys. Chem. C* **111**, 7411–7421 (2007)
- 15.59 G.V. Zhuang, K. Xu, H. Yang, T.R. Jow, P.N. Ross Jr.: Lithium ethylene dicarbonate identified as the primary product of chemical and electrochemical reduction of EC in 1.2 M  $\text{LiPF}_6/\text{EC}:\text{EMC}$  Electrolyte, *J. Phys. Chem. B* **109**, 17567–17573 (2005)
- 15.60 S. Shi, P. Lu, Z. Liu, Y. Qi, L.G. Hector, H. Li, S.J. Harris: Direct calculation of Li-ion transport in the solid electrolyte interphase, *J. Am. Chem. Soc.* **134**, 15476–15487 (2012)
- 15.61 S.K. Jeong, M. Inaba, Y. Iriyama, T. Abe, Z. Ogumi: Electrochemical intercalation of lithium ion within graphite from propylene carbonate solutions, *Electrochem. Solid State Lett.* **6**, A13–A15 (2003)
- 15.62 Y. Yamada, Y. Iriyama, T. Abe, Z. Ogumi: Kinetics of lithium ion transfer at the interface between graphite and liquid electrolytes: Effects of solvent and surface film, *Langmuir* **25**, 12766–12770 (2009)
- 15.63 K. Xu, A.V. Cresce, U. Lee: Differentiating contributions to ion transfer barrier from interphasial resistance and desolvation at electrolyte/graphite interface, *Langmuir* **26**, 11538–11543 (2010)
- 15.64 J. Liu, Z. Chen, S. Busking, I. Belharouak, K. Amine: Effect of electrolyte additives in im-

- proving the cycle and calendar life of graphite/ $\text{Li}_{1.1}[\text{Ni}_{1/3}\text{Co}_{1/3}\text{Mn}_{1/3}]_{0.9}\text{O}_2$  Li-ion cells, *J. Power Sources* **174**, 852–855 (2007)
- 15.65 A. Xiao, L. Yang, B.L. Lucht, S.H. Kang, D.P. Abraham: Examining the solid electrolyte interphase on binder-free graphite electrodes, *J. Electrochem. Soc.* **156**, A318 (2009)
- 15.66 A.J. Smith, J.C. Burns, J.R. Dahn: A high precision study of the coulombic efficiency of Li-ion batteries, *Electrochem. Solid State Lett.* **13**, A177–A179 (2010)
- 15.67 J.C. Burns, J. Gauray, A.J. Smith, K.W. Eberman, E. Scott, J.P. Gardner, J.R. Dahn: Evaluation of effects of additives in wound Li-ion cells through high precision coulometry, *J. Electrochem. Soc.* **158**, A255–A261 (2011)
- 15.68 M.D. Halls, K. Tasaki: High-throughput quantum chemistry and virtual screening for lithium ion battery electrolyte additives, *J. Power Sources* **195**, 1472–1478 (2010)
- 15.69 L. Yang, B. Lucht: Inhibition of electrolyte oxidation in lithium ion batteries with electrolyte additive, *Electrochem. Solid-State Lett.* **12**, A229–A231 (2009)
- 15.70 K. Xu, A. von Cresce: Interfacing electrolytes with electrodes in Li-ion batteries *J. Mater. Chem.* **21**, 9849–9864 (2011)
- 15.71 A. von Cresce, K. Xu: Electrolyte additive in support of 5 V Li-ion chemistry, *J. Electrochem. Soc.* **158**, A337–A342 (2011)
- 15.72 A. Abouimrane, I. Belharouak, K. Amine: Sulfone-based electrolytes for high-voltage Li-ion batteries, *Electrochem. Commun.* **11**, 1073–1076 (2009)
- 15.73 Y. Abu-Lebdeh, I. Davison: High-voltage electrolytes based on adiponitrile for Li-ion batteries, *J. Electrochem. Soc.* **156**, A60–A65 (2009)
- 15.74 J.R. Dahn, J. Jiang, L.M. Moshurchak, M.D. Fleischauer, C. Buhrmester, L.J. Krause: High-rate overcharge protection of  $\text{LiFePO}_4$ -based Li-ion cells using the Redox shuttle additive 2,5-Di-tert-butyl-1,4-dimethoxybenzene, *J. Electrochem. Soc.* **152**, A1283–A1289 (2005)
- 15.75 L.M. Moshurchak, W.M. Lamanna, M. Bulinski, R.L. Wang, R.R. Garsuch, J. Jiang, D. Magnusson, M. Triemert, J.R. Dahn: High-potential Redox shuttle for use in Lithium-ion batteries, *J. Electrochem. Soc.* **156**, A309–A312 (2009)
- 15.76 S.S. Zhang: A review on the separators of liquid electrolyte Li-ion batteries, *J. Power Sources* **164**, 351–364 (2007)
- 15.77 P. Arora, Z. Zhang: Battery separators, *Chem. Rev.* **104**, 4419–4462 (2004)
- 15.78 M.E. Orazem, B. Tribollet: *Electrochemical Impedance Spectroscopy* (Wiley, Hoboken 2008)
- 15.79 S. Zhang, K. Xu, T.R. Jow: EIS study on the formation of solid electrolyte interface in Li-ion battery, *Electrochimica Acta* **51**, 1636–1640 (2006)
- 15.80 S. Zhang, K. Xu, T.R. Jow: Electrochemical impedance study on the low temperature of Li-ion batteries, *Electrochimica Acta* **49**(1), 1057–1061 (2004)
- 15.81 S. Mukerjee, T.R. Thurston, N.M. Jisrawi, X.Q. Yang, J. McBreen, M.L. Daroux, X.K. King: Structural evolution of  $\text{Li}_x\text{Mn}_2\text{O}_4$  in lithium-ion battery cells measured in situ using synchrotron x-ray diffraction techniques, *J. Electrochem. Soc.* **145**, 466–472 (1998)
- 15.82 J.B. Leriche, S. Hamelet, J. Shu, M. Morcrette, C. Masquelier, G. Ouvrard, M. Zerrouki, P. Soudan, S. Belin, E. Elkaim, F. Baudalet: An electrochemical cell for operando study of lithium batteries using synchrotron radiation, *J. Electrochem. Soc.* **157**, A606–A610 (2010)
- 15.83 Y. Sun, Z. Chen, H. Noh, D. Lee, H. Jung, Y. Ren, S. Wang, C. Yoon, S. Myung, K. Amine: Nanostructured high-energy cathode materials for advanced lithium batteries, *Nat. Mater.* **11**, 942–947 (2012)
- 15.84 J. Huang, L. Zhong, C.M. Wang, J.P. Sullivan, W. Xu, L.Q. Zhang, S.X. Mao, N.S. Hudak, X.H. Liu, A. Subramanian, H. Fan, L. Qi, A. Kushima, J. Li: In situ observation of the electrochemical lithiation of a single  $\text{SnO}_2$  nanowire electrode, *Science* **330**, 1515 (2010)
- 15.85 R.E. Gerald II, R.J. Klingler, G. Sandi, C.S. Johnson, L.G. Scanlon, J.W. Rathke:  $^7\text{Li}$  NMR study of intercalated lithium in curved carbon lattices, *J. Power Sources* **89**, 237–243 (2000)
- 15.86 B. Key, R. Bhattacharyya, M. Morcrette, V. Seznec, J.M. Tarascon, C.P. Grey, B. Key, R. Bhattacharyya, M. Morcrette, V. Seznec, J.M. Tarascon, C.P. Grey: Real-time NMR investigations of structural changes in silicon electrodes for lithium-ion batteries, *J. Am. Chem. Soc.* **131**, 9239 (2009)
- 15.87 N. Balke, S. Jesse, A.N. Morozovska, E. Eliseev, D.W. Chung, Y. Kim, L. Adamczyk, R.E. Garcia, N. Dudney, S.V. Kalinin: Nanoscale mapping of ion diffusion in a lithium-ion battery cathode, *Nature Nanotech.* **5**, 749–754 (2010)
- 15.88 S. Kalinin, N. Balke, S. Jesse, A. Tselev, A. Kumar, T.M. Arruda, S. Guo, R. Proksch: Li-ion dynamics and reactivity on the nanoscale, *Mater. Today* **14**, 548–558 (2011)
- 15.89 K. Rhodes, N. Dudney, E. Lara-Curzio, C. Daniel: Understanding the degradation of silicon electrodes for lithium-ion batteries using acoustic emission, *J. Electrochem. Soc.* **157**, A1354–A1360 (2010)
- 15.90 T. Ohzuku, H. Tomura, K. Sawai: Monitoring of particle fracture by acoustic emission during charge and discharge of  $\text{Li/MnO}_2$  cells, *J. Electrochem. Soc.* **144**, 3496–3500 (1997)
- 15.91 H. Wang, R.G. Downing, J.A. Dura, D.S. Hussey: In situ neutron techniques for studying lithium ion batteries. In: *Polymers for Energy Storage and Delivery: Polyelectrolytes for Batteries and Fuel Cell*, ACS Symp. Ser. Vol. 1096, (American Chemical Society, Washington DC 2012) pp. 91–96
- 15.92 J.E. Owejan, J.P. Owejan, S.C. DeCaluwe, J. Dura: Solid electrolyte interphase in Li-ion batteries: Evolving structures measured in situ by neutron reflectometry, *Chem. Mater.* **24**, 2133–2140 (2012)

- 15.93 *Coin Cell Components and Tools for Making Them are Available from Vendors such as Hohsen Corp.* (Osaka and MTI, Richmond 2016)
- 15.94 T.R. Jow, M.B. Marx, J.L. Allen: Distinguishing  $\text{Li}^+$  charge transfer kinetics at NCA/electrolyte and graphite/electrolyte interfaces, and NCA/electrolyte and LFP/electrolyte interfaces in Li-ion cells, *J. Electrochem. Soc.* **59**(5), A604–A612 (2012)
- 15.95 IEC 61960: Secondary cells and batteries containing alkaline or other non-acid electrolytes – Secondary lithium cells and batteries for portable applications, International Electrotechnical Commission (2011) Edition 2.0
- 15.96 M.S. Whittingham: History, evolution, and future status of energy storage, *Proc. IEEE* **100** (2012) pp. 1518–1534
- 15.97 J. Dahn, G.M. Ehrlich: Lithium ion batteries. In: *Linden's Handbook of Batteries*, 4th edn., ed. by T.B. Reddy (McGraw Hill, New York 2011), Chap. 26
- 15.98 IEC 62620: Secondary cells and batteries containing alkaline or other non-acid electrolytes – Large format secondary lithium cells and batteries for use in industrial applications, International Electrotechnical Commission (2010) Draft edition 1.0, Dec. 14
- 15.99 Idaho National Engineering and Environmental Laboratory; United States Department of Energy, Office of Energy Efficiency and Renewable Energy: *PNGV Battery Test Manual* (US Department of Energy, Assistant Secretary for Energy Efficiency and Renewable Energy, Idaho Operations Office, Washington 2001) DOE/ID-10597, Revision 3
- 15.100 K. Amine, I. Belharouak, Z. Chen, T. Tran, H. Yumoto, N. Ota, S.-T. Myung, Y.-K. Sun: Nanos-structured anode material for high-power battery system in electric vehicles, *Adv. Mater.* **22**, 3052–3057 (2010)
- 15.101 S.S. Zhang, K. Xu, T.R. Jow: Charge and discharge characteristics of a commercial  $\text{LiCoO}_2$  based 18650 Li-ion battery, *J. Power Sources* **160**, 1403–1409 (2006)
- 15.102 T.R. Jow, S.S. Zhang, K. Xu, J. Allen: Electrolytes for low temperature operations of Li-ion batteries, *ECS Trans.* **3**(27), 51–58 (2007)
- 15.103 D. Andre, M. Meiler, K. Steiner, Ch. Wimmer, T. Soczka-Guth, D.U. Sauer: Characterization of high-power lithium-ion batteries by electrochemical impedance spectroscopy. I. Experimental investigation, *J. Power Sources* **196**, 5334–5341 (2011)
- 15.104 P. Liu, J. Wang, J. Hicks-Garner, E. Sherman, S. Soukiazian, M. Verbrugge, H. Tataria, J. Musser, P. Finamore: Aging mechanisms of  $\text{LiFePO}_4$  batteries deduced by electrochemical and structural analyses, *J. Electrochem. Soc.* **157**(4), A499–A507 (2010)
- 15.105 I. Bloom, S.A. Jones, E.G. Polzin, V.S. Battaglia, G.L. Henriksen, C.G. Motloch, R.B. Wright: Mechanisms of impedance rise in high-power, lithium-ion cells, *J. Power Sources* **111**, 152–159 (2002)
- 15.106 R. Srinivasan, B.G. Carkhuff, M.H. Butler, A.C. Baisden: Instantaneous measurement of the internal temperature in lithium-ion rechargeable cells, *Electrochimica Acta* **56**, 6198–6204 (2011)
- 15.107 R. Srinivasan: Monitoring dynamic thermal behavior of the carbon anode in a lithium-ion cell using a four-probe technique, *J. Power Sources* **198**, 351–358 (2012)
- 15.108 Y. Zhang, C.-Y. Wang: Cycle-life characterization of automotive lithium-ion batteries with  $\text{LiNiO}_2$  cathode, *J. Electrochem. Soc.* **156**, A527–A535 (2009)
- 15.109 A.J. Smith, J.C. Burns, S. Trussler, J.R. Dahn: Precision measurements of the coulombic efficiency of lithium-ion batteries and of electrode materials for lithium-ion batteries, *J. Electrochem. Soc.* **157**, A196–A202 (2010)
- 15.110 J.C. Burns, G. Jain, A.J. Smith, K.W. Eberman, C.E. Scott, J.P. Gardner, J.R. Dahn: Evaluation of effects of additives in wound Li-ion cells through high precision coulometry, *J. Electrochem. Soc.* **158**, A255–A261 (2011)
- 15.111 IEC 62133: Secondary cells and batteries containing alkaline or other non-acid electrolytes – Safety requirements for portable sealed secondary cells, and for batteries made from them, for use in portable applications, International Electrotechnical Commission (2002)
- 15.112 UL 1642: UL Standard for Safety for Lithium Batteries, Underwriters Laboratories (2005) 4th edn., IL 60062–2096
- 15.113 M.S. Whittingham: Lithium batteries and cathode materials, *Chem. Rev.* **104**, 4271–4301 (2004)
- 15.114 D. Doughty, E.P. Roth: A general discussion of Li-ion battery safety, *Electrochem. Soc. Interface* **21**(2), 37–44 (2012)
- 15.115 D.D. MacNeil, Z. Lu, Z. Chen, J.R. Dahn: A comparison of the electrode/electrolyte reaction at elevated temperatures for various Li-ion battery cathodes, *J. Power Sources* **108**, 8–14 (2002)
- 15.116 E.P. Roth: Effect of cathode composition on abuse response of 18650 Li-ion cells, *Proc. 43rd Power Sources Conf.*, Philadelphia (2008) p. 521
- 15.117 C. Orendorff, D. Doughty: Lithium ion battery safety, *Electrochem. Soc. Interface* **21**(2), 35–66 (2012)
- 15.118 E.P. Roth, C.J. Orendorff: How electrolytes influence battery safety, *Electrochem. Soc. Interface* **21**(2), 45–49 (2012)
- 15.119 J.R. Akridge, Y.V. Mikhaylik, N. White: Li/S fundamental chemistry and application to high-performance rechargeable batteries, *Solid State Ionics* **175**, 243–245 (2004)
- 15.120 S.S. Zhang, D. Foster, J. Read: Discharge characteristic of a non-aqueous electrolyte  $\text{Li}/\text{O}_2$  battery, *J. Power Sources* **195**, 1235–1240 (2010)

Springer Handbook of Electrochemical Energy

Breitkopf, C.; Swider-Lyons, K. (Eds.)

2017, XXVI, 1016 p. 652 illus. in color., Hardcover

ISBN: 978-3-662-46656-8